Magnetoelastic Coupling in Thin Films

by

Ohsung Song

B. S. Metallurgical Engineering, Seoul National University (1987)

M. S. Metallurgical Engineering, Seoul National University (1989)

submitted to the Department of
Materials Science and Engineering in
Partial Fulfillment of the Requirements for the Degree of

DOCTOR OF PHILOSOPHY

at the

MASSACHUSETTS INSTITUTE OF TECHNOLOGY

May 1994

Signiture of Author _____
Department of Materials Science and Engineering
April 29, 1994

Certified by _____
Robert C. O'Handley
Thesis Supervisor

Certified by _____
Manuel Oliveria
Thesis Supervisor

Accepted by _____
Carl. V. Thompson II
professor of Electronic Materials
Chair, Departmental Committee on Graduate students

Magnetoelastic Coupling in Thin Films

by

Ohsung Song

Submitted to the Department of Materials Science and Engineering on April 29, 1994 in partial fulfillment of requirements for the Degree of Doctor of Philosophy in Electronic Materials.

Abstract

We have discovered that magnetoelastic (ME) coupling coefficients (or magnetostriction coefficients) of polycrystalline and single crystal nickel and polycrystalline permalloy ($Ni_{79}Fe_{21}$) thin films take on anomalously large values as film thickness decreases below around 50Å. This effect is modeled to show that the anomaly is associated with a surface effect. The behavior of these coefficients as a function of thickness in films resembles the behavior that is observed for the effective magnetic anisotropy in thin films. Both behaviors are consistent with the Néel model which predicts $A^{eff} = A^{bulk} + A^{surface}/t$ where A may be the magnetic anisotropy constant, K, or the ME coupling coefficient, B. Thus, we propose using the Néel model to analyze this behavior. The film thickness over which the surface anomalies are observed to be significant, especially in single and polycrystalline Ni, is much greater than predicted by the Néel model without exchange coupling.

The polycrystalline films are deposited using electron beam evaporation on Ag/Si(100), Cu/Si (100) or Si wafer substrates which can be strained by a 4-point bending holder. Epitaxial Cu/Ni/Cu sandwich films on Si(100) wafer substrate (Cu/ Ni(100)/ Cu(100)/ Si(100)) prepared by molecular beam epitaxy (MBE) were also studied.

The surface magnetization is measured as a function of both applied magnetic field and applied mechanical strain to get the surface ME coupling coefficients of Ni and permalloy ($Ni_{79}Fe_{21}$) films. *In-situ* magneto-optic Kerr effect (MOKE) measurements or *ex-situ* vibrating sample magnetometer (VSM) measurements are used to obtain θ_K-H (Kerr rotation) or M-H loops. Anaysis of such loops taken under different uniaxial strains imposed by four-point bending of the substrate allows determination of the magnetoelastic coupling coefficient B.

The surface of a cubic material is actually a region of reduced tetragonal symmetry. A formalism is presented for determining the ME coupling coefficients of tetragonally distorted surfaces and thin films. The equation of motion of the magnetization is determined from free energy density expressions containing terms for crystalline and shape anisotropy, ME anisotropy and applied field. Canonical magnetization curves taken under different strains can be fit to the equations of motion to extract the ME coefficients. A more general method is proposed which allows ME coupling coefficients to be determined from the area between arbitrarily shaped M-H curves taken at different strains.

Effective ME coupling coefficients, $B^{eff}(t)$, are measured *in-situ* in an ultra high vacuum chamber with respect to film thickness for 1) polycrystalline permalloy ($Ni_{79}Fe_{21}$) on silver (permalloy/ Ag/Si(100)) , 2) polycrystalline permalloy ($Ni_{79}Fe_{21}$) on copper (permalloy/ Cu/Si(100)), 3) polycrystalline nickel on silicon wafer (Ni/ Ag/Si(100)) and 4) epitaxial Cu/Ni/Cu sandwich films on Si(100) wafer substrate (Cu/ Ni(100)/ Cu(100)/ Si(100)). Also the effective ME coupling coefficients, $B^{eff}(t)$, of polycrystal permalloy on silver measured with a *ex-situ* VSM showed the same result.

The giant ME coupling we have observed in thin films is not the result of a change in film composition. The Ni/Fe ratio in our permalloy films is uniform through the film thickness and the same in all films we have studied by Auger electron spectroscopy (AES). Further, there are no impurities present in the thinnest Ni films which could account for the stronger B^{eff} observed there. Transmission electron microscopy (TEM) and Auger depth profiling illustrate that some chemical interactions occur at the interfaces and these affect the form of the results but are not responsible for the $B^{surface}/t$ behavior. Our microstructural characterization of the films with TEM indicates that our magnetic films are continuous and uniform with random grain orientations.

Single crystal Ni sandwich films (Cu/Ni/Cu/Si(100)) deposited by MBE have also been investigated to determine $B_1^{eff}(t)$ and $B_2^{eff}(t)$ in a single crystalline cubic symmetry. The findings from the above investigation enabled us to propose a phenomenological model that can be applied to any epitaxial magnetic sandwich structure in determining ME coupling coefficients, $B_1^{eff}(t)$ and $B_2^{eff}(t)$, and the Néel interface magnetic anisotropy energy density, K_N. This method also indicates the presence of a surface-induced ME anomaly in epitaxial Cu/Ni/Cu/Si(100), namely, $B_i^{eff} = B_i^{bulk} + B_i^{surface}/t$, just as our direct measurements do for polycrystalline films.

These new results have very important implications for thin film devices. These observations suggest that the surface conditions of thin film magnetic devices are of great importance in controlling anisotropy.

Thesis Supervisor: Robert C. O'Handley
Senior Research Scientiest

Thesis Supervisor: Manuel Oliveria
Professor of Materials Science and Engineering

Table of Contents

List of Tables and Figures

Chapter 1. Introduction

Chapter 2. Backgrounds

Table 2.4.1. Magnitude of bulk anisotropy energies in Ni and NiFe films.

Fig.2.4.1.1. Experimental setup in a uniaxial magnetic easy axis case. Polycrystalline Ni of thickness 1200 Å is deposited on textured Cu strip, and streched by a yoke-type holder actuated by a bolt.

Fig.2.4.1.2. The expected m-H curves in an uniaxial magnetic easy axis with respect to strain. We define $b = B \cdot e$.

Fig.2.4.1.3. Real MOKE hysteresis loops with various strain.

Fig.2.4.2.1. Arbitary domains (m) and external field (H).

Fig.2.4.2.2. Expected m-H loops of polycrystalline Ni with respect to various strain ($e = \pm 4 \times 10^{-4}, \pm 1 \times 10^{-3}$).

Fig.2.4.3.1. Experimental setup to determine B_1 in a single cubic crystalline symmetry.

Fig.2.4.3.2. The expected m-H loops with various strains in a cubic symmetry .
We define $b = B \cdot e$.
1) $e = 0$ 2) $e = -3 \times 10^{-4}$ 3) $e = -5 \times 10^{-4}$ 4) $e = -10 \times 10^{-4}$

Fig.2.4.3.3. Experimental setup for B_2.

Fig.2.4.3.4. m-H loop behavior in single crystalline Ni film with shear strain to get B_2.
We define $b = B \cdot e$.
1) $e = 0$ 2) $e = -3 \times 10^{-4}$ 3) $e = -5 \times 10^{-4}$ 4) $e = -10 \times 10^{-4}$

Fig.2.5.1. Interaction between two magnetic atoms and coordinate sysem.

Table 2.5.1. Anisotropy constant K_1 and magnetoelastic coupling coefficients B_1, B_2 for fcc Ni (at 298 K) and bcc Fe (at 298K). The Néel model parameters derived from them.

Fig.2.5.2. Illustration of bond symmmetry of fcc-thin films.
(a) Nearest neighbor cluster around bulk fcc atoms

(b) Vacant sites due to creation of surface

(c) Nearest neighbor cluster around surface fcc atoms

Table 2.5.2. Bulk and surface magnetoelastic coupling coefficients for cubic structures in the (100) and (111) surface coordinate system. (in Ni/Cu system)

(100) surface gives $B^{eff}{}_1(t)$

(111) surface gives $B^{eff}{}_2(t)$

Fig.2.5.3. Illustration of B's with respect to film thickness under biaxial misfit strain:

single crystal Ni under biaxial strain

(a) $B^{eff}{}_1(t) = [6.2\text{-}5.25/t(Å)]$ $(x10^6\ J/m^3)$

(b) $B^{eff}{}_2(t) = [8\text{-}6.1/t(Å)]$ $(x10^6\ J/m^3)$

Chapter 3. Experimental procedure and instrumentation

Fig.3.1.1. Schematic top view of UHV camber. (Base pressure: 10^{-8} Torr)

A: e-beam evaporator B: Pump line equipped with mechanical and turbo pumps

C: Windows D: Magnets for transverse MOKE E: Magnets for polar MOKE

F: Rotatable Platform. G: Sputter gun H: Laser for MOKE

I: Photodetector for MOKE J: MOKE workbench K: Controllers.

Fig.3.1.2 Schematic behavior of MOKE loop according to strain.

(a) A longitudinal MOKE loop without external imposed strain

(b) A polar MOKE loop without external imposed strain

(c) Change of MOKE loops with strain.

(r: reference loop wihout strain t: with tensile strain c: with compressive strain.)

Fig.3.1.3. Schematic illustration of sample preparation for the VSM measurement.

(a) Circular magnetic films on rectangular silicon wafer.

(b) Four-point bending holder for the ex-situ VSM measurement.

(c) Bending for the tensile strain.

(d) Bending for the compressive strain.

(e) Schematic illustration of VSM measurement with holder.

Fig.3.1.4 Schematic diagram of expectd m-H loops according to strains.

Fig.3.1.5. Measured m-H loops *in-situ* with MOKE

Fig.3.1.6. Measured m-H loops *ex-situ* with VSM

Fig.3.2.1. Samples for the experiment
a) polycrystalline permalloy/2000Å silver/Si(100)
b) polycrystalline permalloy/2000Å copper/Si(100)
c) polycrystalline nickel/natural silicon oxide(SiO_2)/Si(100)
d) Cu capping/ single crystalline Ni/ 2000Å Cu(100)/ Si(100)

Fig.3.2.2. Schematic diagram of e-beam evaporator

Fig.3.2.3. Schematic diagram of MBE chamber

Fig.3.3.1. Schematic representation of the magneto-optic Kerr interaction. The incident light is linearly polarized and the light reflected from the magnetized film has a Kerr rotation and ellipticity (After Bader,1987).

Fig.3.3.2. Illustraion of MOKE measurement setup

Fig.3.4.1. Illustration of Auger process.

Fig.3.5.1. Schematic diagram of PZT 4-point bending specimen holder.
(a) simple streching (b) PZT as a substrate (c)PZT as an actuator

Fig.3.5.2. Four-point sample holder. L=3 cm, a=1 cm.
(a) tensile strain (b) compressive strain

Chapter 4. Experimental results

Fig.4.1.1. Plot of magnetoelastic coupling coefficient for polycrystalline permalloy/Ag/Si vs. film thickness. Measurements are done *in-situ* .

Fig.4.1.2. Plot of B^{eff}•t vs. film thickness (t)

Fig. 4.1.3. Auger depth profiling of the permalloy film on silver vs. sputtering time

Fig.4.1.4. Magnetostriction of polycrystalline Ni-Fe alloy.(After O'Handley, 1977).

Fig.4.1.5. Plot of $B^{eff}(t)$ vs. t measured *ex-situ* by VSM .

Fig.4.2.1. Magnetoelastic coupling coefficient for polycrystalline permalloy/Cu/Si vs. permalloy thickness. Measurements are done *in-situ* .

(a) Plot of B^{eff} vs. film thickness (t)

(b) Plot of B^{eff}·(t-13) vs. (t-13)

Fig.4.2.2. Plot of atomic content of Ni and Fe elements in NiFe vs. sputtering time (min).

Fig.4.2.3. Binary phase diagrams of (a) Ag-Ni and Ag-Fe, (b) Cu-Ni and Cu-Fe (ASM Handbook , vol 3, Alloy Phase diagrams. ASM international, the Materials Information Society)

Fig.4.3.1. (a) Plot of $B^{eff}(t)$ for Ni/SiO_2/Si with film thickness.

(b) Plot of B^{eff}•t vs. film thickness (t)

Fig.4.3.2. Variation of magnetostrciton coefficients in polycrystalline Ni with Si and other solvents. (After Batova)

Fig. 4.4.1. The change of magnetization direction of Ni(100)/Cu(100) epitaxial films with respect to Ni thickness.

Fig.4.4.2. m-H hysteresis loops of Cu/Ni 500Å /Cu(100) film with strain. Measured *ex-situ* by VSM. Maximum applied magnetic filed was 5000 Oe.

(a) no external strain. (b) with $-7x10^{-4}$ uniaxial imposed strain.

Fig.4.4.3. Plot of $K^{eff} \cdot t$ with Ni thickness. Data from Jungblut (1994). Solid curves are data curve fitting.

(a) (100) Ni surface (Cu/Ni(100)/Cu(100))

(b) (111) Ni surface (Cu/Ni(111)/Cu(100)).

Fig.4.4.4. Illustration of averaged strain with film thickness.

Table 4.4.1. Bulk and surface magnetoelastic coupling coefficients and K_N for single crystal Ni. (Determined from Bochi's method applied to Jungblut's data.)

Fig.4.4.5. Plots of extracted magnetoelastic coupling coefficients in Cu/Ni/Cu.

(a) $B_1^{eff} = [6.2 - 192/t(Å)]$ $(x10^6\ J/m^3)$

(b) $B_2^{eff} = [8.5 - 37/t(Å)]$ $(x10^6\ J/m^3)$

Fig.4.5.1. TEM micrographs of 2000Å silver layer.

(a) Bright field image (b) Selected area diffraction pattern (SADP)

Fig.4.5.2. AFM micrographs

(a) 2000Å Ag/ Si(100)

(b) 40Å permalloy/ 2000Å Ag/ Si(100)

Fig.4.5.3. TEM micrographs of 120Å permalloy film/ 2000Å Ag layer.

(a) Bright field image (b) SADP

Fig.4.5.4. TEM micrographs of 10Å permalloy film/ formvar.

(a) Bright field image

(b) SADP of 10Å permalloy

(c) SADP of formvar

Fig.4.5.5. TEM micrographs of 15Å permalloy film/ formvar.

(a) Bright field image

(b) SADP of 15Å permalloy

Chapter 5. Discussions

Appendix: A Four-point bending

Fig.A.3. Strain according to Y_a in 2" Si wafer.
(a) tensile strain (b) compressive strain

Appendix: B Tetragonal symmetry

Fig.B.1. Illustration of the cubic and tetragonal symmetry. Surface relaxation induce the transformtion of the symmetry from cubic to tetragonal in very thin films.

Acknowlegements

I would like thank all the people who have contributed to this study.

I am very grateful to my thesis supervisor, Dr. O'Handley for his full support during my study at MIT.

Also I would like to thank my thesis committee members: Professor Manuel Oliveria-my thesis co-supervisor, Professor Harry Tuller and Professor Gerbrand Ceder. They always showed deep interest and gave valuable advice to my research.

I appreciate the members of our thin film magnetic research group. I am indebted to Dr. Craig Ballentine for his technical help in the laboratory and many constructive discussion for this study. Dr. Changkyung Kim helped with TEM and Dr. Ivan Skorvanek collaborated in the Auger study. Mrs. Donna Chuang gratefully introduced the Néel model to me and Mr. Gabriel Bochi gave me the epitaxial Ni films. I would also like to thank Dr. Sung-Jin Song and Mr. Sang-hoon Ahn for their patience during the proofread.

Thanks to my family, my dear mother and brother for their love and encouragement. Special thank to my parents-in-law. My sincere gratitude is devoted to my deceased father.

Finally I would like to thank my wife Hyewon Min and my daughter Joohyun Michelle Song for their support and patience during graduate student life.

I would like to acknowledge support from Korean Government Oversea Scholarship program and ONR for their partial support of this work.

1. Introduction

Magnetic anisotropy means that the magnetization prefers a certain orientation. Therefore, it strongly affects the shape of the M-H curve. Crystal, shape, magnetoelastic and exchange anisotropy energies all contribute to the total anisotropy energy density. A thorough knowledge of magnetic anisotropy is of practical interest because it is exploited in design of most magnetic devices.

In this study, we are particularly interested in the magnetoelastic anisotropy energy among several other magnetic anisotropy energies, because magnetoelastic anisotropy is related to strain in the material which is one of the most easily controllable factors. When the direction of magnetization changes in a magnetic substance, its dimensions change. This anisotropic strain is called *magnetostriction*. Conversely, when the dimensions of a magnetic material are changed by an applied stress, its preferred direction of magnetization may change. This phenomenon is called *magnetoelasticity*. These two effects have the same physical origin. Here we use the term magnetoelasticity as a general category but magnetostriction coefficient (λ) and magnetoelastic coupling coefficient (B) are specific. The magnetoelastic anisotropy energy density (f_{ME}^{c}) in a cubic material has the form of:

$$f_{ME}^{c} = B_1(e_{11}\alpha_1^2+e_{22}\alpha_2^2+e_{33}\alpha_3^2)+ B_2(e_{12}\alpha_1\alpha_2+e_{23}\alpha_2\alpha_3+e_{31}\alpha_1\alpha_3) \quad (1.1).$$

Here α_i's are defined as the direction cosines between magnetization and crystallographic axis and e_{ij}'s are strain tensors. Eq.(1.1) gives the form of the magnetoelastic energy density in a material for a particular direction of magnetization, $\mathbf{M} = \mathbf{M_s}(\alpha_1, \alpha_2, \alpha_3)$, when a strain e_{ij} is imposed. When the independent variable **M** or **e** is is fixed, the dependent variable **e** or **M**, respectively, is determined by energy minimization including a term of the form of Eq.(1.1). Terms of the form of the product, B·e, give the part of the magnetic anisotropy energy that depends on strain in a magnetic material. The magnetoelastic coupling coefficient is a measure of the strength of the strain-dependent terms in the magnetic anisotropy energy density.

The magnetostriction coefficient (λ) and magnetoelastic coupling coefficient (B) are directly related to each other by elastic constants. This means if we measure the magnetostriction coefficient, we can determine the magnetoelastic coefficient and vice

versa, provided we know the elastic constants. They have opposite signs, as shown formally in Eq.(1.2).

$$B = - \lambda C_{ij} \qquad (1.2)$$

where C_{ij} represents a combination of elastic constants. The magnetoelastic coupling coefficient (B) is a magnetoelastic stress and has units of [N/m^2]; λ is a magnetoelastic strain so it is dimensionless. The product, $B \cdot e$, is a magnetoelastic energy density and has units of [J/m^3]. B depends on the temperature, composition, and , in thin films, on thickness. The magnetic anisotropy energies K and $B \cdot e$ determine the equilibrium orientation of **M** in a magnetic material.

An understanding of magnetoelasticity in magnetic materials is of fundamental importance for eventual control and exploitation of their properties in a variety of applications. Although magnetoelasticity is one of the most important factors controlling performance of magnetic devices, it is also one of the least well understood.

It is well known that magnetic properties in thin films show different behaviors compared with those in thick films. Some of these effects are due to the increased density of the defects in thin films; some are of fundamental origin. At the surface of a material, the reduced coordination and symmetry may lead to dangling bonds, surface states, charge redistribution and surface strains. Thus the electronic structure of the surface should be very different from that of the bulk. The surface magnetic properties as well as other properties which are related to electronic structure should be different from the bulk values (O'Handley, 1989). Consequently, different interaction forces result in surface relaxation strains that can exceed even 10% (Davis at el, 1992). As a result, the surface of a cubic solid can be tetragonally distorted relative to the bulk. The interfaces between films and substrates in heteroepitaxial films can produce coherent planar misfit strains which are typically of a few percent. The epitaxial Ni(100)/Cu(100) system has a misfit strain of 2.6%. Above a critical thickness, this misfit strain energy is relieved by the nucleation of misfit dislocation. Their presence complicates the stress and magnetoelastic analysis severely because the strain fields become highly inhomogeneous in the presence of misfit dislocations.

These electronic and structural changes at surfaces and interfaces in thin films are also accompanied by changes in other fundamental magnetic properties. These surface and interface effects in thin films have been studied for a long time. Gradmann (1974)

reviewed ferromagnetic order modified near the surface in thin films and discussed dependence on film thickness of the primary magnetic properties such as spontaneous magnetization, Curie temperature, and anisotropies. Koon et al (1987) observed that the orientation of the magnetic moment of the 2.4 ML films is perpendicular to the film while the orientation of of 5.5 ML is in-plane at room temperature in ultrathin Fe(100) films on Ag(100). Schneider (1990) showed that the Curie temperatures in ultra-thin fcc-Co films are dramatically lower than those of the bulk. Engel et al (1991) observed surface anisotropy effect in Co/Pd multilayer system. Victora and MacLaren (1993) calculated the interface anisotropy in a system of Co/Pd superlattices to explain the experimental interface anisotropy observation of Engel et al . Heinrich et al (1991) reported magnetic anisotropies and exchange coupling in ultrathin fcc Co(001) structure on Cu(001) template can be modified with respect to film thickness.

Thus, it is well accepted both theoretically and experimentally that the effective anisotropy (K^{eff}) in a thin film is different from that of the bulk. The effective anisotropy can be expressed as the sum of the bulk anisotropy (K^b) and the surface anisotropy (K^s) over the film thickness arising from surface and interface effects:

$$K^{eff} = K^b + K^s/t \qquad (1.3)$$

The inverse thickness dependence of the total effective anisotropy as shown in Eq.(1.3) expresses the fact that any anisotropy localized at the surface and given by the surface anisotropy constant K^s (energy/area), becomes more significant in thin films as surface to volume ratio increases. This surface anisotropy term was first explained by L. Néel (1954) as originating from the reduced symmetry of the surface. The K^s term is now called the Néel anisotropy and it includes any surface related effects. This term has potent technical implications. As thickness decreases, the K^s/t becomes dominant and the effective anisotropy may show dramatically different behavior compared with the bulk.

If we modify Eq(1.3) by multiplying t on both side, then we get :

$$K^{eff.}t = K^{b.}t + K^s \qquad (1.4)$$

In Eq.(1.4), if we plot the $K^{eff.}t$ versus t, then $K^{eff.}t$ would show linear behavior and the slope of this line is K^b and the intercept of y axis is K^s.

If we have a magnetic thin film which has negative K^b and positive K^s and behaves as shown in Fig.(1.1), then we can tune the magnetic property by varying the thickness.

Negative K^{eff} means in-plane magnetization and positive K^{eff} means perpendicular magnetization. Perpendicular magnetization is favorable for the high density recording media. Fig.(1.1) implies that we can make perpendicular recording media below a thickness, t_c. Also, the thickness, t_c, which makes $K^{eff} = 0$ is the optimal device thickness for many applications such as recording heads because they require zero effective anisotropy to enhance signal to noise ratio. Moreover, Eq.(1.3) implies if $K^b > 0$ and $K^s > 0$, then it may be possible to make strong hard magnets from a stack of thin magnetic film layers.

Here K^{eff} is a result of the contributions of crystalline, shape, magnetoelastic, Néel surface and interface anisotropy, but each anisotropy is not very well known. Shape anisotropy is dominant because we study thin films. In the case of the thin films, the shape anisotropy energy density, $(\mu_o/2)M_s^2\cos^2\theta$, tends to make perpendicular magnetization ($\theta = 0°$) unlikely. Shape terms tend to confine **M** to the plane of the film. Within the film plane, shape (ratio of length to width) may still play a small role in determining the equilibrium orientation of **M**. Magnetocrystalline anisotropy is of interest but, in isotropic polycrystalline or in single crystal Ni films, the contribution to the total effective anisotropy is small compared to shape anisotropy. Néel anisotropy is important, and is the dominant term to change the magnetic properties in ultrathin films. Interfacial anisotropy can be a dominant energy in multilayer films which have a multitude of interfaces. We are studying the magnetoelastic contribution to the magnetic anisotropy because it is not well understood, especially in thin films. One of the most important findings in our study is that the relationship, Eq.(1.3), for magnetic anisotropy also extends to the strain dependent part of that anisotropy. Thus, we can express the effective magnetoelastic coupling in thin film as:

$$B^{eff} = B^b + B^s/t. \qquad (1.5)$$

Eq.(1.5) will be proven in section 2.5 theoretically using the Néel model, and verified experimentally in Chapter 4 using the data of NiFe and Ni films .

Since the magnetoelastic coupling coefficient, B, is the coupling factor describing the magnetoelastic anisotropy energy with strains, Eq.(1.5) implies that the ME anisotropy can be anomalously large in ultrathin films. Eq.(1.5) implies that 1/t dependence of B^{eff} is also technically important, especially for magnetostrictive sensors and actuators. As device thickness decreases, B^{eff} can be large according to Eq.(1.5), making magnetostrictive strain

gauges and magnetoelastic transducers very sensitive. Since modern thin film magnetic devices such as magnetic recording media, heads and sensors are getting thinner and smaller to enhance recording density and sensitivity, it is important to know and control magnetic anisotropy.

Moreover, Eq.(1.5) suggests that strain and device thickness can tune the magnetic properties. If we have a material which shows in-plane magnetization because of negative effective anisotropy as indicated by a dashed line in Fig(1.2), then we may be able to manipulate the magnetic properties through the strain as shown with a solid line in Fig (1.2). Practically, strain can be controlled easily by using the specified substrate, coating the magnetic film or bending the magnetic films. We can tune the magnetic properties provided we know the magnitude and sign of the B^b and B^s because they are the factors indicating how much magnetoelastic anisotropy energy can be created with a given strain. As a result, we can tune the magnetic property with device thickness and the strain for our requirements of perpendicular magnetization for high density recording, or $K^{eff} = 0$ for the recording head and microtransformers.

Residual elastic stresses are always present in the thin films used in the various devices. The sign and magnitude of film stresses are for the most part determined by film/substrate lattice mismatch and film processing parameters, i.e., substrate temperature, kind of substrate, deposition rate, and method of deposition. Stresses of about $10^{9\text{-}10}$ dyn/cm^2, compressive or tensile, are often observed (O'Handley, 1993). In magnetic thin films these stresses interacting with the magnetostriction induce a magnetoelastic anisotropy which can influence the performance of magnetic thin film devices (Klokholm, 1988). Thus, it is very important to consider the effect of B^s in design and manufacturing magnetic devices.

In this work, we will study the behavior $B^{eff}(t)$ in Ni and permalloy (NiFe) films. Although Ni and permalloy films are used in a great many technical appplications, relatively few theoretical and experimental works on *surface magnetism* of these films have been done so far. In this study on ME couplings in thin films, we show the behavior of the magnetoelastic anisotropy energy at the surfaces of these films. Ni thin films are well suited for studying ME coupling effects because cubic bulk crystalline anisotropy coefficients (K_1= -4.5 x 10^3 J/m^3, K_2= 2.3 x 10^3 J/m^3) are known and are relatively small compared to the ME contribution to the magnetic anisotropy, B e, where B_1 = 6.2 x 10^6 J/m^3, B_2 = 8.5 x 10^6 J/m^3. In addition, considerable magnetic and thin film

processing data exists for Ni films (Benninger, 1967, Smoluchowski, 1941, Brown Jr.,1965, Franse, 1970, Lee, 1971).

Permalloy bulk alloys show simultaneously very small values of K_1, λ_{100} and λ_{111}. Thus, these alloys are easily magnetized and often exhibit low noise in ac applications because domain wall motion is uniform. Permalloy ($Ni_{80}Fe_{20}$) thin films, which are used in inductive and magnetoresistive (MR) recording heads are also of our interest for their importance as soft magnetic materials. Also, permalloy shows a sufficiently high magnetoresistance, so that it can be used as an MR read head.

In summary, our study shows how the variation of the ME coupling coefficients with film thickness allows the tunning of the magnetic anisotropy in ultrathin magnetic devices. In the following sections, we will discuss how we can measure the magnetoelastic coupling coefficients as a function of thickness, how the Néel model can predict the behavior of the B in thin films and what are the experimental results .

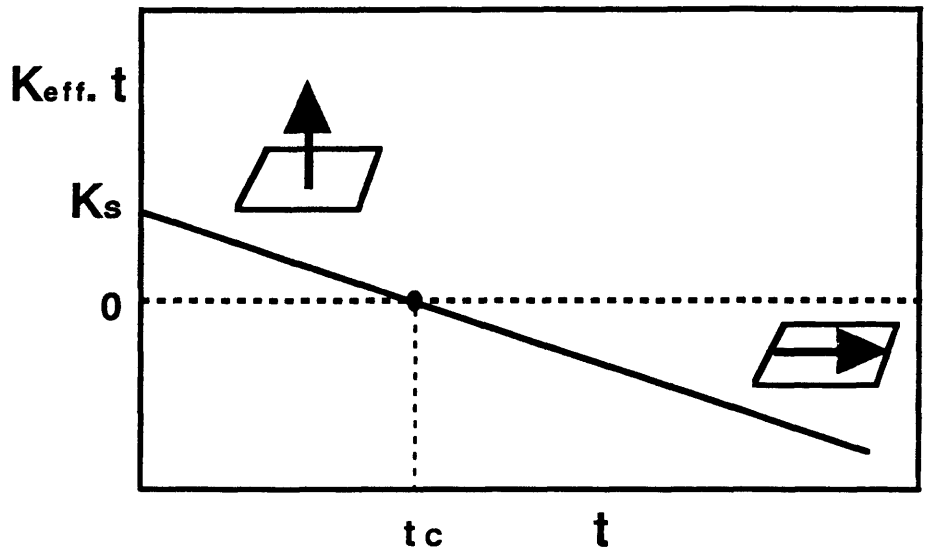

Fig.1.1 Schematic plot of $K^{eff.}t$ vs. t.

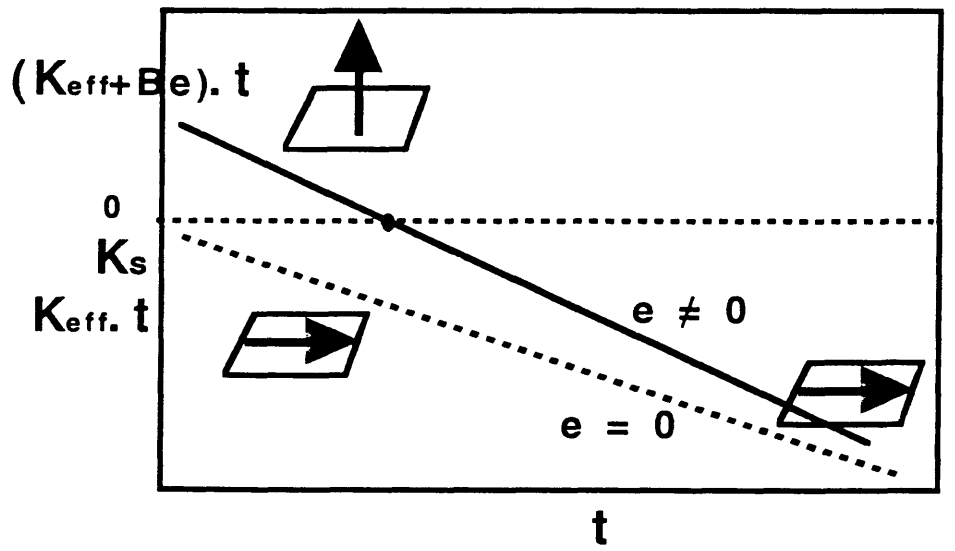

Fig.1.2 Schematic plot of $(K^{eff}+B^{eff.}e)\cdot t$ vs. t.

2 Background

2-1. Physical Origin of Magnetostriction

Magnetostriction, like crystal anisotropy, has its origin in spin-orbit interactions. It is relatively weak in 3-d transition metals and alloys because an applied field of a few hundred oersteds usually suffices to rotate the spin away from the easy direction (Cullity, 1972). The orbit-lattice coupling on crystal field splitting of electronic orbitals is strong in 3-d metals and alloys. This means that the orientations of the orbits are fixed very strongly to the lattice, and even large fields cannot change them. When an external field tries to reorient the spin of an electron, the orbit of that electron also tends to be reoriented if the coupling between orbital motion and spin (L•S) is strong. If L•S is weak as in 3-d metals and alloys, the spins can align with the field without reorienting the orbitals. The energy required to rotate the spin system of a domain away from the easy direction, which we call the magnetocrystalline anisotropy energy, is related to the energy of the spin-orbit coupling and to the strength of the crystal field.

The exchange interaction between two neighboring spins can be defined as a spin-spin coupling. This coupling is very strong and tends to keep neighboring spins parallel, or antiparallel, to one another. But the associated exchange energy depends only on the angle between adjacent spins and not at all on the direction of the spin axis relative to the crystal lattice. The spin-spin coupling generally does not contribute to the magnetocrystalline or the magnetoelastic anisotropy.

We can understand the physics of magnetostriction from Fig.(2.1.1). Here a dot is an atom nucleus, an arrow means a net magnetic moment per atom, and an oval represents an electron orbit ($l \neq 0$). The upper row of atoms depicts the paramagnetic state above T_C. If, for the moment, we assume that the spin-orbit coupling is very strong, then the effect of the spontaneous magnetization occurring below T_C would be to rotate the spins and the electron clouds into some particular orientation determined by the crystal anisotropy, left to right. The nuclei would be forced further apart, and the spontaneous magnetostriction would be $\Delta L/L$. If we then apply a strong field vertically, the spins and the electron clouds would rotate through 90°, and the domains of these spins would align by spin-orbit interaction. This interaction leads to magnetostrictive strain, $\Delta L/L$. The strains pictured are enormous, of the order of 0.3. Actually, we know the magnetostrictive strain is usually very small indeed, of the order of 10^{-5}. This means that the reorientation

of electron clouds takes place only to a very small extent in 3-d transition metals or the orbitals are very nearly sphericals in 3-d metals (Cullity, 1972).

For an isotropic material the strain due to a change in the direction of magnetization is simply related to the angle (θ) between the magnetization direction and the strain direction in which is measured:

$$e = (3/2)\lambda_S(\cos^2\theta - 1/3) \qquad (2.1.1)$$

More fundamentally, an imposed strain, e_{ij} , gives rise to a magnetoelastic anisotropy proportional to the strength of the ME coupling coefficients, B. In isotropic symmetry, the strain induced anisotropy energy density (f_{ME}) is given by:

$$f_{ME} = B(e_{11}\alpha_1^2 + e_{22}\alpha_2^2 + e_{33}\alpha_3^2 + e_{12}\alpha_1\alpha_2 + e_{23}\alpha_2\alpha_3 + e_{31}\alpha_1\alpha_3) + \ldots \qquad (2.1.2)$$

The B's are the stresses of magnetic origin that give rise to the magnetostrictive strains. B is proportional to the magnetostriciton coefficient as we have shown already in Eq.(1.2), $B = -\lambda C_{ij}$. f_{ME} adds a term to the total anisotropy energy that is strain dependent.

In this study, we have observed that the magnetostriction can be anomalously large near the surface of the magnetic materials. This implies that the spin-orbit interaction at the surfaces in the thin films can be very different from that of the film interiors. One way to picture this is the following. In the interior of the solid, electronic orbitals can take on orientations in three dimensions so the sum over the angular momenta of the valence electrons may tend to cancel. At a surface, electron orbitals extending out of the surface are unlikely. Hence, with most orbitals in the plane of the surface $L = \Sigma\ l_i$ will often be normal to the surface. Moreover, the magnetoelastic anisotropy energy that is strain dependent in thin films can be very different from that of the bulk materials.

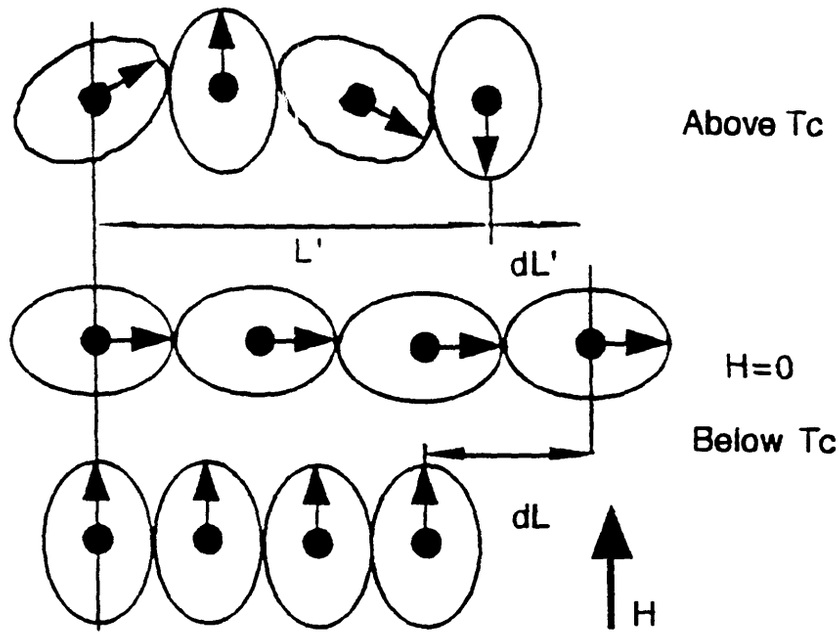

Fig .2.1.1. Illustration of physics of magnetostriction.(After Cullity,1972)

2.2. Magnetic Anisotropy and Surface Magnetic Anisotropy

Magnetic anisotropy energy density governs the directional dependence of certain magnetic properties. There are several kinds of anisotropy: crystal anisotropy, shape anisotropy, magneotelastic anisotropy. The magnetization (**M**) will lie along the crystallographic easy axis unless a torque due to shape, strain and field etc. does work on **M** to move it from that direction. But from another point of view **M** always lies along the easy axis which is determined by all the energies: crystal, shape, strain and field energy etc.

Crystalline anisotropy can be thought of as a torque which tends to align the magnetization to a certain direction within the crystal. In a single crystal magnetic material, the preferred direction for magnetization is called the easy axis (Cullity, 1972).

For a polycrystalline case in which all constituent grains are oriented randomly, the individual anisotropies may cancel out when averaged over the entire sample, and the body as a whole will not exhibit any crystal anisotropy, like an amorphous material. However in some polycrystalline bodies, the crystals have a prefered orientation, called texture. In this case the aggregate body will have an anisotropy, dictated by the dominant crystalline orientation. In an electron-beam deposited film on a specific textured substrate, such as the one studied in this work (see section 2.4.1 uniaxial magnetic easy axis), the individual crystals tend to align along certain crystalographic axes making it easier to magnetize the sample in one direction than it would be if the individual crystals oriented randomly.

The associated crystalline anisotropy energy density is given by:

$$f_c = K_0 + K_u \sin^2\theta \qquad \text{(for uniaxial easy axis case)}$$

$$= K_1(\alpha_1^2\alpha_2^2 + \alpha_2^2\alpha_3^2 + \alpha_3^2\alpha_1^2) + K_2\,\alpha_1^2\alpha_2^2\alpha_3^2 + \ldots . \qquad \text{(for cubic crystalline case)} \quad (2.2.1)$$

where K_u, K_1 and K_2 are anisotropy constants, θ is the angle between magnetization and crystallographic easy axis, and α's are direction consines between magnetization vector and crystal coordinate system.

Shape anisotropy comes into play if the crystal has a non-spherical shape. In a rectangular shape, the effect of shape anisotropy is simply to make it easier to magnetize the sample along the long axis than along the short one. Thus if we applied a magnetic field

along the out-of-plane direction in a thin film, a shape anisotropy energy $\frac{\mu_0}{2} M_s^2 \cos^2\theta$ $[J/m^3]$ should be stored in the sample of volume (V).

An applied tensile strain could rotate the magnetization away from the easy direction by an amount dependent on the magnitude of the strain and the strength of the ME coupling coefficient. The magnetoelastic energy density (f_{ME}) associated with a stress σ or strain e_{ij} is:

$$\begin{aligned} f_{me} &= -\frac{3}{2}\lambda_s \sigma \cos^2\theta \qquad \text{(isotropic polycrystalline case)} \\ &= B_1(e_{xx}\alpha_1^2 + e_{yy}\alpha_2^2 + e_{zz}\alpha_3^2) + \\ &+ B_2(\alpha_1\alpha_2 e_{xy} + \alpha_2\alpha_3 e_{yz} + \alpha_3\alpha_1 e_{zx}) \ [J/m^3] \ \text{(cubic crystal symmetry)} \end{aligned} \qquad (2.2.2)$$

If a tensile strain is applied along the [010] direction of a cubic material, the relative strain along the [100] and [001] directions are given by

$$e_{xx} = e_{zz} = -\nu e_{yy} \qquad (2.2.3)$$

where ν, which is called Poisson's ratio, is typically in the range 0.3 to 0.35 for metals. We approximate it as $\frac{1}{3}$. Since ME coupling coefficients (B's) and magnetostriction coefficients (λ's) are directly proportional to magnetoelastic anisotropy energy density (f_{ME}), we describe the ME anisotropy by studying B or λ with a given strain tensor information. Therefore, if we study the behavior of B with respect to film thickness, then we can describe the ME anisotropy behavior with thickness.

When magnetic anisotropy is measured as a function of thickness in films less than 100Å thick, it is generally observed that the anisotropy can be described by an equation of the Néel model form (L. Néel, 1954):

$$K^{eff}(t) = K^{bulk} + K^{surface}/t \qquad (2.2.4)$$

Here K^{bulk} is the bulk anisotropy constant measured at large film thickness and $K^{surface}$ is a surface energy density which changes the effective anisotropy in thin films from the bulk value.

Fig.(2.2.1) are examples of this surface ansiotropy behavior for two systems from the literature. Note that a plot of $K^{eff} \cdot t$ vs t gives linear behavior with slope indicating the value of K^{bulk} and y-intercept giving the value of $K^{surface}$. Fig.2.2.1.(a) is a plot of the anisotropy field ($H = 2K/M_S$) vs.inverse film thickness which has the form of Eq.(2.2.4). We can determine the bulk and surface ansiotropy from the intercept of the y-axis and slope of the plot (Gradmann, 1984).

Fig.2.2.1.(b) is a plot of the $K_{Co} \cdot t_{Co}$ versus Co thickness in Co/Pd epitaxial superlattices.(N. Engel et al. 1991). The linear behavior of this figure is well described by: $K_u^{Co} \cdot t_{Co} = (K_u^{eff} - 2\pi M_S^2)\, t_{Co} + 2K_S$. The uniaxial anisotropy energy density (K_u^{Co}) for Co/Pd superlattices can be modeled by inclusion of an effective interface contribution proportional to $1/t_{Co}$ and a volume term, independent of t_{Co}. The result show that the contribution of the Co-Pd interface to the total anisotropy is K_S=0.63 erg/cm^2 in all of the crystal orientations.

Thus, we reviewed several anisotropy energies and showed the total effective anisotropy energy in thin film is a sum of bulk anisotropy and surface anisotropy devided by the film thickness as in Eq.(2.2.4). The thickness dependence of the anisotropy is well accepted both theoretically and experimentally. The surface anisotropy energy become dominant as film thickness decreases. This anisotropy behavior in thin films has important technical implications to tune the desired magnetic property with device thickness as modern magnetic devices are getting thinner and smaller. It is of interest to study how we can measure the thickness dependence of each anisotropy, particularly the magnetoelastic contribution to the total effective anisotropy and how it behaves as thickness decreases. The principle to measure the magnetoelastic coupling coefficients in thin films will be discussed next in section 2.3.

(a)

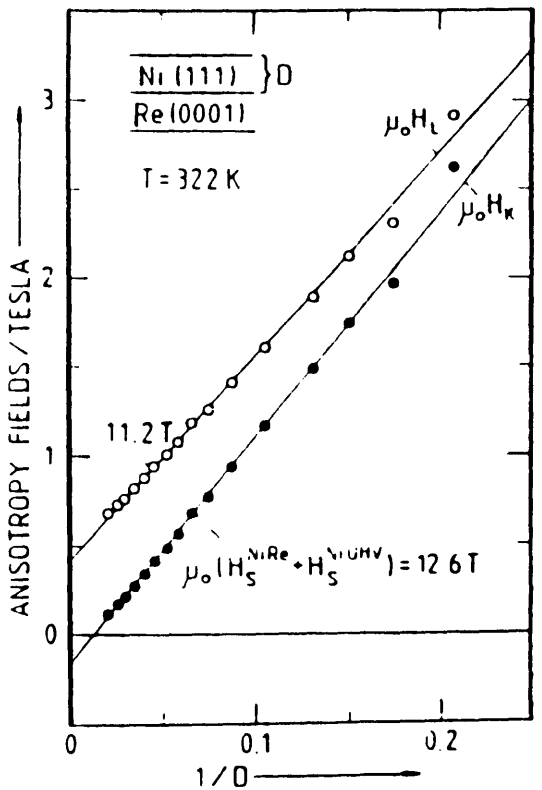

(b)

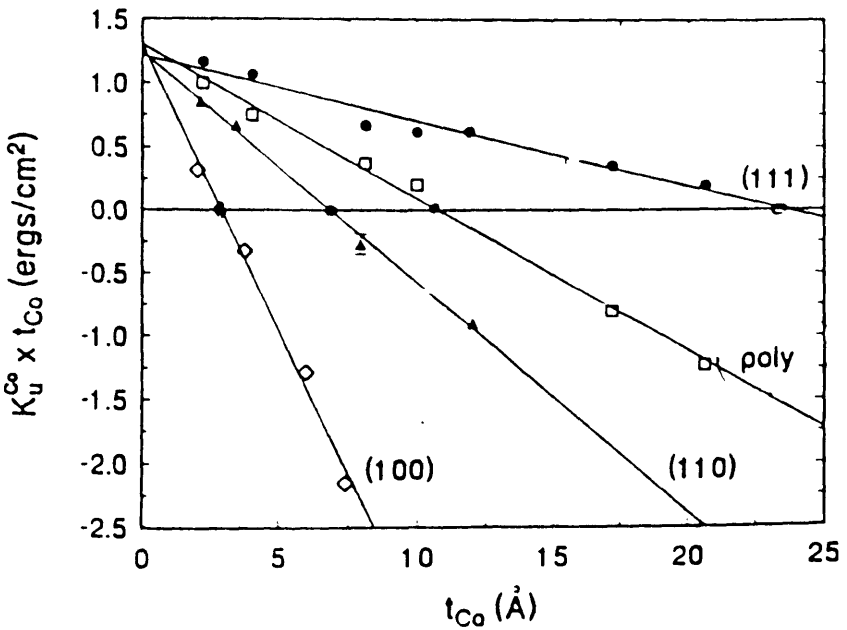

Fig.2.2.1. Reproductions of surface anisotropy data from the literature.

(a) Gradmann, (1984).
(b) Brad N. Engel, et al (1991).

2.3 Principles in measuring surface magnetoelastic coupling coefficients

On an m-H loop, the area bounded by the m-H curve, the saturation magnetization and the positive m-axis is proportional to the total anisotropy energy density (see Fig.(2.3.1)). Here we define m as the reduced magnetization, which is normalized by saturation magnetization (M_s), m = M/M_s, and H is the external magnetic field. The magnetoelastic coupling coefficients can be determined by measuring the variation of this area with a change in strain. If we take an m-H loop with no applied strain, the shaded region in Fig.(2.3.1)(a) is a reference anisotropy energy. Similarly, if we take another m-H loop with an external uniaxial strain, the shaded region in Fig.(2.3.1)(b) is the ansiotropy energy which includes the magnetoelastic anisotropy caused by the applied strain. The area difference between these two should include the information of the magnetoelastic coupling coefficients as shown in Fig.(2.3.1)(c).

From a macroscopic point of view, when an external force (for example tensile stress) is exerted on a magnetic material, the lattice will be distorted, and the domain magnetization may change its orientation. This makes the total free energy change until it reaches equilibrium (Sun,1991).
The free energy density of a strained cubic magnetic system is given in MKS units :

$$\begin{aligned} f &= f_{crystal} + f_{me} + f_{elastic} + f_{Zeeman} \\ &= K_1(\alpha_1^2\alpha_2^2 + \alpha_2^2\alpha_3^2 + \alpha_3^2\alpha_1^2) + K_2\alpha_1^2\alpha_2^2\alpha_3^2 \\ &\quad + B_1(\alpha_1^2 e_{xx} + \alpha_2^2 e_{yy} + \alpha_3^2 e_{zz}) + B_2(\alpha_1\alpha_2 e_{xy} + \alpha_2\alpha_3 e_{yz} + \alpha_3\alpha_1 e_{zx}) \\ &\quad + \frac{1}{2}C_{11}(e_{xx}^2 + e_{yy}^2 + e_{zz}^2) + \frac{1}{2}C_{44}(e_{xy}^2 + e_{yz}^2 + e_{zx}^2) + C_{12}(e_{xx}e_{yy} + e_{yy}e_{zz} + e_{zz}e_{xx}) + \ldots\ldots \quad (2.3.1) \\ &\quad - M \bullet B^* \end{aligned}$$

where α_i's are direction cosines between the magnetization vector and crystal coordinate system, e_{ij}'s are strain components, K_i's are the cubic anisotropy constants and B_1, B_2 are magnetoelastic coupling coefficients. The terms proportional to the K's in Eq. (2.3.1) describe the anisotropy energy density in an unstrained material. The line terms that depend on both strain and direction cosines represent the magnetoelastic energy density

f_{me}. The line terms depend on elastic constants (C_{ij}'s) and strains describe pure elastic energy density. The fourth line represents Zeeman or field energy.

From Eq.(2.3.1), we can get a mathematical definition of magnetoelastic coupling coefficient as the strain derivative of the free energy:

$$B_{ij} = \frac{1}{\alpha_i \alpha_j} \frac{\partial f_{me}}{\partial e_{ij}} \tag{2.3.2}$$

We can include the strain dependent free energy in the more familiar thermodynamic expression for the Gibbs free energy.

$$G = U - ST - e\sigma - B^* H \tag{2.3.3}$$

where U is internal energy, S is entropy, T is temperature, e is strain, σ is stress, B^* is magnetic flux density and H is the magnetic field in MKS units. The asterisk is used with the magnetic flux density to distinguish it from the magnetoelastic coupling coefficient, B. From the Maxwell's thermodynamic relationship of Eq (2.3.3) and Gibbs-Duhem relationship,

$$\left(\frac{\partial H}{\partial e}\right)_{\sigma} = \left(\frac{\partial \sigma}{\partial B^*}\right)_{H} \tag{2.3.4}$$

By integrating this, we obtain Eq.(2.3.5),

$$\sigma(B^*) - \sigma(0) = \int_0^{B} \left(\frac{\partial H}{\partial e}\right)_{\sigma} dB^* \tag{2.3.5}$$

where

$$B^* = \mu_0(M + H) \quad \text{and} \quad \sigma = eE. \quad \text{Here E is Young's elastic modulus.} \tag{2.3.6}$$

From Eqs.(2.3.5) and (2.3.6), we obtain Eq.(2.3.7).

$$\sigma(B^*) - \sigma(0) = \int_0^{\mu_0 M} \mu_0 \left(\frac{\partial H}{\partial e}\right)_{\sigma} dM \tag{2.3.7}$$

Thus

$$e(B^*) - e(0) = \int_0^m \frac{\mu_0 Ms}{E}\left(\frac{\partial H}{\partial e}\right)_\sigma dm \qquad (2.3.8).$$

The integral in Eq.(2.3.8) is proportional to the field difference between two m-H curves taken at slightly different strains, integrated from $m_i = 0$ to some arbitrary value m.

Further, another general result can be obtained through the condition, $\partial f/\partial e_{ij} = 0$ if magnetostrictive strain depends upon rotation of the magnetization vector, not on wall motion (Sun and O'Handley, 1991).

$$e(B)=(B/3E)(4m^2(H)-1) \qquad (2.3.9)$$

where B is a saturation ME coupling coefficient.
From Eq(2.3.8) and (2.3.9), we can get Eq(2.3.10).

$$-\frac{B}{3}\left[\frac{4m^2(H)-1}{E(H)} - \frac{4m^2(0)-1}{E(0)}\right] = \int_0^m \frac{\mu_0 Ms}{E}\left(\frac{\partial H}{\partial e}\right)_\sigma dm \qquad (2.3.10).$$

We can neglect the ΔE effect because the imposed strain is much greater than the magnetostriction in our experiment, then we get Eq.(2.3.11)

$$B = -\frac{3}{4}\frac{\mu_0 Ms}{m^2(H)-m^2(0)}\int_0^m \left(\frac{\partial H}{\partial e}\right)_\sigma dm \qquad (2.3.11)$$

We can evaluate Eq.(2.3.11) at two convenient $m_1 < m < m_2$ field values and take the difference. Thus the ME coupling coefficient B_{ij} is related to the e_{ij} derivative of the m-dependent field integrated over an arbitrary magnetization range and normalized to the difference in the square of the fields at those magnetization limits.
If we define the area difference between the m-H loops

$$\Delta A = \int_0^m \left(\frac{\partial H}{\partial e}\right)_\sigma dm \qquad (2.3.12)$$

then

$$B = -\frac{\mu_0 Ms\Delta A}{(1+\nu)[m^2(H) - m^2(0)]} \qquad (2.3.13).$$

Eq(2.3.13) is consistent with the equations in other cases (e.g. polycrystalline and single crystals).

The significance of Eq.(2.3.13) is illustrated in Fig.(2.3.2). The integral is simply the difference between two m-H curves evaluated at two different strain levels, integrated from m_1 to m_2. This equation is useful for evaluating B from the m-H loops including the non-saturated m-H loops and those with remanance (m_r) as long as we take any arbitary m_1 and m_2 greater than m_r. Since the hysteresis near the saturation region is much smaller than that near the initial magnetization region, the data from the approach to saturation region can be used to evaluate B more accurately.

In Eq.(2.3.13), all parameters are constant and known variables from the experimental m-H loop, except for the saturation magnetization, M_S. Actually M_S of thin films often exhibits a thickness dependence. Neither magneto-optic Kerr effect (MOKE) nor secondary electron spectroscopy with polarization analysis (SESPA) can provide an accurate absolute measure of saturation magnetization. Saturation magnetization is expected to be smaller in very thin film (Gradmann, 1974). We have examined this in polycryatalline Ni and permalloy films *ex-situ* using the vibrating sample magnetometer (VSM). First, we made a series of films of constant area with various thickness. Then we measured the saturation magnetization through the vibrating sample magnetometer (VSM). The results for polycrystalline Ni and permalloy films are shown in Fig.(2.3.3). The VSM shows considerable noise as thickness decreases, especially below the thickness of 100Å range. Thus we could not get any reliable signal below 15Å and 30Å in permalloy and Ni, respectively. The scattering below thickness of 100Å most likely have come from the reduced signal/noise ratio of VSM not from the thickness effect.

In this study, we assume that the saturation magnetization in films of all thicknesses is the bulk value. Note that the film magnetization enters Eq.(2.3.13) in such a way as to suppress the measured effective B, not enhance it. If we erroneously used a bulk value to get B, insertion of the true M_s, if it were smaller than the bulk, would suppress measured B value. Also, such an origin for the ME anomaly would not give rise to the sign change which we observed in the permalloy film series.

Generally, we can determine B at any thickness of the film through Eq.(2.3.13). For the detailed application of Eq.(2.3.13), we will show how to determine B's in the cases of

the thin films with uniaxial magnetic easy axis, isotropic magnetization and cubic symmetry.

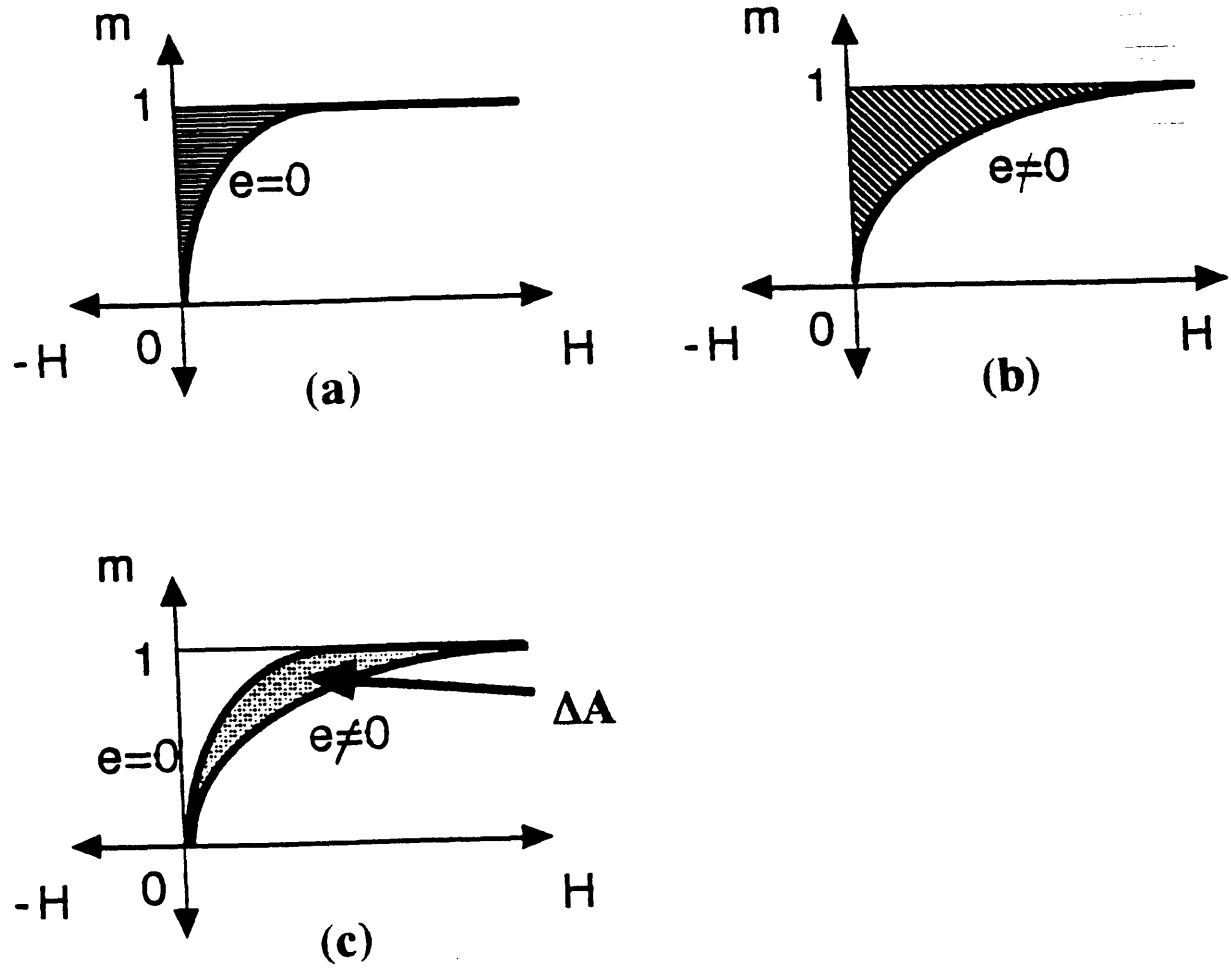

Fig.2.3.1 Change of averaged m-H loops with strain.

(a) m-H loop without external strain: the shaded area is the reference anisotropy.

(b) m-H loop with external strain: anisotropy energy increased because of the magnetoelastic anisotropy energy.

(c) the shaded area shows magnetoelastic anisotropy energy.

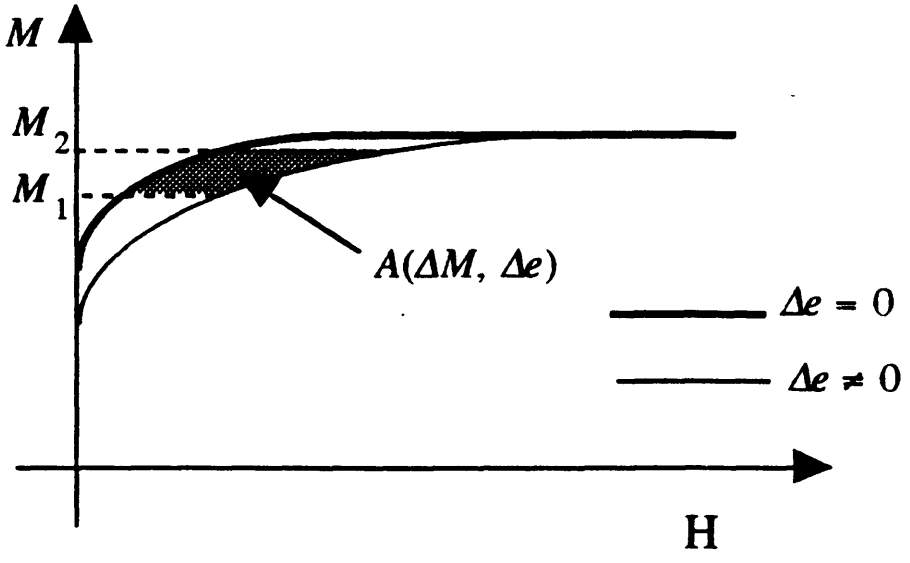

Fig.2.3.2. Illustration showing the area between unstrained and strained (the shaded area)

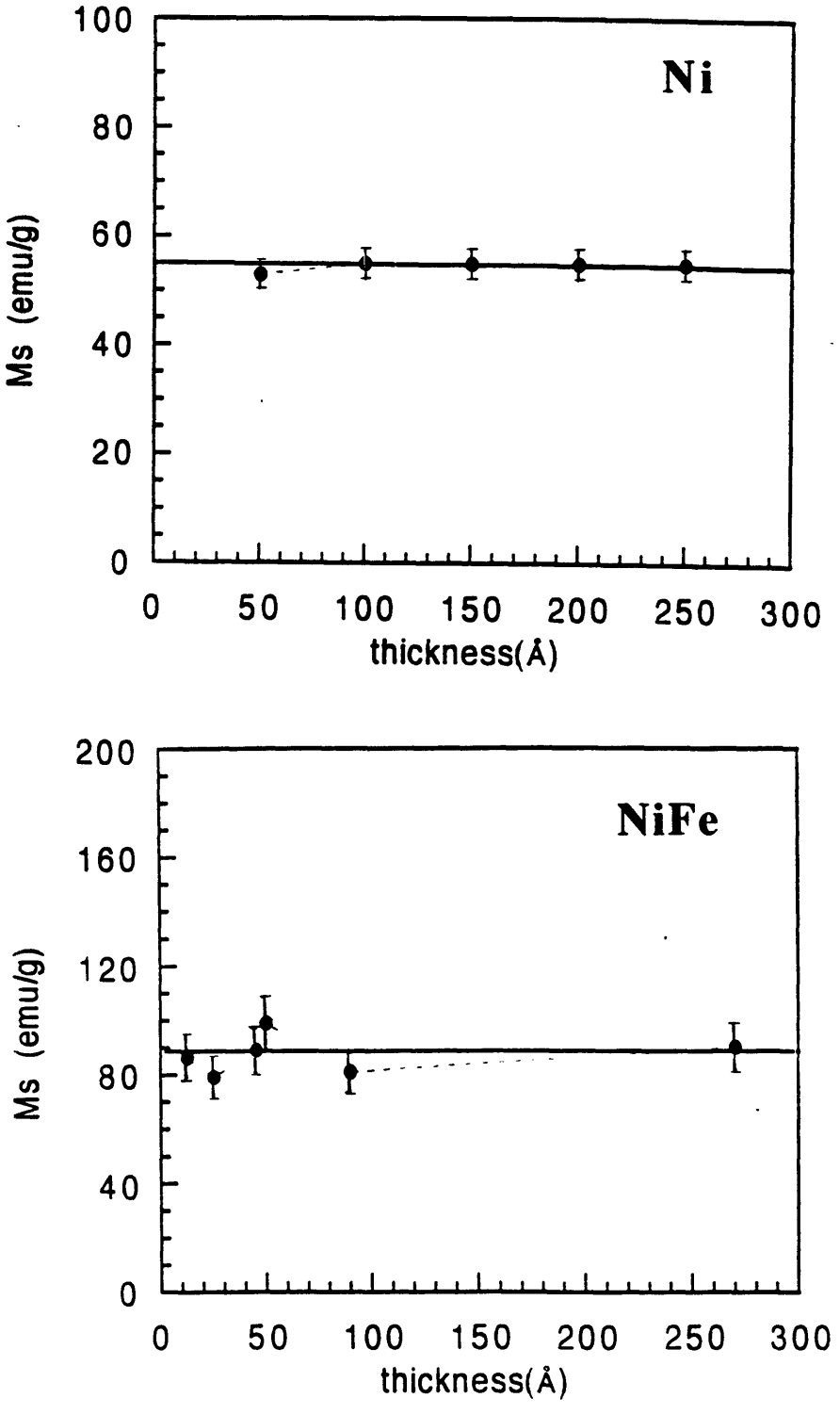

Fig.2.3.3. Ms(t) vs t in polycrystalline Ni and permalloy films (a) a plot of Ms(t) vs. film thickness in polycrystalline Ni. (b) a plot of Ms(t) vs. film thickness in polycrystalline permalloy.

2.4. Expected anhysteretic curves with strain

In order to calculate the form of an m-H loop, we need to consider all anisotropy energies and the Zeeman energy and then find the equilibrium state from the conditions $\frac{\partial F}{\partial \theta} = \frac{\partial F}{\partial \varphi} = 0$ and $F''_\theta > 0$, $F''_\varphi > 0$. In Fig.(2.4.1), we show the magnetization vector **M** in a cartesian coordinate system and define the direction cosines.

If the magnetization lies in the plane of the film (θ =90°), we only need the $\frac{\partial F}{\partial \varphi} = 0$ and $F''_\varphi > 0$ conditions. This can simplify the problem. This assumption is reasonable for polycrystalline Ni and permalloy thin films because of their large shape anisotropy. (see Table 2.4.1). Thus most of the polycrystalline magnetic films show in-plane magnetization to reduce the shape anisotopy energy .

Table 2.4.1. Magnitude of bulk anisotropy energies in Ni and NiFe films.

anisotropy energy	shape (J/m^3) $-\mu_0 M_S^2/2$	crystalline (J/m^3) K_1	magnetoelastic(if $e=10^{-3}$)(J/m^3) $B_1 e$
nickel	-1.35×10^5	4.5×10^4	6.2×10^3
permalloy	-1.5×10^5	≈ 0	≈ 0

The free energy density of the unstrained Ni film in zero field is given by the crystalline and magnetostatic anisotropy terms.

$$F = K_1\left(\alpha_1^2\alpha_2^2 + \alpha_2^2\alpha_3^2 + \alpha_3^2\alpha_1^2\right) + K_2\alpha_1^2\alpha_2^2\alpha_3^2 \qquad \text{(crystalline anisotropy)}$$
$$+ \frac{\mu_0 M_s}{2}\alpha_3 \qquad \text{(magnetostatic anisotropy)} \qquad (2.4.1)$$

and $\frac{\partial F}{\partial \theta} = \frac{\partial F}{\partial \varphi} = 0$ gives φ = 45° (because $K_1 < 0$), and θ = 90°. This means that we expect our Ni and permalloy thin films to have an in-plane magnetization. More

discussions on how to calculate the anhysteretic m-H curves with the above assumptions will be shown below.

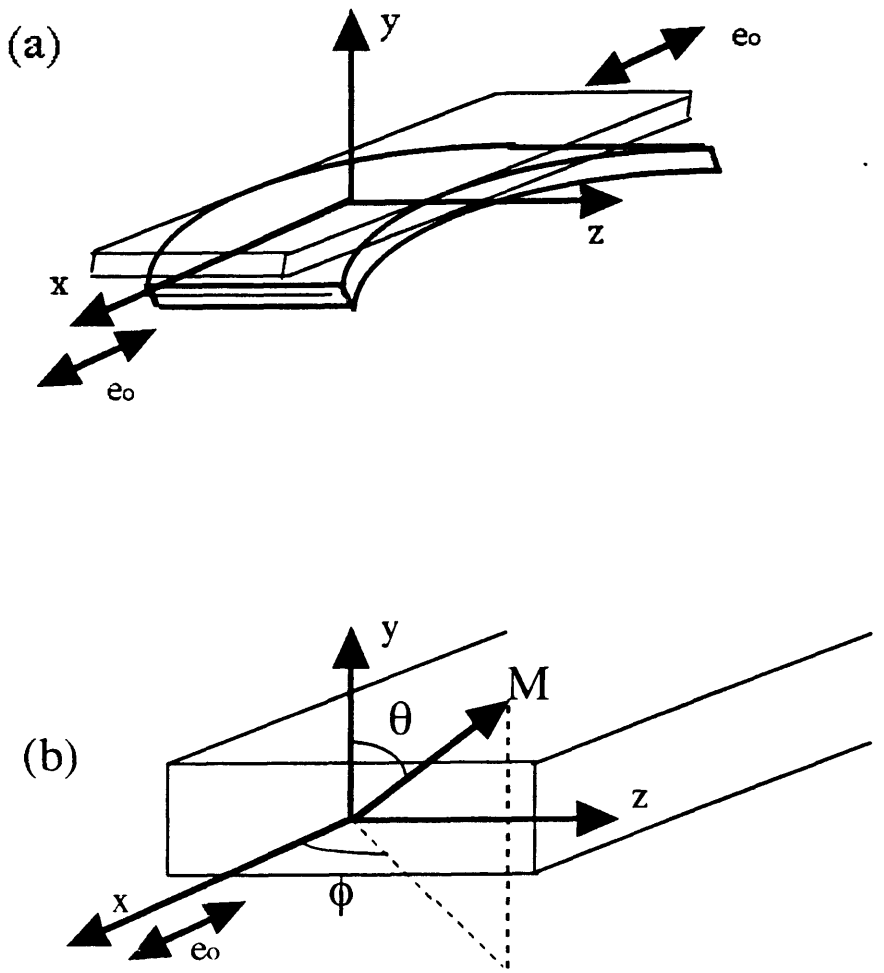

Fig.2.4.1 Magnetization vector and coordinate system.

$\alpha_1=\sin\theta\cos\phi$, $\alpha_2=\sin\theta\sin\phi$, $\alpha_3=\cos\theta$.

(a) Coordinate system for (100) film whose ME coupling coefficients are to be determined by four-point bending. Four-point bending subjects the surface film as sample tensile strain e_o.

(b) Arbitary magnetization vector and direction cosines in cartesian coordinate system.

2.4.1.Uniaxial easy axis

First, we can think about the uniaxial anisotropy case as shown Fig.(2.4.1.1). Note that the strain and external magnetic field are parallel to the magnetic easy axis. The total free energy density is:

$$\begin{aligned} F &= K_0 + K_u \sin^2\varphi && \text{crystalline anistropy} \\ &+ B_1 e\left(\cos^2\varphi - \nu\sin^2\varphi\right) && \text{magnetoelastic anistropy} \\ &- \mu_0 M_s H_{ex}\cos\varphi && \text{Zeeman energy} \end{aligned} \qquad (2.4.1.1)$$

At equilibrium $\dfrac{\partial F}{\partial \varphi} = 0$ with $m = \cos\varphi = \dfrac{M}{M_s}$ (2.4.1.2)

we get the relationship:

$$m = \frac{\mu_0 M_s}{2\left[K_u + Be(1+\nu)\right]} H_{ex} \qquad (2.4.1.3)$$

In Fig. (2.4.1.2), we plot m as a function of Hex both for e = 0 and e ≠ 0. We have defined b = Be and show b > 0.

From Eq.(2.4.1.3), the magnetoelastic coupling coefficient is given as a function of the change of the area (ΔA) in two different m-H loops and the imposed strain (Δe) :

$$B = \frac{\mu_0 M_s \Delta A}{(1+\nu)\Delta e} \qquad (2.4.1.4)$$

Thus we can get B easily if we know Δe and ΔA from the m-H loop measurements at different strain state, and provided we have the data on saturation magnetization, M_s, with film thickness. As Eq.(2.4.1.4) has simple linear relationship with B and ΔA, it may be enough to measure the effective saturation field (H_K^{eff}) to get B as shown in Eq.(2.4.1.5). We can express the effective saturation field as :

$$H_K^{eff} = H_K + \frac{2(1+\nu)B\Delta e}{\mu_o M_s} \qquad (2.4.1.5)$$

Fig.(2.4.1) is a schematic of an ex-situ MOKE experimental set up for the polycrystalline Ni film on textured Cu substrates. The Ni film is 1200Å thick and has a uniaxial magnetic easy axis parallel to the external field. A yoke type holder is needed to strech the Cu substrate which, in turn, exerts a tensile strain of up to 10^{-3} on the Ni film.

Fig.(2.4.3) is the result of the *ex-situ* m-H loops of the Ni films with imposed uniaxiual strains of zero and 10^{-3}. The square loop without imposed strain changes into rotated loop with tensile strain. The change of the loops according to strain is consistent with the expectation as shown in Fig.(2.4.2)

From the data shown in Fig.(2.4.1.3), we get $B = 6.0 \times 10^6$ J/m^3 using Eq.(2.4.1.4). This value compares favorably with the bulk value of B_1 for Ni, $B_1 = 6.2 \times 10^6$ J/m^3.

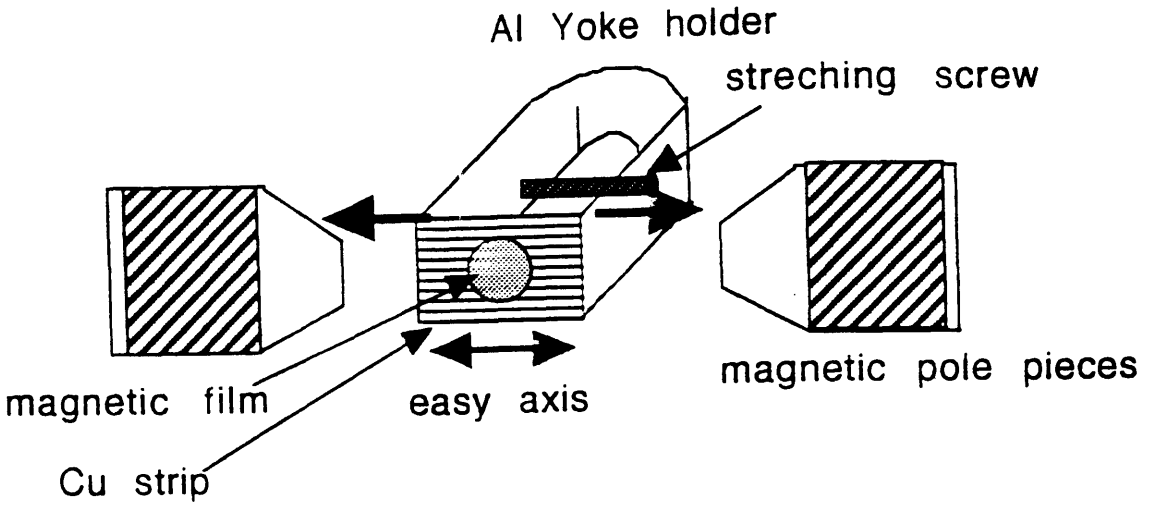

Fig.2.4.1.1. Experimental setup in a uniaxial magnetic easy axis case. Polycrystalline Ni of thickness 1200 Å is deposited on textured Cu strip, and streched by a yoke-type holder actuated by a bolt.

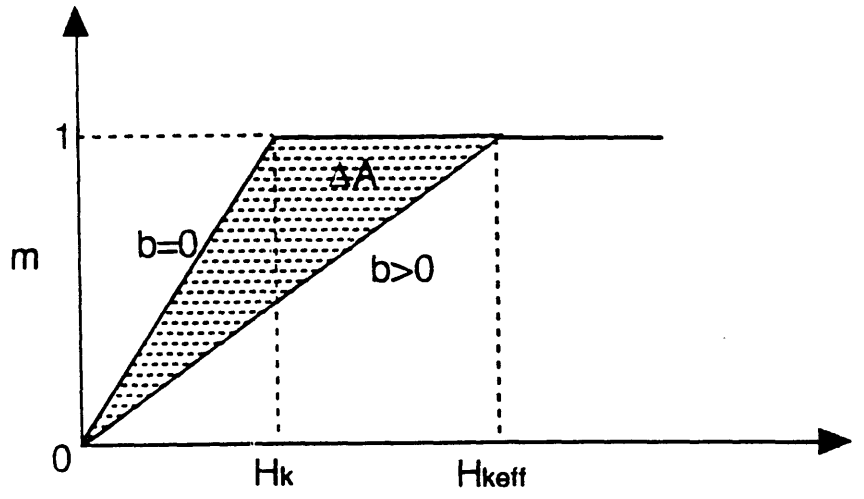

Fig.2.4.1.2. The expected m-H curves in an uniaxial magnetic easy axis with respect to strain. Where b=Be.

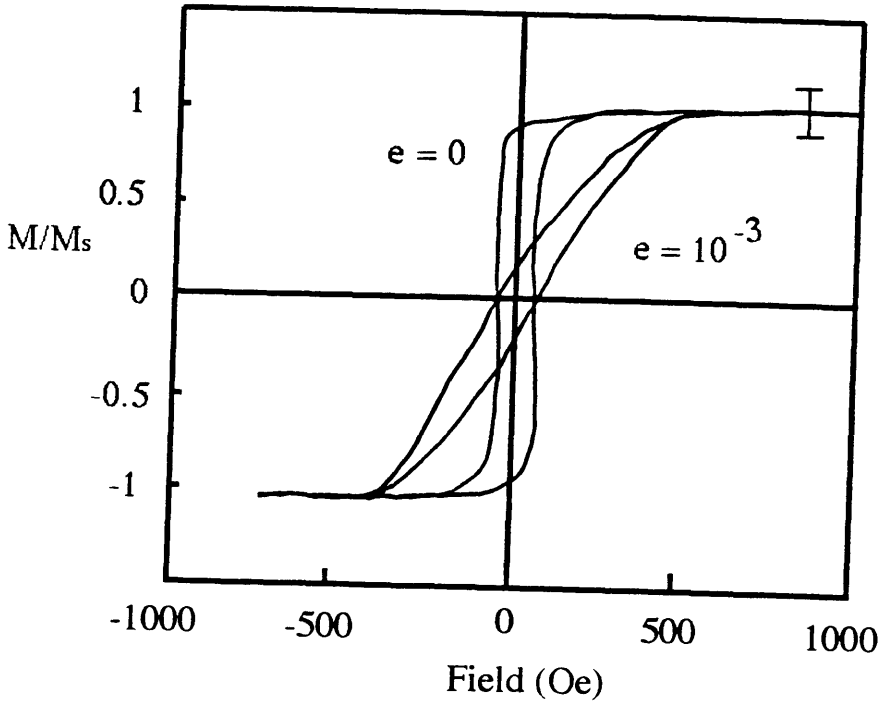

Fig.2.4.1.3. Real MOKE hysteresis loops with various strain.

2.4.2. Isotropic polycrystalline magnetic films

It is somewhat difficult to derive relationships like those in section 2.4.1 because total free energy expressions can not be described in a simple way. S. Németh(1992) and Lachowicz(1984) showed how to determine magnetostriction coefficients on polycrystalline and amorphous strips on thick films. We need to know how each randomized magnetic domain interacts with the external magnetic and strain fields. Therefore we would like to treat the magnetization as an average over a distribution (Sablik and Jiles, 1993). This approach makes use of a generalized Langevin function in a manner similar to several treatments of amorphous and polycrystalline materials.

In the anhysteric state, which describes thermodynamic equilibrium, the polycrystalline material is treated as a collection of magnetic domains, each carrying magnetic moment $\vec{m}$. The distribution of domains at temperature T carries a total magnetization M in the field direction given by

$$< M > = \frac{\int_0^{\pi} M_s \cos\theta e^{-E_d(\theta)/K_B T} \sin\theta d\theta}{\int_0^{\pi} \theta e^{-E_d(\theta)/K_B T} \sin\theta d\theta} \qquad (2.4.2.1)$$

where θ is the angle between domain moment $\vec{m}$ and applied field H, and M_S = Nm is the saturation magnetization of N domains per unit volume as shown in Fig.(2.4.2.1). $E_d(\theta)$ is the domain energy in the presence of the magnetic and strain fields of the other domains and in the presence of external field H. The effect of interaction between domains can be represented as an effective contribution to the magnetic field,

$$E_d(\theta) = -\mu_0 m H_e \cos\theta \qquad (2.4.2.2)$$

where the effective field H_e is,

$$H_e = H + \alpha M + H_\sigma \qquad (2.4.2.3)$$

The contribution αM to effective field arises from magnetic interaction between domains and the contribution H_σ arises from magnetoelastic interaction between domains. The coupling parameter α can be expressed in terms of saturation magnetization, saturation

magnetostriction, and elastic constants and can be determined experimentally (M. Sablik ,1993). From thermodynamic relationship, in the case of orthogonal stress and magnetic field,

$$G = U - TS - \frac{3}{2}\lambda\sigma + \mu_o MH$$
$$U = \frac{1}{2}\alpha\mu_0 M^2 \qquad (2.4.2.4)$$

where G is the Gibbs free energy density, U is internal energy density. It follows that the effective field H_e is

$$H_e = \frac{1}{\mu_0}\left(\frac{\partial G}{\partial M}\right)_T = H + \alpha M - \frac{3}{2}\frac{\sigma}{\mu_0}\left(\frac{\partial \lambda}{\partial M}\right)_T \qquad (2.4.2.5)$$

Comparing Eq.(2.4.2.3) with Eq.(2.4.2.5), we have

$$H_\sigma = -\frac{3}{2}\frac{\sigma}{\mu_0}\left(\frac{\partial \lambda}{\partial M}\right)_T \qquad (2.4.2.6)$$

where λ is the bulk magnetostriction under applied field H.

If we define $a = Nk_BT/\mu_oM_s$, then the solution of eq(2.4.2.1) is given by:

$$M = M_S \mathbf{L}(H_e/a) \qquad (2.4.2.7)$$

where $\mathbf{L}(x)=\coth(x)-1/x$ is the Langevin function. We assume the number of domains, N, is constant. We can take the following values as reasonable for polycrystalline Ni (Sablik, 1993):

a=3000, α=6.87 10^{-5}, μ_oM_s=0.6 Tesla , λ=-3.4x10^{-5}, E=2.5 x 10^{11} J/m^3. Because $\lambda = 3/2\,\lambda_S(\cos^2\theta - 1/3)$, we can write $\partial\lambda/\partial M = 2(\lambda_s/M_s^2)M = 2(\lambda_s/M_s)m$. The results of Eq.(2.4.2.7) are shown in Fig.(2.4.2.2) for several values of strains.

Thus, it is possible to predict the behavior of m-H loops with respect to strain even in isotropic polycrystalline magnetic materials. This prediction is in fact consistent with our general principle shown in section 2.3 and later results of polycrystalline NiFe and Ni films (see section 4).

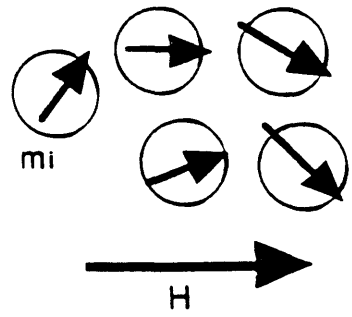

Fig.2.4.2.1. Arbitary domains (m) and external field (H).

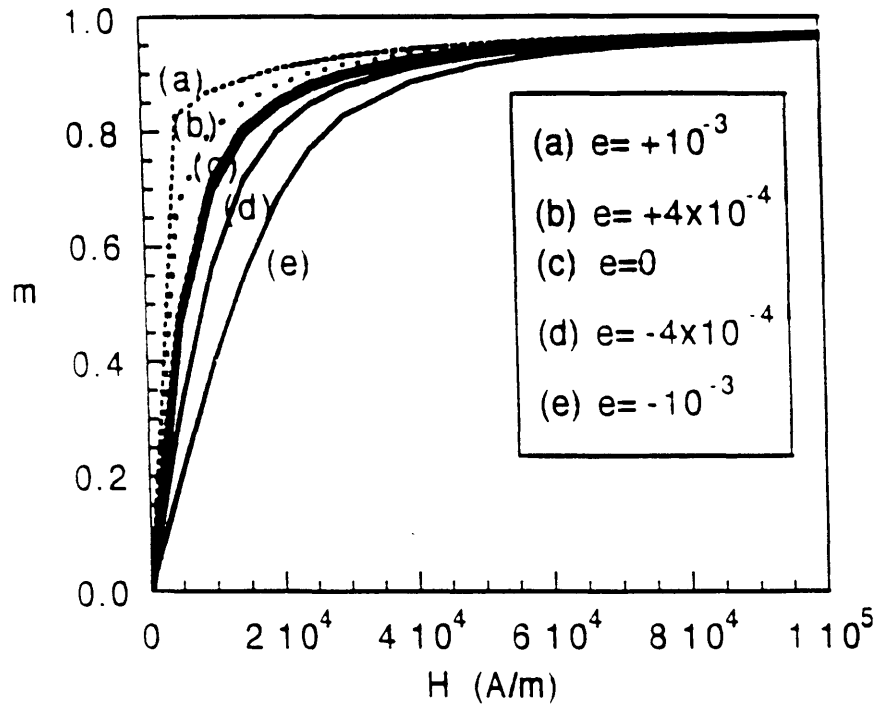

Fig.2.4.2.2. Expected m-H loops of polycrystalline Ni with respect to various strain ($e= +4\times10^{-4}$, $+1\times10^{-3}$).

2.4.3. Cubic symmetry

In cubic symmetry, we can express the crystalline anisotropy energy density (f_K) and magnetoelastic energy (f_{ME}) as Eq.(2.2.1),(2.2.2) respectively. This means we need B_1 and B_2 to express single crystal magnetoelastic energy instead of one B as in the isotropic case.

For the coordinate suystem as shown in Fig.(2.4.3.1), we can express the total free energy as Eq.(2.4.3.3),

$$\begin{aligned} F = {} & K_1 \sin^2\varphi\cos^2\varphi && \text{crystalline anisotropy energy} \\ & + B_1 e\left(\sin^2\varphi - \nu\cos^2\varphi\right) && \text{ME anisotropy energy} \\ & - \mu_0 M_s H_{ex}\cos\varphi && \text{Zeeman energy} \end{aligned} \qquad (2.4.3.1)$$

and to satisfy the equilibrium condition, $\dfrac{\partial F}{\partial \varphi} = 0$ with $m = \cos\varphi = \dfrac{M}{M_s}$ (2.4.3.2)

we must have:

$$-m\left[2K\left(2m^2 - 1\right) + 2B_1 e(1+\nu)\right] = \mu_0 M_s H_{ex} \qquad (2.4.3.3)$$

If we plot m vs. H_{ex} from the Eq.(2.4.3.3) for various strains, we obtain Fig.(2.4.3.2). We define b = Be. The plot illustrates that, without imposed strain, the m-H curve has the expected remanance of $(1/2)^{1/2}$. However, as strain increases for $b < 0$, the remanance decrease until it becomes zero for curve 3 in Fig.(2.4.3.2)

As was done in the uniaxial easy axis case, we can express B_1 in the zero remanance cases as shown in curves 3 and 4 in Fig.(2.4.3.2) as :

$$B_1 = \frac{\mu_0 M_s \Delta A}{(1+\nu)\Delta e} \qquad (2.4.3.4)$$

In the range of $m_r < m < 1$ (and $m_r > 0$) as shown in the curves 1 and 2 in Fig.(2.4.3.2), we can expressn B_1 (see Eq.(2.3.13)):

$$B_1 = \frac{\mu_0 M_s \Delta A}{(m_2^2 - m_1^2)(1+\nu)\Delta e} \qquad (2.4.3.5)$$

Finally, for the range $m_r > 0$, we can express B in terms of m_r (H = 0) and crystalline anisotropy constant (K_1) as :

$$B_1 = \frac{-K_1(2m_r^2 - 1)}{(1+\nu)\Delta e} \qquad (2.4.3.6)$$

This means we can idenify crystal anisotropy constants for cubic symmetary and this can be even applied to a study to find magnetocrystalline anisotropy constants, K's, with respect to different thicknesses (K(t)).

With the same approach, we can get B_2 by bending a (100) Ni film toward [110] direction as shown in Fig (2.4.3.3)(a) because we can produce shear strains.
We have shear strain by rotation of crystallographic axis as shown in Eq.(2.4.3.6). Then the total free energy density would be Eq.(2.4.3.7).

$$e_{ij} = e_0 \begin{bmatrix} \frac{1-\nu}{2} & \frac{1+\nu}{2} & 0 \\ \frac{1+\nu}{2} & \frac{1-\nu}{2} & 0 \\ 0 & 0 & -\nu \end{bmatrix} \qquad (2.4.3.7)$$

$$\begin{aligned} F = {} & K_1 \cos^2\varphi \sin^2\varphi \\ & + B_1(e_{11}\cos^2\varphi + \sin^2\varphi) + B_2 e_{12} \sin\varphi\cos\varphi \\ & - \frac{\mu_0 M_s H_{ex}}{\sqrt{2}}(\cos\varphi - \sin\varphi) \end{aligned} \qquad (2.4.3.8)$$

At equilibrium , $\frac{\partial F}{\partial \varphi} = 0$

we get the relationship

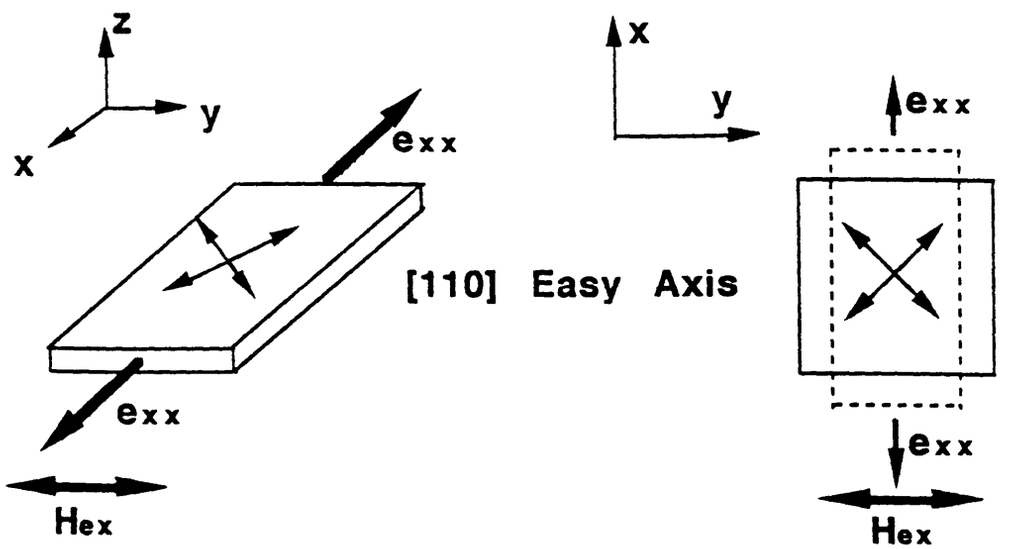

Fig.2.4.3.1. Experimental setup to determine B_1 in a single cubic crystalline symmetry.

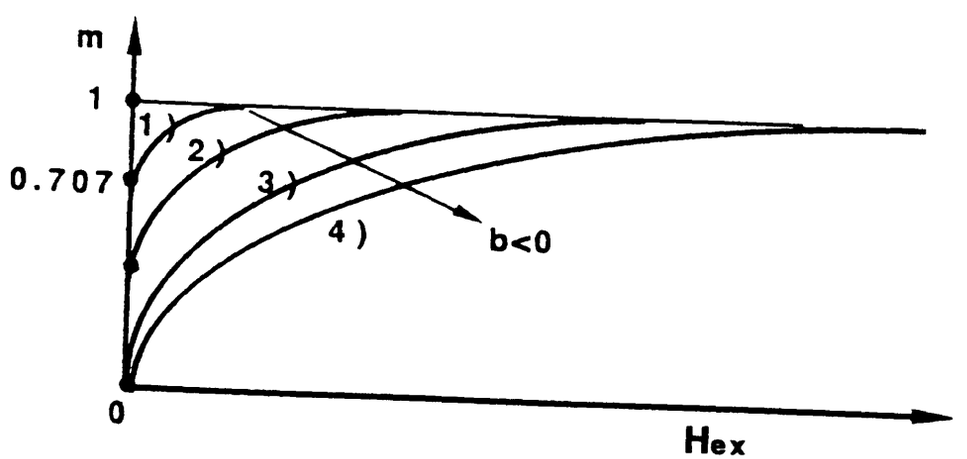

Fig.2.4.3.2. The expected m-H loops with various strains in a cubic symmetry.
Where b=Be.

1) e = 0 2) e = -3×10^{-4} 3) e = -5×10^{-4} 4) e = -10×10^{-4}

$$H_{ex} = \frac{m}{\mu_0 M_s}[K_1(1-2m^2) + B_2 \frac{(1+\nu)}{2} e_0] \qquad (2.4.3.9)$$

We can illustrate the plot of m vs. H_{ex} from the Eq.(2.4.3.8) for various strains in Fig.(2.4.3.4). The plot shows that m has the expected remanance of 0.707 without imposed strain. As strain increases, the remanances decrease until it becomes zero.

From the Eq.(2.4.3.8), we can get the relationship of Eq.(2.4.3.9) in the zero remanance cases such as the curves 3 and 4 in Fig.(2.4.3.4):

$$B_2 = \frac{2\mu_0 M_s \Delta A}{(1+\nu)\Delta e} \qquad (2.4.3.10)$$

Similarly, for the range $0 < m_r <$ (arbitary m_1 amd m_2) < 1 (e.g. curves 1 and 2 in Fig.(2.4.3.8)), we can express B_2 from the m-H loops with the remanances through Eq.(2.3.13) in section 2.3.:

$$B_2 = \frac{2\mu_0 M_s \Delta A}{(m_2^2 - m_1^2)(1+\nu)\Delta e} \qquad (2.4.3.11)$$

Again , if the m-H loops have remanances such as in the curves 1 and 2, we get the K_1 from the Eq.(2.4.3.11):

$$B_2 = \frac{2K_1(2m_r^2 - 1)}{(1+\nu)\Delta e} \qquad (2.4.3.12)$$

From Eq(2.4.3.9) to (2.4.3.11), we can get $B_2(t)$ and $K_1(t)$ if we measure the m-H loops under different strains with respect to film thickness (t).

In conclusion, we propose a new method to determine $B_1(t)$, $B_2(t)$ and even $K_1(t)$ with two different m-H loops measured at different strain states. It is a new and unique mehod of prediction and interpretation of m-H loops in single crystals. Although the magnetostriction coefficients of numerous bulky single crystals had been measured (Bozorth, 1954), this is a new method to find magnetostriciton coefficients and even magnetocrystalline coefficients with respect to film thickness.

One major assumption in the above derivation is that the film retains cubic crystalline symmetry even in the very thin regime. This may not be true because of surface relaxation in thin films. To treat this problem more generally, we need to allow for the fact that a few top mono-layers of the film have lower symmetry than the bulk (that is, bulk cubic becomes tetragonal symmetry below thickness of a few nm). We consider the tetragonal symmetry in Appendix B.

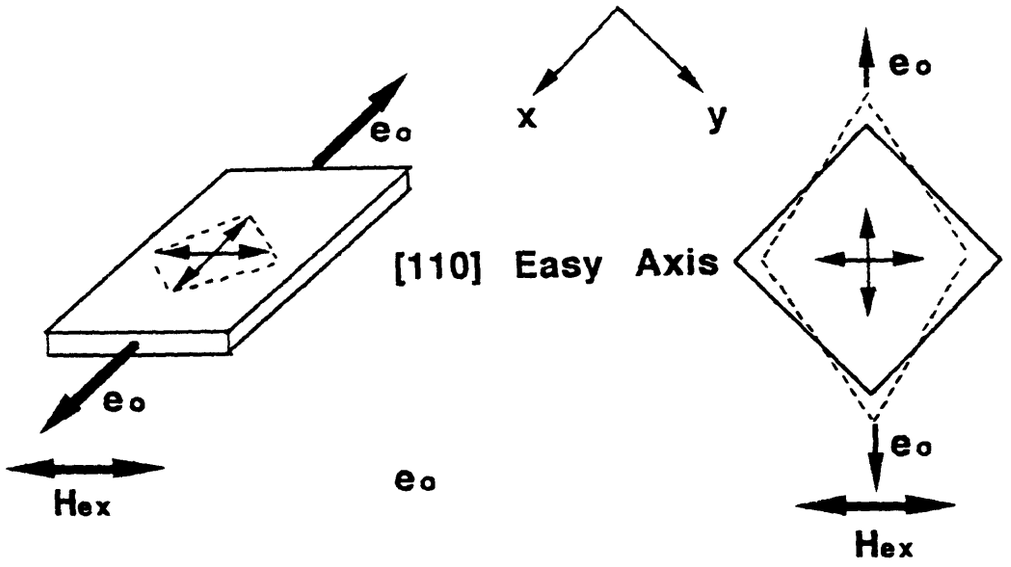

Fig.2.4.3.3. Experimental setup for B_2.

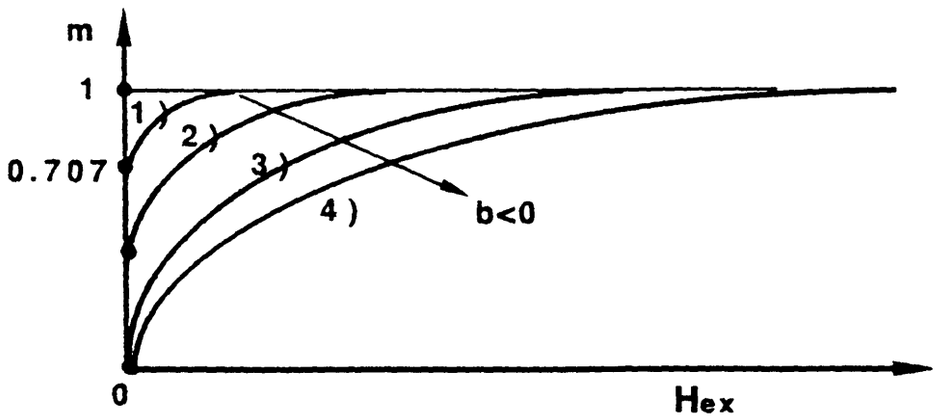

Fig.2.4.3.4. m-H loop behavior in single crystalline Ni film with shear strain to get B_2.

Where b=Be.

1) e = 0 2) e = -3×10^{-4} 3) e = -5×10^{-4} 4) e = -10×10^{-4}

2.5 Néel model

We now describe the Néel model which gives a microscopic meaning to the phenomenological energy density terms used so far to describe surface effect. This treatment follows that of the Chuang *et al* in reference. Néel (1954) proposed that atoms in reduced symmetry, such as at a surface, will give rise to anisotropies that are different from the bulk anisotropy in the material. We made the following assumptions to predict the effective B with the Néel model. First, we consider no surface relaxation and no thickness dependence of the strain, although significant surface relaxation (up to 10% by Davis 1992) is involved because of the lowered symmetry and misfit strains at the interface have large inverse thickness dependence. Second, we assume an ideal interface without intermixing between the substrate and magnetic film, and no magnetic interaction between the substrate and film; but an irregular interface is expected because of chemical intermixing . Third, we do not account for the exchange coupling between surface and bulk. However, the surface spins can be pinned by large surface magnetoelastic anisotropy and can occur the exchange coupling with interior spins. This will be discussed in section 5. Fourth, only nearest neighbor interactions are considered. Although we made the above assumptions for the Néel model calculations, the Néel model allows us to predict the trends of B as film thickness decreases.

In the Néel model, the magnetic pair interaction energy (w(r,φ)) between atoms is expanded in Legendre polynomials (L.Néel , 1954)(S. Chikazumi, 1986):

$$w(r,\phi) = G(r) + L(r)(\cos^2\phi - \frac{1}{3}) + Q(r)(\cos^4\phi - \frac{6}{7}\cos^2\phi - \frac{3}{35}) + \cdots \quad (2.5.1)$$

where r is interatomic distance and ϕ is the angle between the bond axis and M_s as shown in Fig.(2.5.1). The first term is independent of the direction of magnetization, so it describes any isotropic effects such as exchange. The second term has the symmetry of the dipole-dipole interaction, which depends on the direction of magnetization, and may describe uniaxial anisotropy of any origin. The third, quadrupolar term describes anisotropy of cubic symmetry. The coefficients of Eq.(2.5.1) are functions of the distance, r, between the pairs of magnetic atoms, and can be expanded in terms of bond strain as Eq.(2.5.2),

$$L(r) = L(r_o) + (dL/dr) \cdot e \cdot r_o + \ldots \qquad (2.5.2)$$

where r_o is the bulk unstrained bond length.

The values of $L(r_0)$ and $Q(r_0)$, as well as their variation with the bond length (e.g. $(dL/dr)r_o$) can be related to the magnetocrystalline anisotropy constant K_1, and the magnetoelastic coefficients B_1 and B_2 of the bulk material (S. Chikazumi,1964). The second nearest neighbor interactions are often ignored because the interaction strength should decrease with bond length. This should be a good approximation for Ni and Co where the d-electron are well localized and the number of second nearest neighbor is eight versus twelve nearest neighbors. However, it may not as good in Fe where the d-electrons are not as tightly localized as in Co or Ni and the nearest neighbor number is eight.

The Néel coefficients for fcc Ni have been calculated, using bulk values of K_1, B_1 and B_2 at 298K, from the following relationship.(S. Chikazumi,1964).

$$K_1 = Q(r_o)$$
$$B_1 = 3L(r_o) + (dL/dr)r_o / 2$$
$$B_2 = 2L(r_o) + (dL/dr)r_o \qquad (2.5.3)$$

These coefficients are listed in Table 2.5.1. along with coefficients for bcc Fe.

Table 2.5.1. Anisotropy constant K_1, magnetoelastic coupling coefficients B_1, B_2 for fcc Ni (at 298 K) and bcc Fe (at 298K) and the Néel model parameters derived from them (Chuang, 1994)

	K_1 10^6 erg/cm^3	$Q(r_0)$ 10^6 erg/cm^3	B_1 10^8 erg/cm^3	B_2 10^8 erg/cm^3	$L(r_o)$ 10^8 erg/cm^3	$(dL/dr)r_o$ 10^8 erg/cm^3
fcc Ni	-0.045	-0.045	0.62	0.8	0.1	0.6
bcc Fe	0.47	0.26	-0.29	0.71	-0.11	0.91

We can find the bulk and surface contribution to the anisotropy energy by summing the pair interaction energy Eq.(2.5.1) over the nearest neighbors in each cluster.

The anisotropy energy density for a film is then given by:

$$E^{eff} = E^{bulk} + E^{surface}/t \qquad (2.5.5)$$

where E^{bulk} and $E^{surface}$ are in units of energy/volume and energy/area respectively. t is the film thickness. The effective anisotropy energy in thin films is given by a sum of bulk anisotropy and surface anisotropy which is inversely proportional to film thickness. Néel (1954) introduced the idea that surface anisotropy goes as one over the thickness (t). This term expresses the fact that as the film thickness increases, surface atom make up a smaller fraction of the total film volume. For a detailed derivation of Eq.(2.5.5), see Chuang et al (1994).

For fcc Ni(100) films, we can distinguish bulk and surface atomic sites in the film as indicated in Fig.(2.5.2). Each type of site contributes in a different way to magnetic anisotropy because of different nearest neighbor symmety. Bulk fcc Ni atoms have 12 nearest neighbors as shown in Fig. (2.5.2(a)). The symmetry of a surface is reduced compared to that of bulk because four nearest neighbor bonds are broken in the creation of the surface as shown in Fig. (2.5.2(b)). The resulting nearest neighbor cluster around a surface atom in a thin film contains only eight atoms instead of twelve atoms. (Fig. 2.5.2(c)). The effective anisotropy energy of Ni(100) film can be calculated by considering the interaction energy of eight nearest neighbors with an external uniaxial strain tensor of Eq.(2.4.4.4). Then we have the anisotropy energy which is given as a form of Eq.(2.5.5).

$$K^{eff} = f\,(L(r_o), (dL/dr)\,r_o, e) + \{g\,((L(r_o), (dL/dr)\,r_o, e)\}/t \qquad (2.5.6)$$

Eq.(2.5.6) is the same form as Eq.(2.5.5) and the first term indicate the bulk anisotropy and the term which is inversely proportional to film thickness is from the surface symmetry. Both bulk and surface terms are functions of the Néel model parameters ($L(r_o)$, $(dL/dr)\,r_o$) and the strain. Néel model parameters are known constants as shown in Table 2.5.1.

Since B is defined as the partial derivative of anisotropy energy with respect to strain ($B = \partial K/\partial e$), we can express B as Eq(2.5.7) from the derivative of Eq.(2.5.6) with respect to strain :

$$B_i = f'(L(r_o), (dL/dr)\, r_o) + \{g'((L(r_o), (dL/dr)\, r_o)\}/t \qquad (2.5.7).$$

Eq.(2.5.7) is the general form of the effective magnetoelastic coupling coefficient and identical to Eqs.(2.5.5) and (2.5.6). First term is B^b and the term which is inversely proportional to film thickness indicate B^s/t. In Eq.(2.5.7), both B^b and B^s are functions of only the Néel parameters. We can determine magnitues and signs of the B^b and B^s through the above procedure even different surfaces and strain tensors in any other cubic symmetry.

We would like to take an example of the Néel model application for our purpose. Let us consider strain that is uniform throughout the thickness of the film, such as due to unrelieved misfit between the film substrate in Ni/Cu (100) which has 2.6% lattice mismatch. This Ni/Cu(100) system is of interest because we can compare the results by the Néel model calculation with those from the Cu/Ni/Cu(100) epitaxial films in section 4.4. The misfit strain in the film has the form of :

$$e = e_0 \begin{vmatrix} 1 & 0 & 0 \\ 0 & 1 & 0 \\ 0 & 0 & -2\nu/(1-\nu) \end{vmatrix} = e_0 \begin{vmatrix} 1 & 0 & 0 \\ 0 & 1 & 0 \\ 0 & 0 & -1 \end{vmatrix} \qquad (2.5.8)$$

where e_0 is the misfit strain, $e_0 = (a_{substrate} - a_{film}) / a_{substrate}$, and Poisson's ratio (ν) is assumed to be 1/3.

Using these assumptions, we can calculate $B^{eff}{}_1(t)$ from the (100) surface of the Ni/Cu(100) system. Since only principal strain involved in Eq.(2.5.8), we expect the result of $B^{eff}{}_1$. First, we can evaluate the effective interaction energies of the (100) surfaces of the Ni film with a given strain tensor, Eq.(2.5.8). The anisotropy energy of (100) surface of the eight nearest neigbors under strain tensor of Eq.(2.5.8) can be calculated with Eq.(2.5.1) and is given as the form of Eq.(2.5.6). Since $B^{eff}{}_1(t)$ is defined as the partial derivative of anisotropy energy with respect to principal strain (e_{ii}), we can evaluate B1 from the effective interaction energy. The result is shown in Table 2.5.2. Similarly, if we consider (111) surface of Ni/Cu(111) system with biaxial misfit strain, then we can obtain $B^{eff}{}_2(t)$ because this surface is related only shear strains (e_{ij}) as will be shown in Eq.(4.4.2). With the same methodology, we can calculate the $B^{eff}{}_2$. The result is also shown in Table 2.5.2.

Table 2.5.2. Bulk and surface magnetoelastic coupling coefficients for cubic structures in the (100) and (111) surface coordinate system. (in Ni/Cu system)
(100) surface gives $B^{eff}{}_1(t)$
(111) surface gives $B^{eff}{}_2(t)$

		B^{bulk}	$B^{surface}/t$
(100) system	$B^{eff}{}_1(t)$	$3L(r_o)+(1/2)(dL/dr)r_o$	$[-1.5L(r_o)]/t$
(111) system	$B^{eff}{}_2(t)$	$2L(r_o)+(dL/dr)r_o$	$[-L(r_o)-(1/8)(dL/dr)r_o]/t$

Thus the ME coupling coefficients in single crystal Ni/Cu can be given as :

$$B^{eff}{}_1(t) = [6.2 - 5.25/t(\text{Å})]\ (\text{x}10^6\ \text{J/m}^3)$$
$$B^{eff}{}_2(t) = [8 - 6.1/t(\text{Å})]\ (\text{x}10^6\ \text{J/m}^3) \qquad (2.5.9)$$

for the case of biaxial misfit strain. The results of Eq(2.5.9) are illustrated in Fig.(2.5.3). This shows $B^{eff}{}_1(t)$ and $B^{eff}{}_2(t)$ of epitaxial fcc-Ni can change sign near the surface. We will see in section 4.4 that the results in Fig.(2.5.3) are consistent with those of the epitaxial Ni films with Cu capping layer (Cu/Ni/Cu(100)) except for the thickness scale. The thickness scale may be recalibrated by considering the exchange interaction between surface and bulk. More detailed discussions on possible origins of thickness scale shifts will be found in section 5.

Thus, given the strain states of films, the Néel model allows us to predict that B^{eff} is the sum of B^{bulk} and the surface term, $B^{surface}/t$, while determining the sign and magnitude of B^{bulk} and $B^{surface}$ in a single crystal.

Single crystal Ni with biaxial strain shows that B_i's can decrease from positive to negative values as thickness decreases due to the lowered symmetry at the surfaces.

So far, the Néel model does not include the exchange anisotropy energy between the surface and bulk or the intermixing at the interface. These may be the major reasons why the $B^{surface}$ contribution can be significant only below thickness of 10Å range with this simple model. The possible contributions of the exchange coupling and intermixing layers will be discussed in section 5.

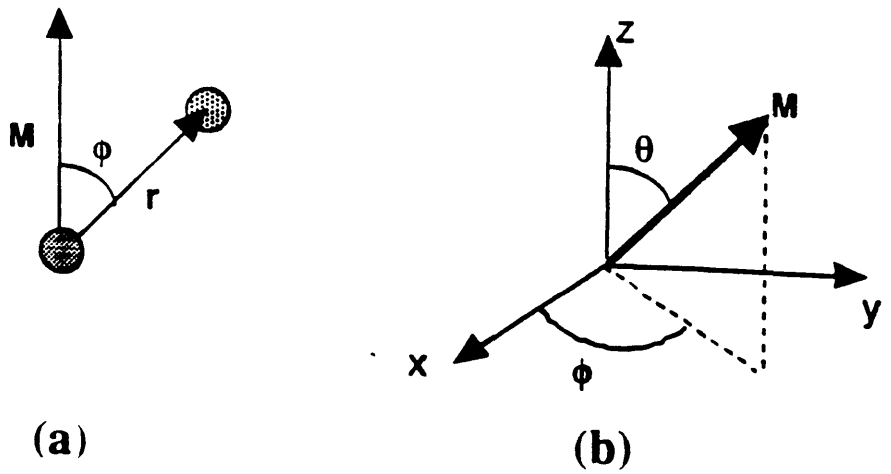

Fig.2.5.1. Interaction between two magnetic atoms and coordinate sysem.

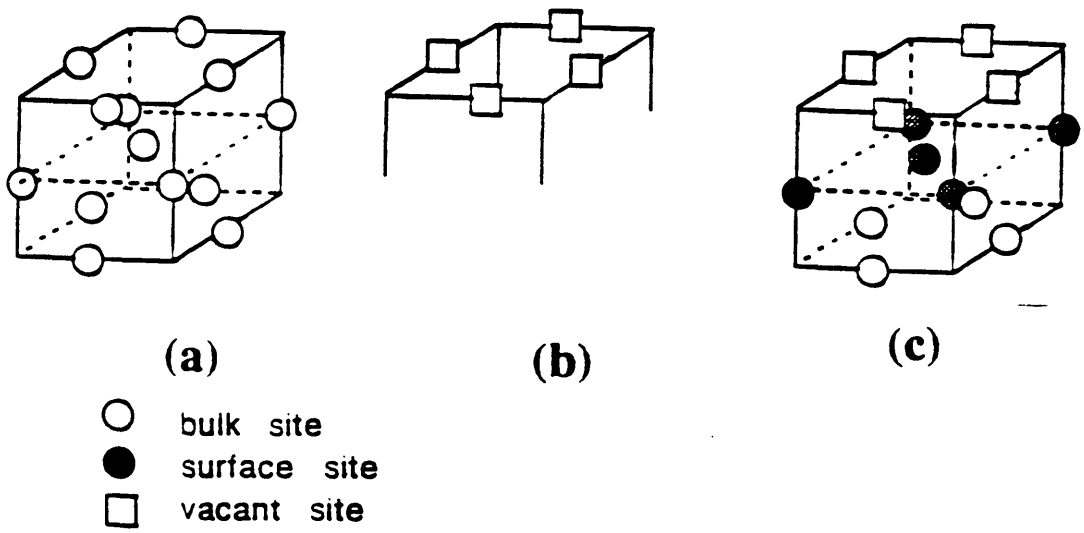

Fig.2.5.2. Illustration of bond symmmetry of fcc-thin films.

(a) Nearest neighbor cluster around bulk fcc atoms

(b) Vacant sites due to creation of surface

(c) Nearest neighbor cluster around surface fcc atoms

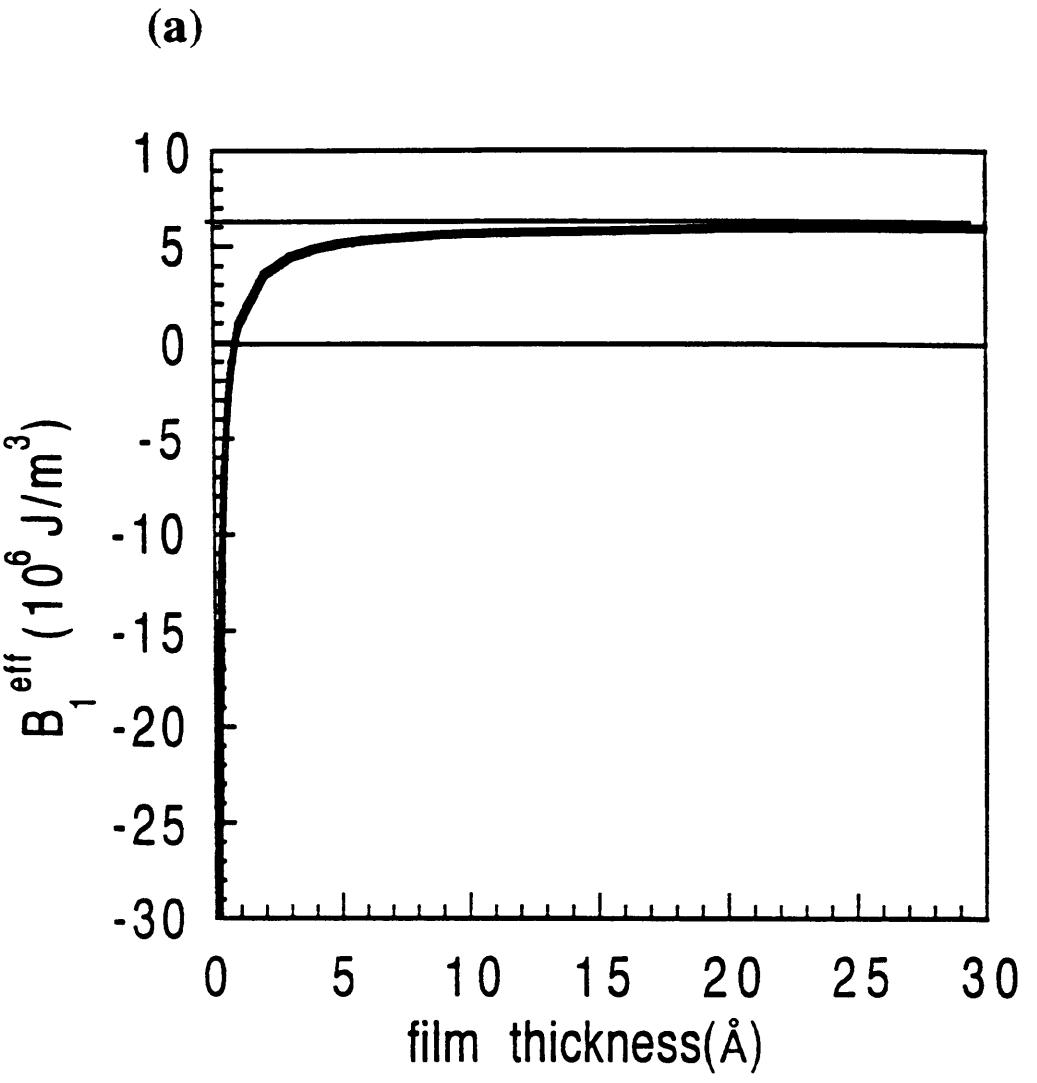

Fig.2.5.3. Illustration of B's with respect to film thickness under biaxial misfit strain: single crystal Ni under biaxial strain
(a) $B^{eff}{}_1(t) = [6.2\text{-}5.25/t(Å)]$ $(x10^6\ J/m^3)$

(b)

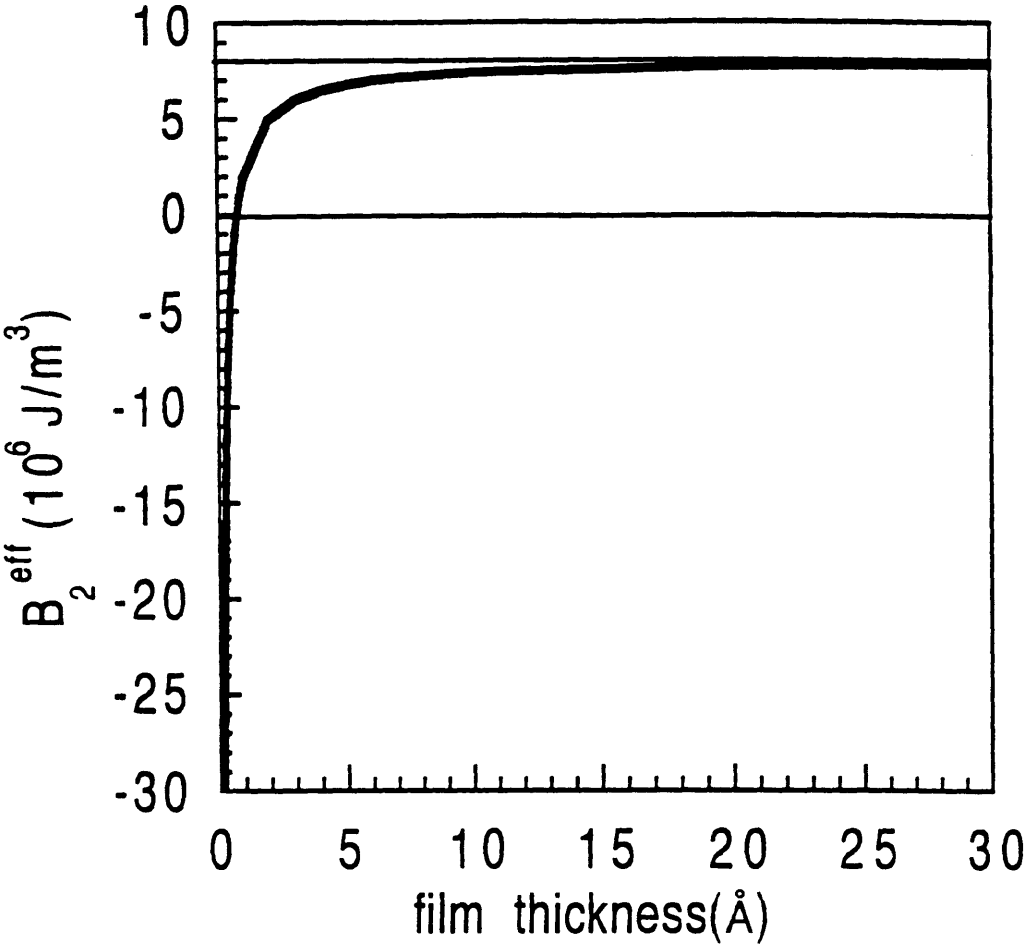

(b) $B^{eff}_2(t) = [8\text{-}6.1/t(Å)]$ ($x10^6$ J/m^3)

3. Experimental procedure and instrumentation

3.1. Overall view of experiment

The overal view of experimental procedure is as follows. We first measure m-H loops *in situ* on a film subject to no applied strain using magneto-optic Kerr effect (MOKE). A bulk measurement technique such as torque magnetometry or vibrating sample magnetometry (VSM) may be used if the film can be protected from atmospheric contamination. These unstrained loops establish the operative anisotropy constants (assuming M_S is determined independently by using VSM as shown in Fig.(2.3.3)), and provide a guidance in selecting strain and field directions for ME coupling coefficient measurements. m-H loops taken with different applied strain through 4-point bending, Δe, and field combinations allow determination of all the B's as shown in section 2.3.

We showed the top view of our experimetal facilitiy in Fig.(3.1.1). When studying thin films, the film must be kept free of contaminants during all stages of experiments. In order to obtain such cleanliness, the growth and characterization of these magntic films were performed under ultra-high vacuum (UHV). The chamber is equipped with a mechanical roughing pump, a turbo pump and a ion pump which provide the base pressure of 1×10^{-8} Torr. The four-point bending sample hoder is mounted on a rotatable platform which is capable of 360° rotation. It is used to position the sample for the various experiments such as evaporation, Auger spectroscopy, and magneto-optic Kerr effect (MOKE) measurement etc. Auger spectroscopy is used to monitor substrate cleanliness and film deposition. Three magnetic pole pieces inside the chamber give capabilities of longitudinal and polar MOKE measurements.

Here is an example of measurement of magnetoelastic coupling coefficient (B) in polycrystallne permalloy films (permalloy/ 2000Å Ag/ Si(100)). We prepared a silicon substrate measuring 0.5 x 3.2 cm cut from a 2" Si(100) wafer. The thickness of the wafer was 0.025 cm. The intermediate silver (Ag) layer was deposited on the prepared wafer in another chamber which was equipped with e-beam evaporator. The base pressure of this chamber was set around 10^{-6} Torr and the deposition rate was 5Å/sec. The thickness of the Ag layer was 2000Å. After that, this substrate was transferred to our chamber as shown in Fig.(3.1.1). The permalloy source, with composition $Ni_{79}Fe_{21}$, was a rod of diameter 0.1 inch.

Then we deposited permalloy film using e-beam evaporator with rate of 0.5Å/min. Similary, to make our Ni films, 99.995% Ni rod source was used. The evaporation rate of Ni was 0.5 Å/min.

After deposition of a desired thickness of film, MOKE measurements were performed. Upon getting a MOKE signal, we found the magnetic easy axis through the longitudinal and polar MOKE measurements. This is shown schematically in Fig.(3.1.2) where panels (a) and (b) represent loops in either longitudinal or polar fields. Fig.(3.1.2) (a) and (b) show the magnetic film has in-plane easy axis. We obtained here a reference m-H loop without external imposed strain. Then we applied external tensile or compressive strain to the sample by manipulating the 4-point bending holder. Therefore we could get another m-H loop at different strain through MOKE as shown in Fig.(3.1.2).(c). The m-H loops would change according to strain as we expected in section 2.4.2.

To verify the result of MOKE measurements, we used the same composition of the films ($Ni_{79}Fe_{21}$) with various thicknesses of polycrystalline permalloy films on a silver/silicon wafer substrate as shown in Fig.(3.1.3).(a) using a mask with e-beam evaporation. The diameter of the magnetic film is 0.2 inch. The holder for the vibrating sample magnetometer (VSM) is made of Kel-F ^{TM} 81 Platic PCTFE (homopolymer of chlorofluoroethylene) to reduce the background noise and is designed to apply tensile and compressive strain ($\pm 1.5 \times 10^{-3}$) depending on the direction of the loading as shown in Fig.3.1.3.(c) and (d), respectively. Then we have measured the magnetoelastic coupling coefficients of these film through VSM as shown in Fig.(3.1.3).(e) with the same principle as described earlier.

Note that according to the experimental setup, we can determine the magnetoelastic coupling coefficients for the isotropic magnetic material as shown in section 2.3 and 2.4.2. The simple change of m-H loops under each strain is shown in Fig.(3.1.4). Typical real MOKE and VSM data which depend on the corresponding strain are shown in Fig.(3.1.5) and Fig.(3.1.6), respectively. By repeating the above procedure of m-H loops measurments and determining the B values as growing the films, we can measure the $B^{eff}(t)$ with respect to film thickness.

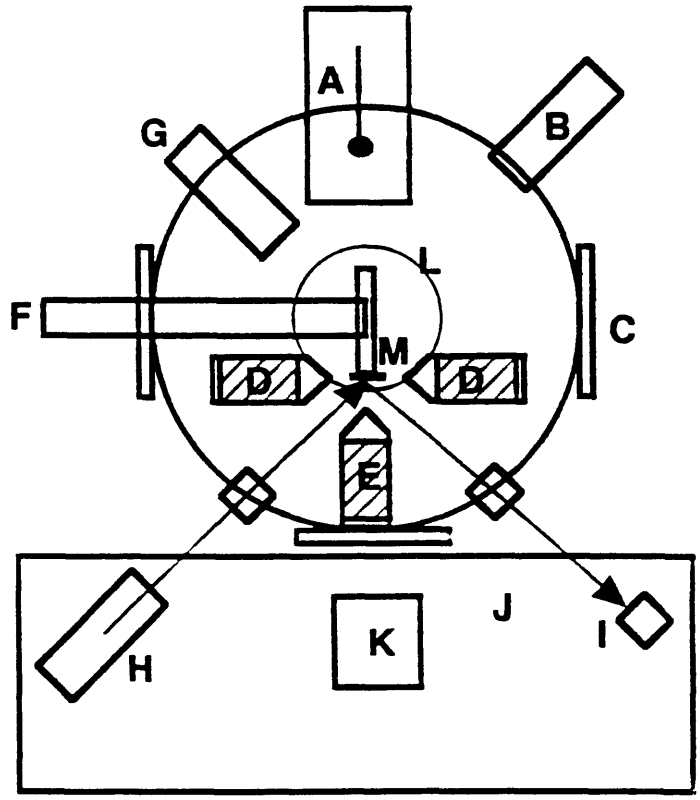

Fig.3.1.1.Schematic top view of UHV camber. Base pressure: 10^{-8} Torr
A: e-beam evaporator B: Pump line equipped with mechanical and turbo pumps.
C: Windows D: Magnets for transverse MOKE E: Magnets for polar MOKE
F: Rotatable Platform. G: Sputter gun H: Laser for MOKE
I: Photodetector for MOKE J: MOKE workbench K: Controllers.

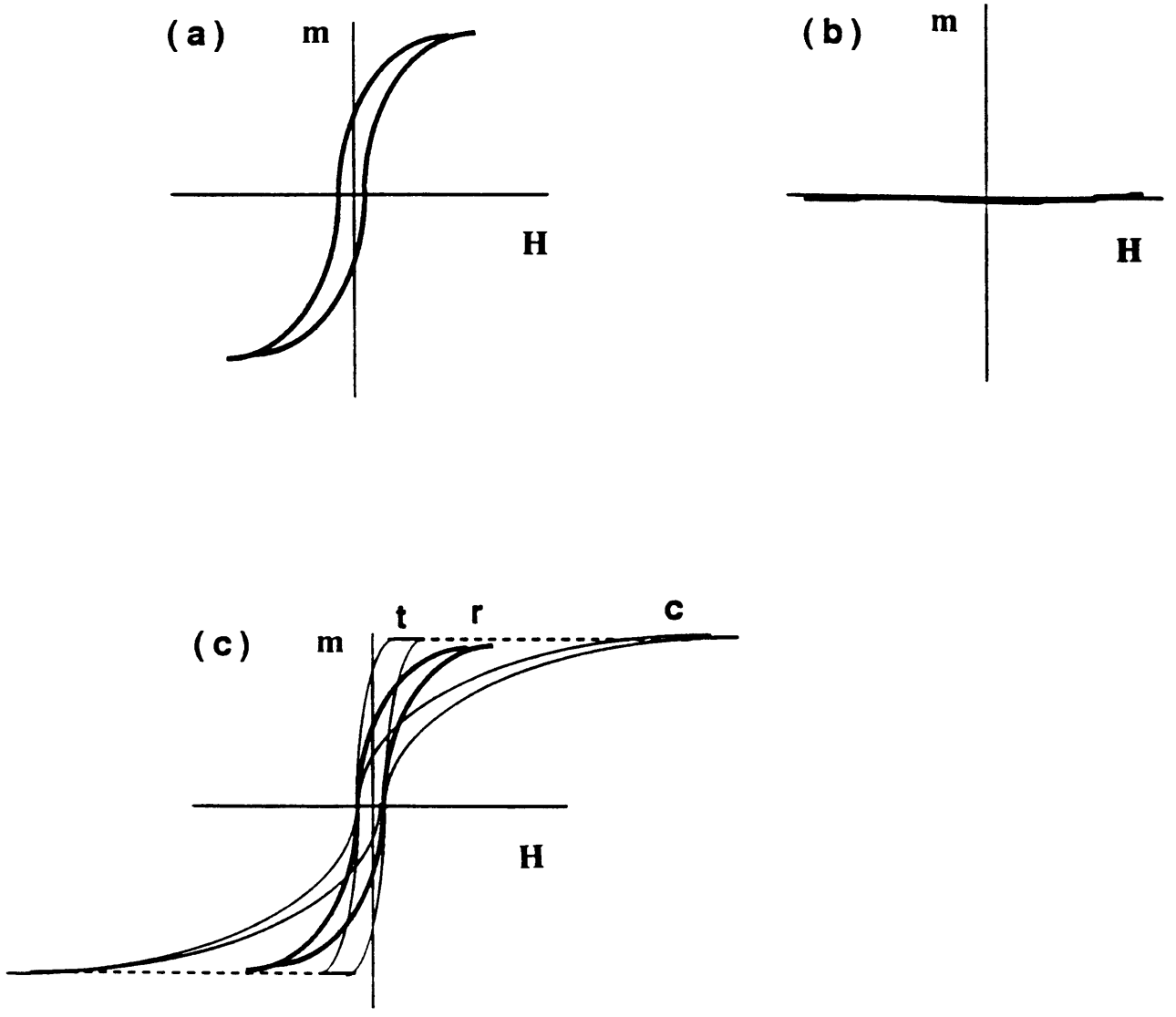

Fig.3.1.2 Schematic behavior of MOKE loop according to strain.

(a) A longitudinal MOKE loop without external imposed strain

(b) A polar MOKE loop without external imposed strain

(c) Change of MOKE loops with strain.

(r: reference loop wihout strain t: with tensile strain c: with compressive strain.)

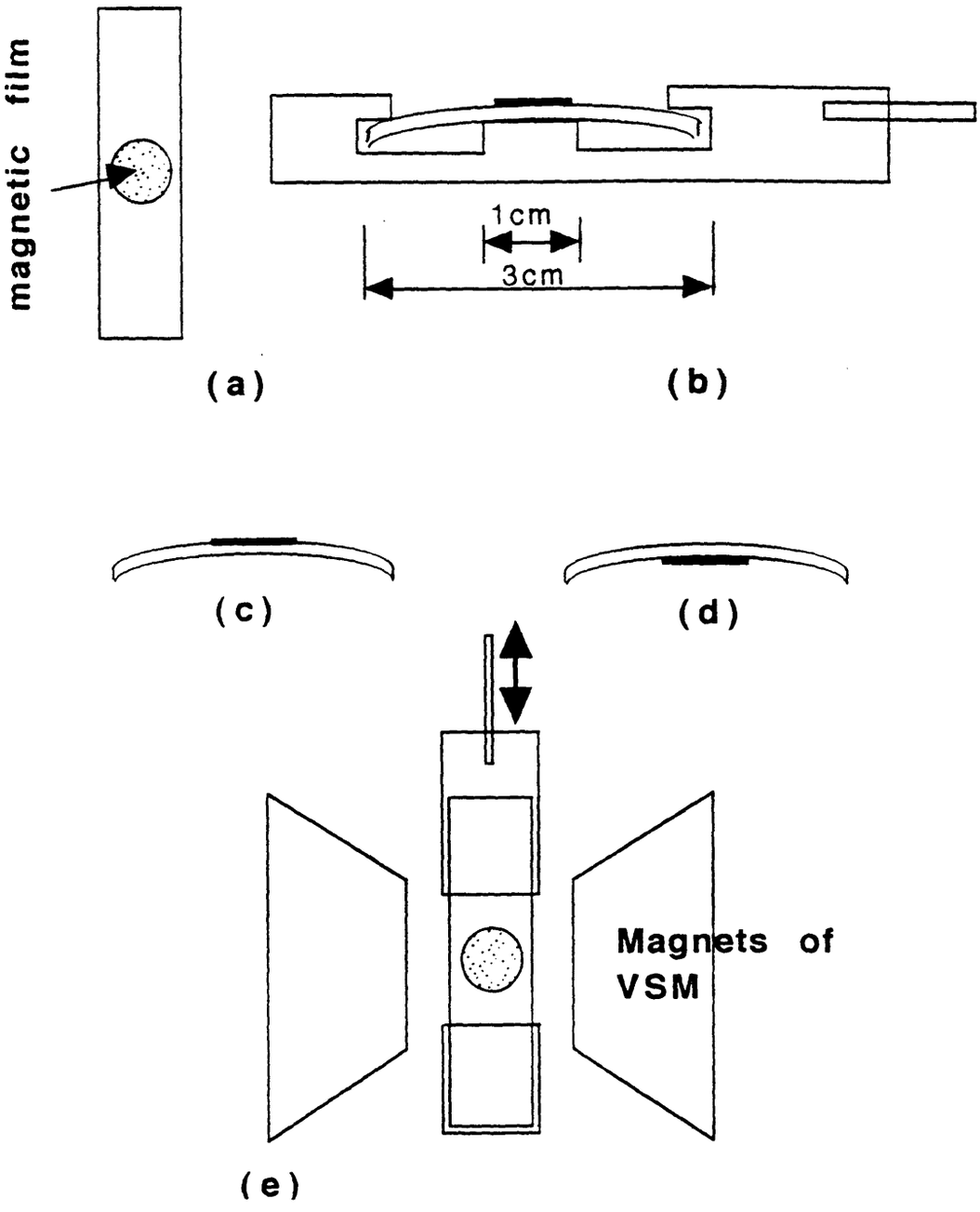

Fig.3.1.3. Schematic illustration of sample preparation for the VSM measurement.

(a) Circular magnetic films on rectangular silicon wafer.

(b) Four-point bending holder for the ex-situ VSM measurement.

(c) Bending for the tensile strain.

(d) Bending for the compressive strain.

(e) Schematic illustration of VSM measurement with holder.

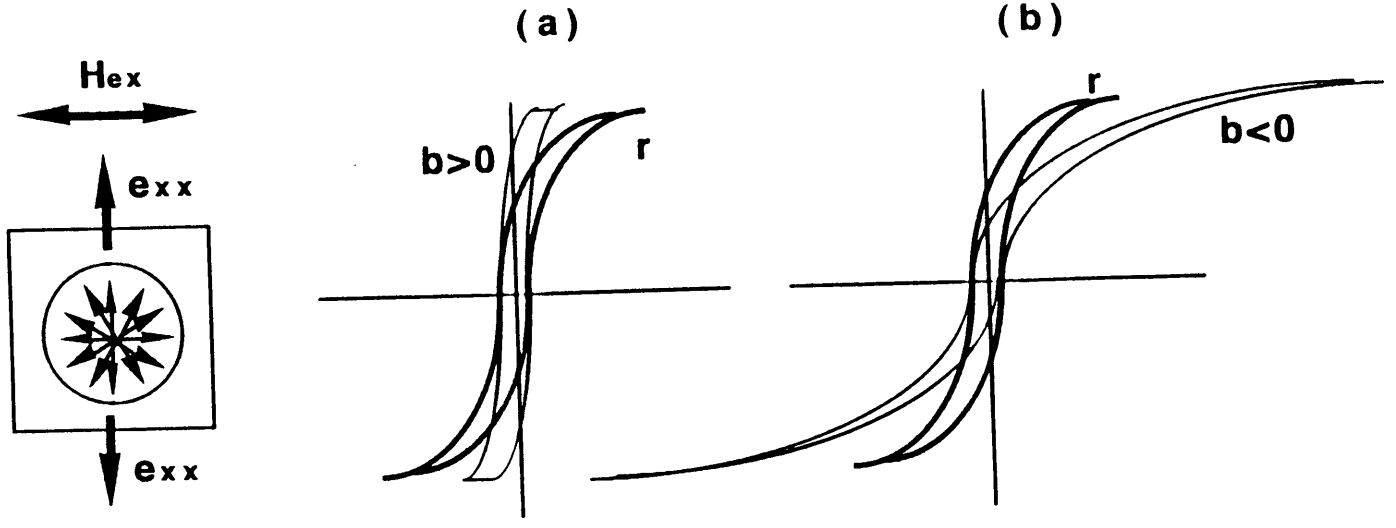

Fig.3.1.4 Schenatic diagram of expectd m-H loops according to strains.

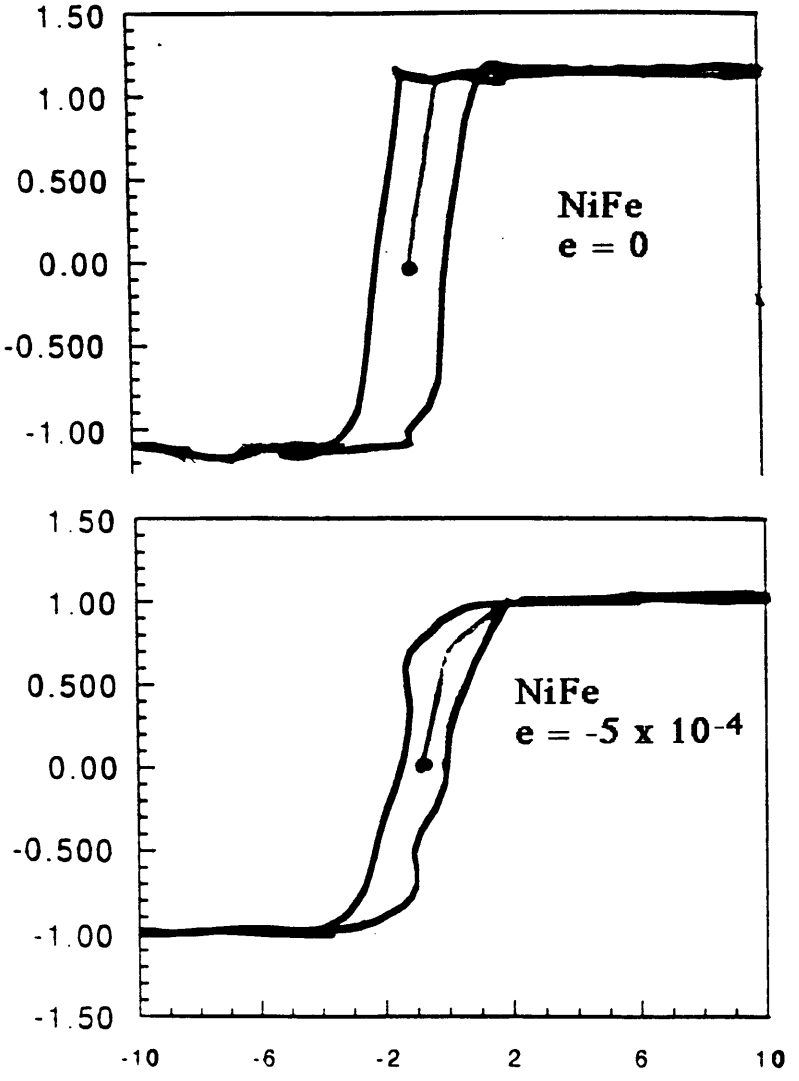

MOKE data. Permalloy 65Å /Ag/ Si(100)
above: e=0 below: e = -5 x10^{-4}

Fig.3.1.5. Measured m-H loops *in-situ* with MOKE

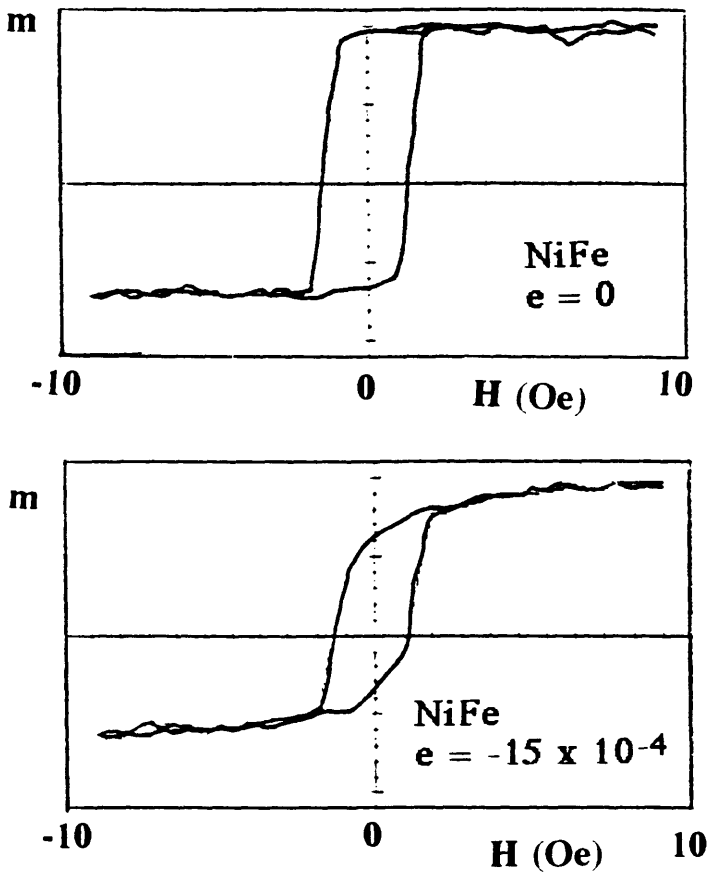

VSM data. Permalloy 45Å /Ag/ Si(100)
above: e=0 below: e = +15 x10^{-4}

Fig.3.1.6. Measured m-H loops *ex-situ* with VSM

3.2. Sample preparation

We prepared samples of four different types as shown in Fig.(3.2.1).

1) polycrystalline permalloy ($Ni_{79}Fe_{21}$)/2000Å silver/Si(100)

2) polycrystalline permalloy ($Ni_{79}Fe_{21}$)/2000Å copper/Si(100)

3) polycrystalline nickel (Ni)/natural silicon oxide(SiO_2)/Si(100)

4) Cu capping/ single crystal Ni(100)/ 2000Å Cu(100)/ Si(100)

In each case, we studied the dependence of the ME coupling coefficient on magnetic layer thickness.

Silicon wafer substrates were chosen because they are inexpensive and readily available compared to other materials. In additon, Si's well-known mechanical properties makes possible the accurate control of strain to the film. All silicon wafers were cleaned by acetone to remove organic impurities before the deposition.

In preparing the polycrystalline magnetic films, silver (Ag) is a good buffer layer to prevent silicide formation between permalloy and the silicon wafer and to keep the interface stable chemically. Copper (Cu) is also as good as silver in that regards.(Zhu, 1984). Natural silicon dioxide layers between the polycrystalline Ni and the silicon wafers are expected to function favorably in this study for it acts as a good diffusion barrior.

All polycrystalline magnetic films and intermediate layers were deposited through an e-beam evaporator. A typical deposition rate of Ni and Permalloy films was 0.5 Å/min at the base pressure of $2x10^{-8}$ Torr. The e-beam evaporation condition for depositing Ag or Cu intermediate films was 5Å/sec and 10^{-6} Torr of base pressure.

A schematic of the e-beam evaporator which was designed and built for this study is shown in Fig.(3.2.2). A tungsten (W) filament is used to supply electrons. A positive voltage is applied to a magnetic material source (Ni or permalloy rod) which accelerates the electrons from the filament to the rod. Then the energy of the electron is transferrd to the Ni or permalloy source ($Ni_{79}Fe_{21}$), melting and evaporating the tip. The Ni source is 99.995% pure and the permalloy is 99.99% pure.

E-beam evaporation is a clean deposition technique because only the tip of the rod is evaporated without any crucible and it is extensively out gassed before the evaporation.

The amount of material being deposited is monitored by a quartz crystal oscillator (QCO). The QCO is mounted close within 1 inch of the source tip. The deposition rate,

as given by QCO, is calibrated with film thickness by monitoring the growth of thick films which can be measured *ex-situ* using a step profilometry (Dek-Tak).

We can recalibrate the deposition rate by using the Herts-Knundsen equation (Holland, 1961):

$$\text{Deposition rate} = N / (2\pi r^2) \ [\#/cm^2.sec] \qquad (3.2.2.1)$$

where N is the evaporation rate expressed as $N = (2\pi m_a kT)\ P_{eq}[\#/cm^2.sec]$. Here, m_a is the mass of atom, k is Boltzman constant, T is the temperature of the source [°K], and P_{eq} is the equilibrium partial pressure of the source [Torr].

Our e-beam chamber is not equipped to characterize the growth mode or the crystallinity of the film substrate. While the intent of the experiments is not to study film growth but to probe magnetic properties, the two are interrelated.(Bruce, 1977). The growth mode is affected by such parameters as substrate temperature (Iwasaki,1978), deposition rate (Coughlin, 1981), and substrate orientation (Chambers, 1986) etc. Because the quality of the film is an important factor determining its magnetic properties (D. A. Steigerwald,1988), microstructural characterization of the magnetic films have been performed (see section 4.5).

The epitaxial Cu(100) capping /Ni(100)/Cu(100)Si(100) samples shown in Fig.(3.2.1) (d) were prepared using molecular beam epitaxy (MBE). The preparation of epitaxial films requires rigorous conditions such as removal of the surface oxide layer and impurities. The Si wafers were dipped in 10% HF-deionized water solution to remove the native oxide layer and were dried before loading the into MBE chamber. The Cu capping layer helps to prevent formation of Ni silicide and surface oxidation for *ex-situ* measurements. Moreover, these Cu layers are suitable to study misfit dislocations due to appropriate lattice mismatch (2.6%) between Ni and Cu layers (Bochi, 1994).

A few reports on epitaxial Ni layer growth are available (J. Tersoff, 1982)(M. G. Barthes, 1981)(B.T.Jonker et al, 1988)(Chang, 1992). According to Chang(1992), the epitaxial Ni(100)/Cu(100)/Si(100) system can be made by evaporation around 10^{-9} Torr.

We showed a schematic top view of the moleclar beam epitaxy (MBE) system in Fig.(3.2.3). It is equipped with two electron beam evaporators (for Ni and Cu), a load-lock, a RHEED set-up, an Auger Electron Spectroscopy (AES) apparatus and surface magneo-optic Kerr effect (MOKE) set up for *in-situ* magnetic characterization. The AES apparatus is located above the sample holder. The base pressure of the chamber was

$5x10^{-11}$ Torr and pressure never exceeded $1x10^{-8}$ Torr during deposition. The deposition rate for Cu and Ni were 3Å/s and 0.5Å/s respectively. The thickness of intermediate Cu layers was 2000Å in Cu/Ni/Cu/Si sandwich samples. The thickness of capped-Cu layer in Cu/Ni/Cu/Si was 40Å. No intentional heating was applied to the samples during deposition. The crystallographic quality and the growth orientation of the thin films were studied *in-situ* by refracted high energy electron diffractometry (RHEED). RHEED is an *in-situ* film charaterization technique capable of monitoring the structure of the films during and after growth. The RHEED electron beam is incident on the film surface at a grazing angle. The outcoming beam has a specular and diffracted component, and produces a diffraction pattern on a fluorescent screen. More details can be found in standard references.(Lagally et al, 1993).

We studied the microstructure of the polycrystalline magnetic films with transmission electron microscope (TEM). To prepare TEM specimens parallel to the film/substrate interface, samples were cut into square pieces, approximately 3x3 mm using a carbide tip. After cutting, the specimen was mounted on a polish block with crystal wax epoxy with the face of interest down. The silicon substrates were ground down to the thickness of 35 μm using 400 grit SiC paper. After cleaning the specimen in the sequence of acetone and methanol, specimens are removed from the polish block. Finally ion milling was performed in a room temperature stage at 6kV for 15 hrs. The ion beams were directed toward the specimens at an angle of 15° from the surface until the samples were transparent to electrons.

Also films of various thicknesses were grown on formvar substrates coated with carbon on 400 mesh Athene grids to investigate the morphology of the magnetic films as film thickness increases. Formvar substrates are the thin polymer films which are transparent to electrons and offer good amorphous substrates to grow the magnetic films.

TEM observation was accomplished using a JEOL200CX instrument at 200kV. Detailed theories of image interpretation for the transmission electron microscopy can be found in standard references.(Ludwig Reimer, 1984) (P. Hirsh et al., 1977). Some microstructure images were obtained using a Nanoscope III atomic force microscope (AFM).

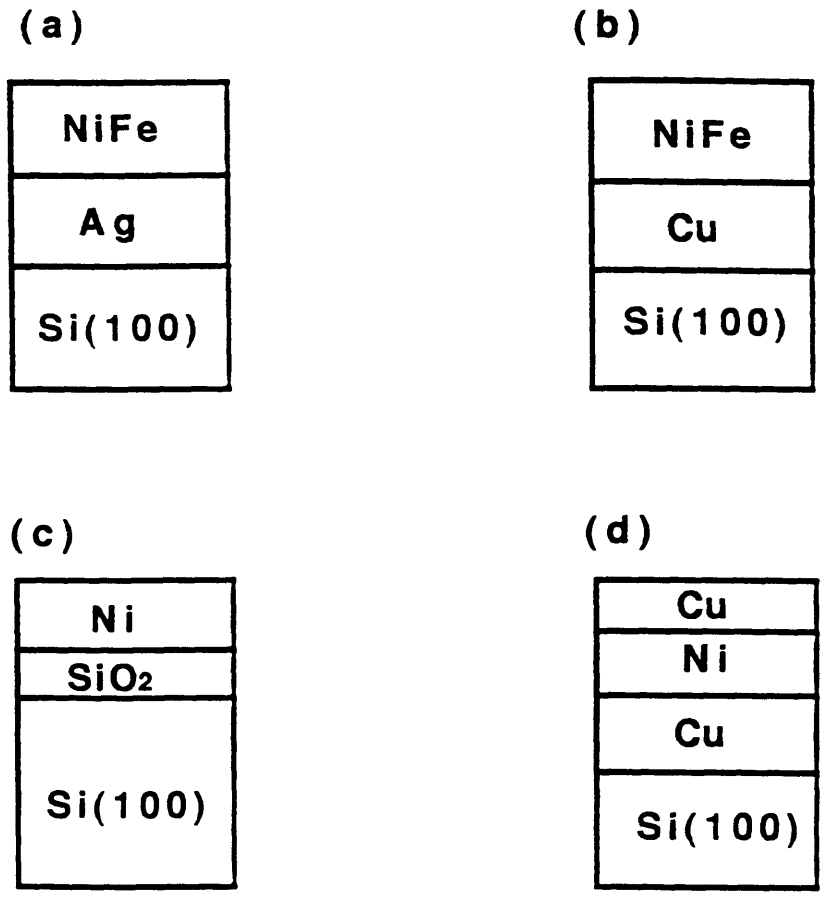

Fig.3.2.1. Samples for the experiment

a) polycrystalline permalloy/2000Å silver/Si(100)

b) polycrystalline permalloy/2000Å copper/Si(100)

c) polycrystalline nickel/natural silicon oxide(SiO_2)/Si(100)

d) Cu capping/ single crystalline Ni/ 2000Å Cu(100)/ Si(100)

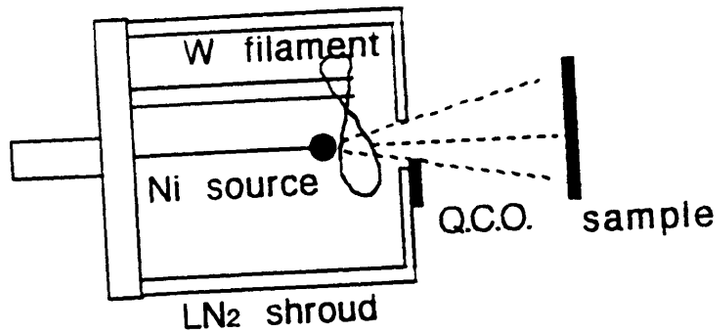

Fig.3.2.2. Schematic diagram of e-beam evaporator

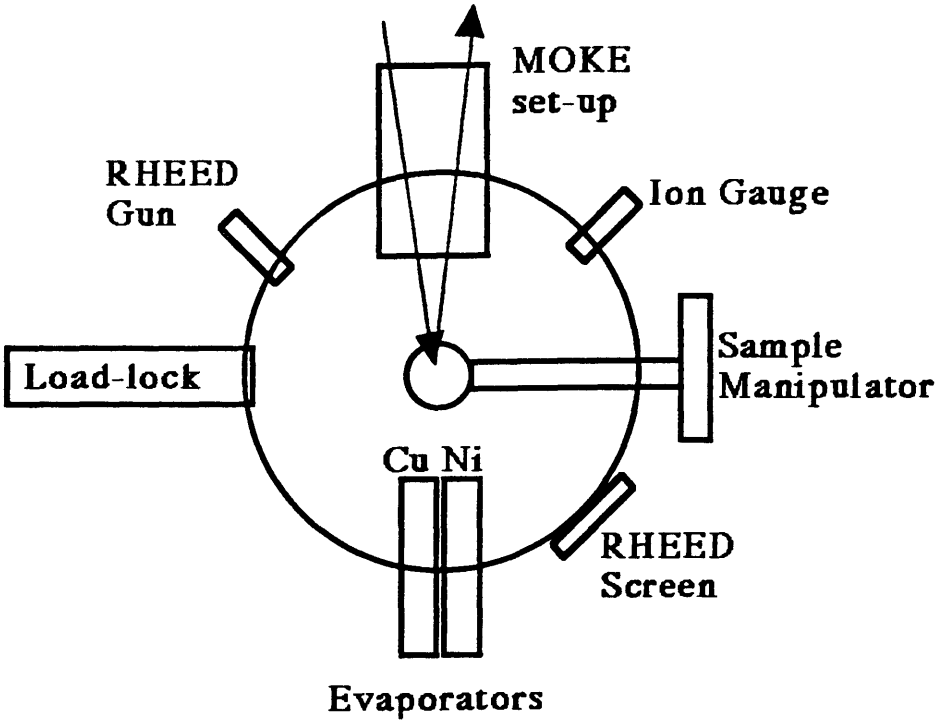

Fig.3.2.3. Schematic diagram of MBE chamber

3.3. MOKE measurements

The magneto-optic Kerr effect (MOKE) can be applied to a variety of materials to research surface magnetostriction or dominant magnetic anisotropies, to identify magnetic ordering, to correlate Curie-temperature trends with film thickness and to characterize the critical magnetization exponent at the 2-D phase transformation (Bader ,1991). Great progress has been made in using MOKE to address key issues in surface magnetism and in magneto-optics in ultra thin films (Bauer, 1990). Visible light is reflected from a surface layer comparable to the classical skin depth, $\delta_{cl} = 200\text{Å}$. In magnetic films of thickness $t << \delta_{cl}$, the light also reflects partially from the substrate. If the substrate is a non-magnetic material, all Kerr rotation is due to magnetic film. MOKE has been shown to be sensitive to a few monolayers (ML) in thickness.

Fig.(3.3.1) shows schematic representation of the magnetic interaction. We assumed that the saturation Kerr rotation corresponds to the saturation magnretization with film thickness is known and that the relationship is linear. The incident light is linearly polarized and the light is reflected from the magnetized film having Kerr rotation and ellipticity. The part of the induced response that is in-phase with the incident light gives rise to the rotation, while the out-of-phase part accounts for ellipticity. If an external magnetic field is applied to reverse the magnetization direction of the sample, the magneto-optic rotation and ellipticity reverse sign. Macroscopically the effect can be described by off-diagonal terms in the dielectric tensor Ξ,

$$\Xi = N^2 \begin{bmatrix} 1 & iQ & 0 \\ -iQ & 1 & 0 \\ 0 & 0 & 1 \end{bmatrix} \qquad (3.3.1)$$

where N is the refractive index and Q is the magneto-optic (Voigt) constant of the medium.

When light enters a magnetic medium, it separates into left-circularly polarized light (lcp) and right circularly polarized light (rcp). The interaction of light with a magnetic medium can be understood by the analyzing effects on its lcp and rcp. The amount that rcp and lcp are absorbed by the material can be found from the tensor. The absorptive properties depend upon the real part of the diagonal elements and the imaginary part of the off-diagonal elements. If this difference is finite then the two are absorbed differently. This means the two circular modes travel with different velocities and attenuate differently, due to the differences in the real and imaginary parts of the potential inside the medium. As

the rcp and lcp recombine when they leave the material, this difference in absorption leads to a change in polarization. For a linear polarized light, the axis of polarization is rotated and it has become elliptically polarized. These effects scale directly with the magnetization of surface (Bader,1990).

There are three Kerr configurations that are of importance: polar, longitudinal and transverse. In the polar Kerr effect the magnetization direction is perpendicular to the plane of the film (along the surface normal). In the longitudinal Kerr effect the magnetization is in the film plane and in the scattering plane of the light (plane of incidence). We use these polar and longitudinal configurations. In the transverse Kerr effect the magnetization is also in film plane, but the polarization direction of light is perpendicular to the plane of the film plane.

Typically the system consists of a laser source, a polarizing analyzer, and a photodiode detector. For MOKE magnetic characterization, the sample is maneuvered into the gap of electromagnets inside the vacuum chamber. The magnet yoke and pole pieces are made of soft iron. The magnet is capable of applying in-plane fields up to ±350 Oe, and out-of-plane ±200 Oe.

The optics used for detecting MOKE are shown in Fig.(3.3.2). Polarized light from 30mW He-Ne laser is passed through a polarizer. The laser and polarizer are configured to produce s-polarized light of light whose electric field vector oscillates perpendicular to the plane of incidence. The plane of incidence is defined by the propagation vector of the light and the normal to the sample's surface. The light enters the vacuum chamber through a window and is reflected by the sample. The reflected beam travels at through another windows. Finally, the light passes through another polarizer and into a photodetector. The polarization in the path of the reflected beam path is set slightly off extinction with respect to the initial polarizer. The amount of light which is able to path through the analyzing polarizer is proportional to the amount of rotation due to MOKE and is referred to as the Kerr intensity. The resulting m-H loop will be an average response over the area of the sample illuminated by laser beam (around $1mm^2$). Magnetic hysteresis curves are obtained by monitoring light intensity at the detector as the field is swept.(Ballentein,1989)

The first step in taking data was to align the optics so the laser beam passed through the center of the two polarizers and quarter wave plate and struck the magnetic film and photodiode in the center as shown in Fig.(3.3.2).

Once this had been accomplished, the second polarizer and quarter wave plate were rotated to minimize the signal to the photodiode. The second polarizer was than rotated one degree from its extinction orientation. The zero offset was adjusted so that the base signal

was zero, allowing us to look at the variation in the intensity. The absolute intensity which was amplified by a lock-in was recorded by the computer (IBM 386PC).

Before the optics had been adjusted, the maximum current to the electromagnet was set by adjusting the potentiometer attached to the current power supply. For each group of runs and its calibration file, the starting maximum current was kept the same.

The applied field was swept from its maximum to minimum value by the computer preset number of times (typically ten to twenty) and the intensity at the detector was plotted vs. field (512 bin numbers). The computer program used to take data was the E. G. & G. ACE Multichannel Scaling Software working with a MCS data acquisition computer board.

Initially a run of data was taken with the field applied along the axis orthogonal to the strain, the x-axis, and the starting magnet current set to its maximum value. The sample saturated readily in this direction for permalloys, while the Ni film saturated partially. Then data was taken with the field applied perpendicular to the plan of the film (z-axis) to check the in-plane easy axis.

From these data, we normalized all the data points to get m-H loops. Here m means a magnetization vector which was normalized by saturation magnetization (M_S). ($m = M/M_S$ = arbitary unit signal/maximum signal value).

We averaged the values of upper and lower parts of the hysteresis loop at each H under a given strain (the bold curve in Fig.(2.2.1)). The area surrounded by the averaged m-H curve and upper boundary in the first quadrant and positive m-axis is measured. This area is the effective anisotropy energy, and is shown as the shaded areas in Fig.(2.2.1).

Finally, the compressive strain was applied to see the change of the loops. Following the compressive strain, tensile strain was also applied to the films to see the rotation of the loops to opposite direction with the same data aquisition process.

Eventually, we had two area at the different strain state, then we could calculate the magnetoelastic coupling coefficients (B) and magnetostriciton coefficients (λ) from the Eq.(2.3.13) in section 2.3.

As a practical problem, T. Katayama (1988) reported the polar Kerr rotation angle of Fe layer would be very small below 56Å with red laser light. This means MOKE analysis depends on even laser wavelength and film thickness.

It is of interest to use a complementary technique with different probing depth to understand the surface itself or coupled magnetic layers.

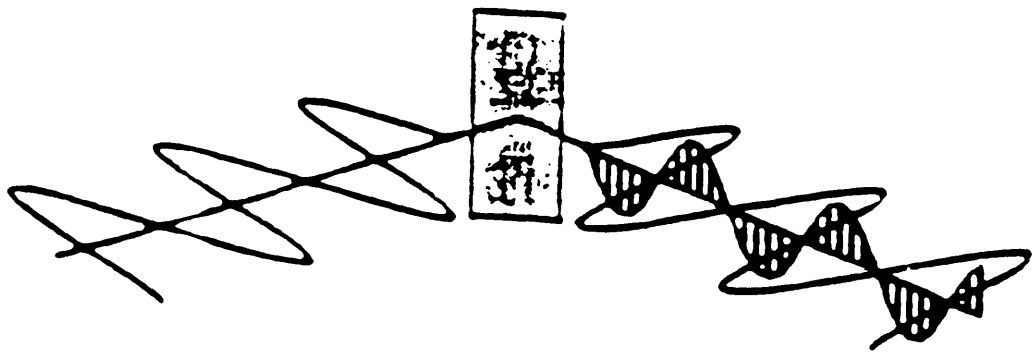

Fig.3.3.1. Schematic representation of the magneto-optic Kerr interaction. The incident light is linearly polarized and the light reflected from the magnetized film has a Kerr rotation and ellipticity (After Bader,1987).

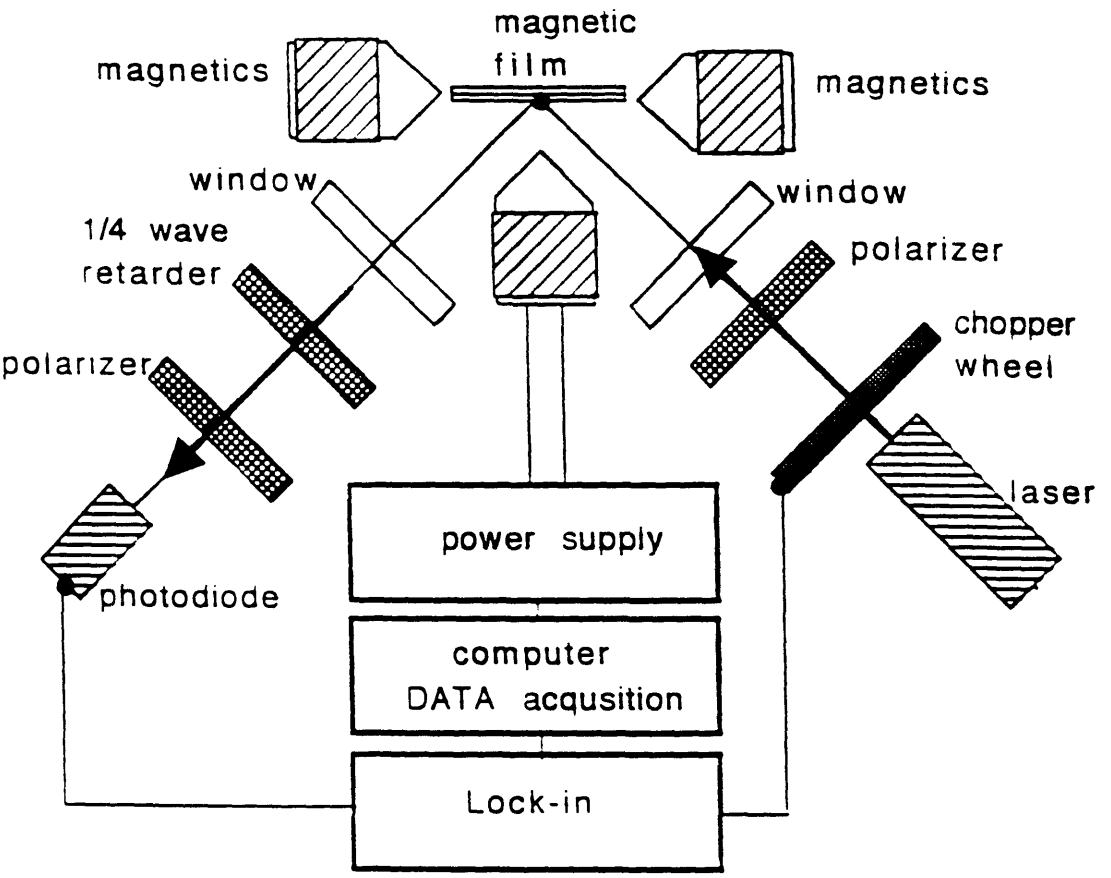

Fig.3.3.2. Illustraion of MOKE measurement setup

3.4. Auger Spectroscopy

In this study, Auger electron spectroscopy is used to check the composition of polycrystalline permalloy (NiFe) and Ni films. Particular attention was paid to the possible existence of silicide and oxide at the interface and surface.

A sputter etching gun produced a 2kV beam of Ar ions which is directed to the substrate. Sputtering is performed until the sustrate is clean. Typical contaminants on the magnetic film layer were oxygen and carbon. Auger spectroscopy study showed that NiFe films have no significant compositional variation with respect to depth. Moreover, Auger measurements reveals that the copper intermediate layer interacts more with the permalloy film than does the silver layer.

Auger electron spectroscopy is based on a radiationless process called the Auger effect. In the Auger process, a core level of surface atom is ionized by an impinging beam of electrons. The excited atom can decay to a lower energy state by having one of the outer electrons drop down into the vacant core level. Depending on the incident beam energy, the energy which is produced by such a valence-core level transition can be released as radiation, or alternatively, by the Auger process without emission of radiation. In the latter case, the excess energy from the transition is given to an outer electron of the same atom. This electron is then rejected from the atom with a characteristic kinetic energy as shown in Fig.(3.4.1).

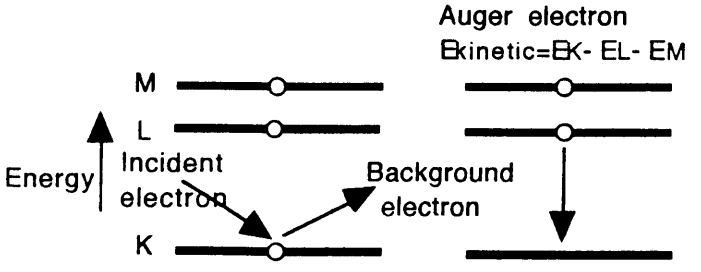

Fig.3.4.1. Illustration of Auger process.

Atoms can have many different Auger transitions. Each transition involving different energy levels results in a different kinetic energy for the Auger electrons. Usually certain transitions tend to dominate for a particular element. By analyzing the different kinetic energies of the Auger electrons, it is possible to determine the binding energies of a sample's surface atoms. Since these binding energies are the characteristic of a particular element, it is therefore possible to determine chemical composition. (L.C. Fieldman and J.W. Mayer,1986).

The variation in the number of secondary electrons per unit energy, dN(E)/d(E), is calculated and plotted versus kinetic energy. This derivative technique is used to minimize background effects and sharpen the peaks. Once the peaks are determined, it is possible by reference to standard data taken to determine the composition at the surface (Davis *et al*, 1978)(Walat, 1993).

Due to the small inelastic mean free path of the electrons, only Auger electrons from atoms within the first few layers will be ejected from the surface without any significant loss of energy. Such electrons will give peaks in the energy distribution of the secondary electrons. The energy and shape of these Auger peaks can be used to determine the composition of the surface.

3.5. Four-point Bending and other techniques to measure B.

How does one determine the magnetostrictive properties of materials? Large λ's (10^{-4} to 10^{-3}) or B's can be measured by X-ray diffraction (XRD). λ in transition metals and alloys (10^{-7} to 10^{-4}) can be measured with strain gauges. Since XRD or strain guages are not suitable for thin films, other techniques have been developed to measure the magnetielastic coupling coefficients.

The direct method to determine the magnetostriction constant of a thin film is to utilize the static bending of a thin film-substrate by the magnetostriction effect under the influence of a magnetic field. The measurement of a small degree of bending is delicate and requires very thin substrates of rather large size. Typically two methods of measuring the magnetostriction coefficients through the direct method are reported in the literature which yield reliable data. One may use optical interferometry to detect the bending of the magnetic film under the influence of a magnetic field. Hoffman et al (1969) reported ultrathin foils as substrate which shows bending observable by optical interferometry. Bellesis (1993) and Harllee (1993) also showed magnetostriction measurements by interferometry.

The other uses an electrical capacitance probe with a cantilevered substrate. A variation of this method was used with some success (Klockholm, 1976); the magnetostrictive stress in a magnetized film causes a deflection in the film-substrate cantilever. The thickness and elastic constants of both film and substrate are required to extract the magnetostriction. The deflection of the free end is measured by a capacitance probe (J. E. Goldman, 1949)(C. Y. Shih,1988).

It is possible, also, to determine the change in magnetization in response to an imposed stress or strain. Clark and Wun Fogle (1989) have used such a simple applied stress technique to measure bulk ME coefficients of amorphous ribbons. Sun and O'Handley (1990) have used the same principle to measure the surface ME coefficient of an amorphous material (assumed isotropic) using spin polarized secondary electron spectroscopy to selectively monitor the response of the surface magnetization to the applied strain.

In addition, Zuberek et al (1988) measured the surface magnetostriciton of Ni/Ag multilayer using strain-modulated ferromagnetic resonance (FMR) and found a strong thickness dependent contribution to the magnetoelastic coupling coefficients that drove B^{eff}

negative at small thickness. Several other techniques such as a dynamical magnetostriction tester (so called, DYMOST) (G.Trippel,1977), mechanical bending of cantilevered substrate (Kwaaitaal 1982), special 4-point bending holder for VSM (D. Mauri, 1990), and ferromagnetic resonance with tapered sample for uniform strain (R.D. McMichael, 1994), have been reported.

We have used the simple streching method to measure the B^S of the polycrystalline Ni film deposited on a textured Cu strip and explored thin film growth on piezoelectric transducer (PZT) substrates as an alternative way of inducing strain to measure ME coefficients as shown in Fig.(3.5.1). However the streching method is hard to control and not practical in a UHV chamber. It is difficult to grow single crystal films on PZT substrates due to porosity of the PZT ceramics which degrade the optical signals and pin the magnetic response. Moreover, PZT as an actuator was not realistic because it requires tremendous amount of voltage to make the necessary bending of the silicon wafer substrate.

Finally, we would suggest a 4-point bending system actuated by mechanical force to produce strain to satisfy our requirements. The system is shown schematically in Fig.(3.5.2). (See the Appendix-A for the detail relationship between surface strain and bending). All of the materials on the holder are nonmagnetic; therefore it does not interfere with the magnetic measurements.

We can get homogeneous uniaxial strain between 2 inner poles by using 4-point bending as shown in Fig.(3.5.2). We can apply the bending distance (Y_a) and surface strain (e) as Eq.(A.5) in Appendix (A. Sloane, 1952). The apparatus consists of 2 metal blocks with 8 rods (1/16" of diameter) spaced at a specific distance from the center of the block (L=3cm, a=1cm). Fig.(3.5.2).(a) and (b) shows that uniaxial tensile or compression stresses can be applied to the substrates and films by placing it in contact with the 2 sets of rods while a center block is driven by an mechanical actuator (micrometer or fine thread mechanism for the UHV).

Our method of checking the change in magnetization with respect to strain produced by four-point bending is proved to be sensitive and reliable up to 10^{-7} of magnetostriciton as will be shown in our experimental results, especially NiFe films.

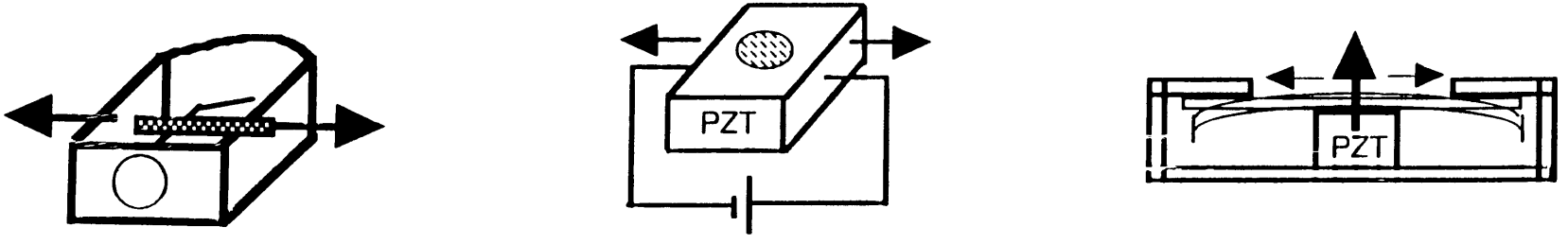

(a) (b) (c)

Fig.3.5.1.. Schematic diagram of PZT 4-point bending specimen holder.
(a) simple streching (b) PZT as a substrate (c)PZT as an actuator

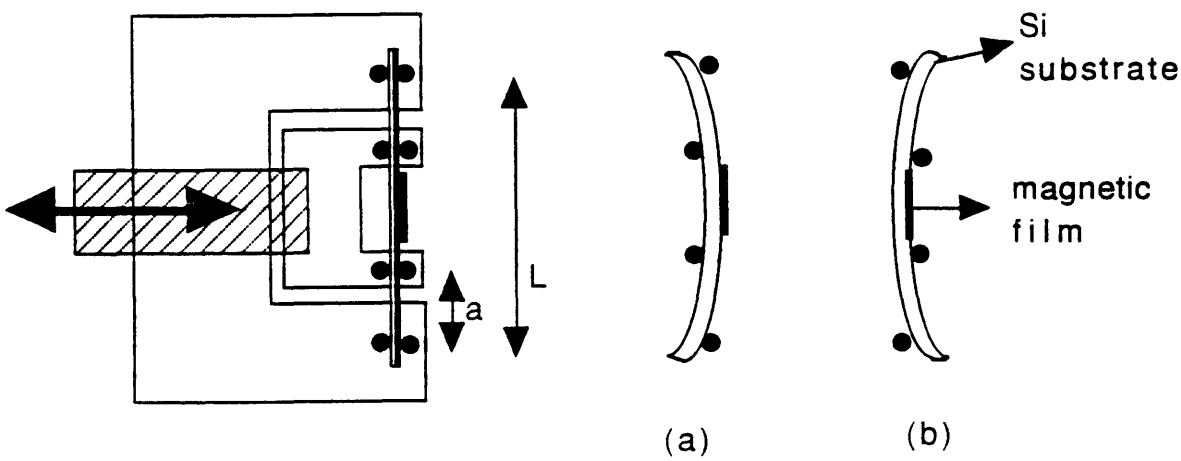

Fig.3.5.2. Four-point sample holder. L=3 cm, a=1 cm.
(a) tensile strain (b) compressive strain

4. Experimental results

4.1. Permalloy on silver

Fig.(4.1.1) shows the $B^{eff}(t)$ data vs. film thickness for polycrystalline $Ni_{79}Fe_{21}$/ 2000Å Ag/ Si(100), a slightly iron rich permalloy. The data were taken *in-situ* MOKE as we described earlier. For film thicknesses greater than 40Å, the measured value was identical to the bulk value $B^{eff}= -0.8x10^5$ J/m^3 ($\lambda= +0.25x10^{-6}$). This is a very small magnetostriction but is quite reliably measured by our method even in films less than 100Å thick. As the film thickness decreases a strong positive ME term becomes evident in the measured effective ME coupling coefficient:

$$B^{eff}(t) = B^{bulk} + B^{surface}/t \qquad (4.1.1)$$

where $B^{surface}= +1.4x10^{-4}$ J/m^2 for polycrystalline $Ni_{79}Fe_{21}$. Eq(4.1.1) is identical to that observed for surface anisotropy energy in many thin films and multilayer systems and is fully consistent with the Néel model described in section 2.5.

The solid line in Fig (4.1.1) is a fit to the Néel model, that is :

$$B^{eff}(t) = -0.78 + 14/(t-7) \quad (x\ 10^5\ J/m^3),$$

where t is in units of Å. Here the 7Å thickness offset suggests a magnetically different layer. Possible origin for this offset, diffusion induced intermixing or the exchange coupling between surface and bulk, will be explained later. The arrow indicates the bulk value of the magnetoelastic coupling coefficient. B^{eff} shows a change of sign around a thickness of 20Å.

The results in Fig (4.1.1) indicate that near the film surface the magnetoelastic coupling coefficient can be much greater than its value in the interior and can even have a different sign. We can see this result more clearly if we plot $B^{eff}\bullet(t-7)$ vs. film thickness (t-7) as shown in Fig.(4.1.2). The slope is B^{bulk} and the intercept is $B^{surface}$.

The effect of Eq.(4.1.1) may be simply related to the lower symmetry of the surface Néel model or it may arise from some sructural or chemical anomaly unique to the surface or to the ultrathin films. At the most basic level, the data in Figs.(4.1.1) and (4.1.2)

indicate that in ultrathin films, i.e. near the surface, the magnetization orientation is much more sensitive to the state of strain than in the thicker films. There could be many phenomena that contribute to this enhanced magnetoelastic coupling.

We need to determine whether any chemical or structural changes in the thinnest films could be responsible for the abrupt change of the magnetoelastic coupling near the surface. Microstructural effects will be discussed in section 4.5 with TEM and Auger depth profiling. Here, we consider the chemical composition effect. Auger depth profiling of the permalloy film composition shows that the Ni/Fe ratio to be uniform within ±4% throughout the film thickness as shown in Fig (4.1.3). This figure is a plot of the atomic concentration of nickel and iron elements with respect to sputter time. Fig.(4.3.1) shows the relative ratio of Ni and Fe according to sputter time because only Ni and Fe Auger signals are normalized. The thickness of the polycrystalline permalloy film was nominally 30Å. The change in composition in the first 30 sec is due to surface oxidation during the transportation of the sample after *in-situ* magnetic measurements. The peaks after 3 min. of sputter time are artifact from the software and are not physically important. Sputtering was done with a gun voltage of 2 kV-5 $\mu A/cm^2$, scale factor of 0.063 k c/s and sputter rate of 10Å/min .

For the surface to show a ME coefficient of the order $+10^6$ J/m^3 ($\lambda = -5x10^{-5}$), the composition would have to shift approximately from $Ni_{79}Fe_{21}$ to $Ni_{85}Fe_{15}$ as shown in Fig (4.1.4) (data taken from O'Handley, 1977). Thus this change is not a result of the composition change near the surface but probably is due to the surface effect which is modeled by Néel.

To verify the result of Fig.(4.1.1), we measured B again with *ex-situ* VSM. We used the same composition of the films ($Ni_{79}Fe_{21}$) with various thicknesses of polycrystalline permalloy films on a silver/silicon wafer substrate as shown in Fig.(3.1.3).(a) using a mask with e-beam evaporation. The result in Fig.(4.1.5) shows that one could see the same behavior as in Fig.(4.1.1). We can fit the measured effective ME coupling coefficient with the Néel form:

$$B^{eff}(t) = -1.17 + 28.6/t \quad (x\ 10^5\ J/m^3).$$

The unit of t is Å. Since all thicknesses of the magnetic films are recalibrated by the VSM saturation magnetization data, the above equation does not have a magnetically different

layer thickness t_0. We can see the change of sign around a thickness of 25 Å and a reasonable bulk value as indicated by the arrow in Fig.(4.1.5). The reason that we observe smaller values than *in-situ* near the surface may be due to surface pinning because of surface oxidation.

In conclusion, we see a giant magnetostriction coefficient near the surface which has 1/t dependence through *in-situ* MOKE and *ex-situ* VSM measurements. This behavior is consistent with the model that Néel expected. Moreover, this behavior is not a result of composition change in the thinnest films.

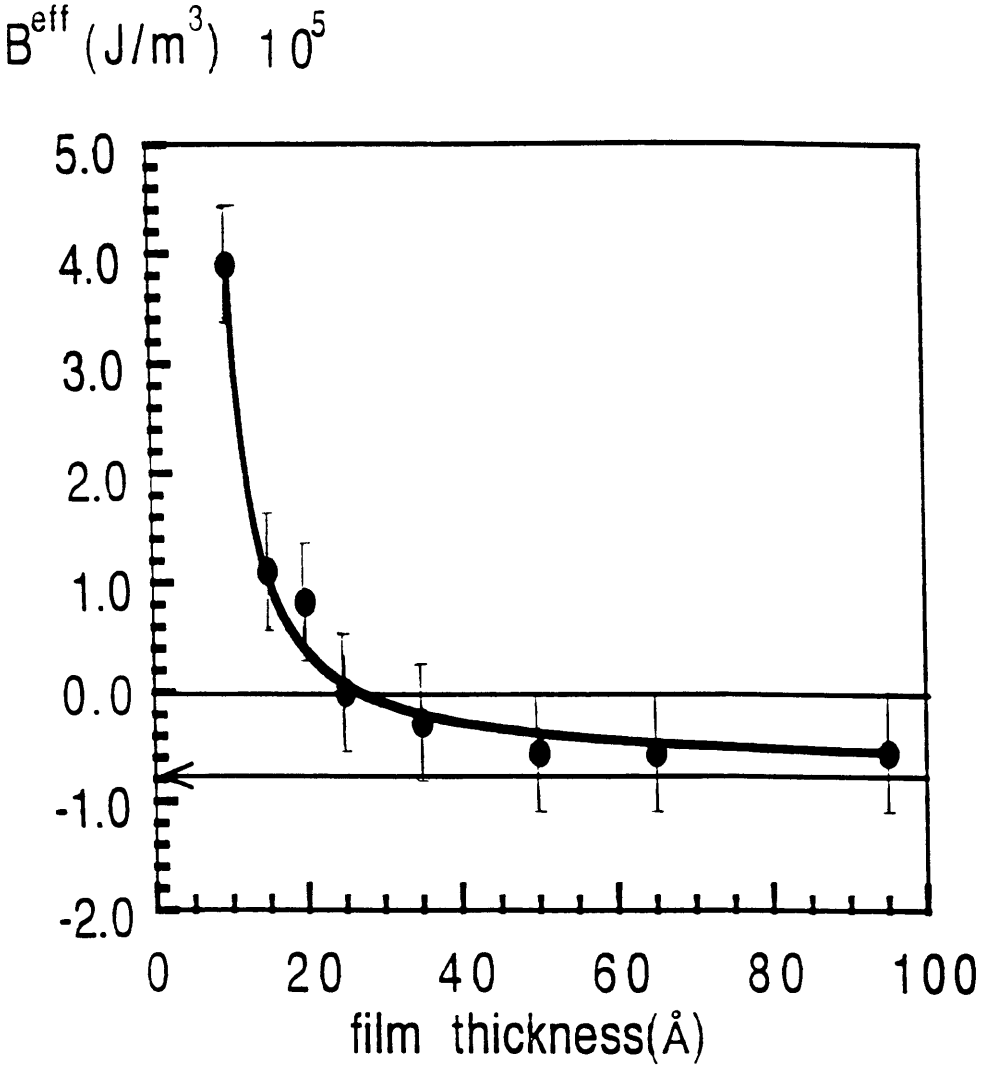

Fig.4.1.1. Plot of magnetoelastic coupling coefficient for polycrystalline permalloy/Ag/Si vs. film thickness. Measurements are done *in-situ* .

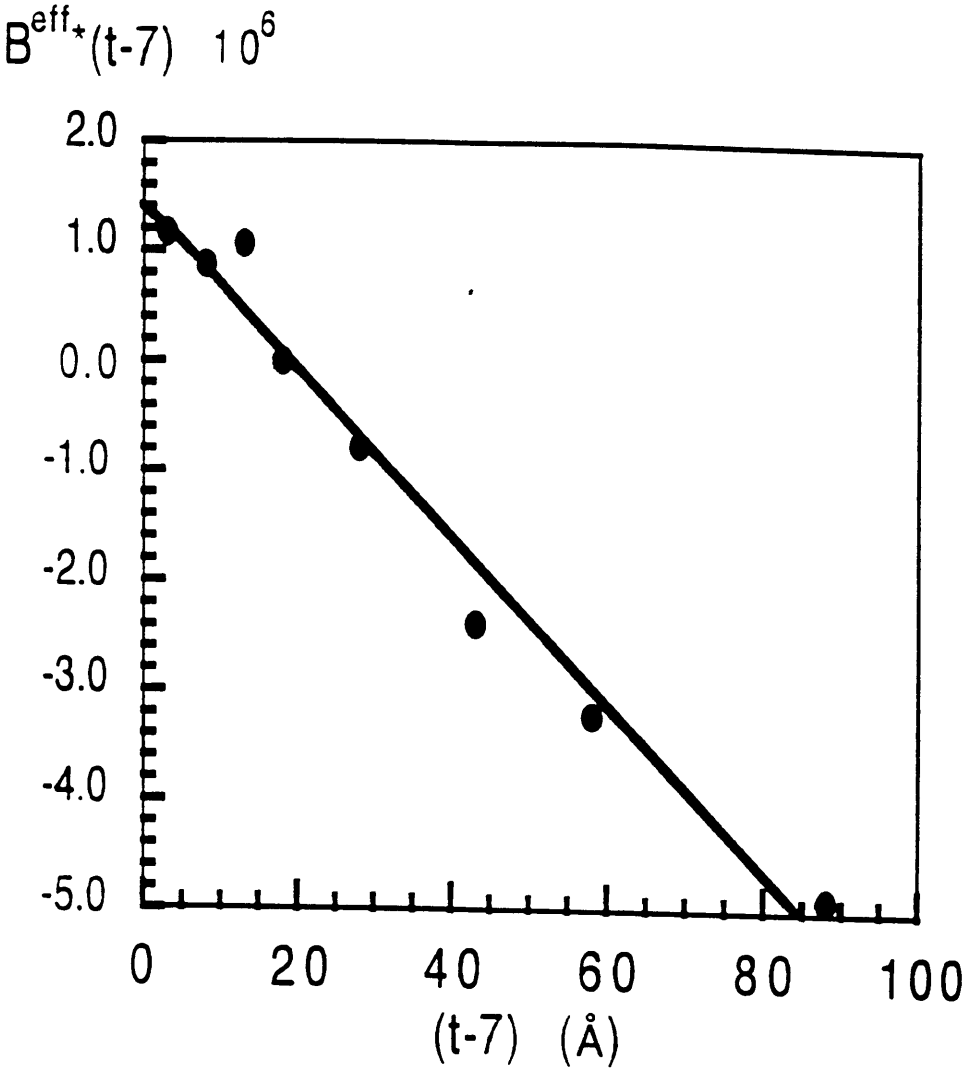

Fig.4.1.2. Plot of B^{eff}•t vs. film thickness (t)

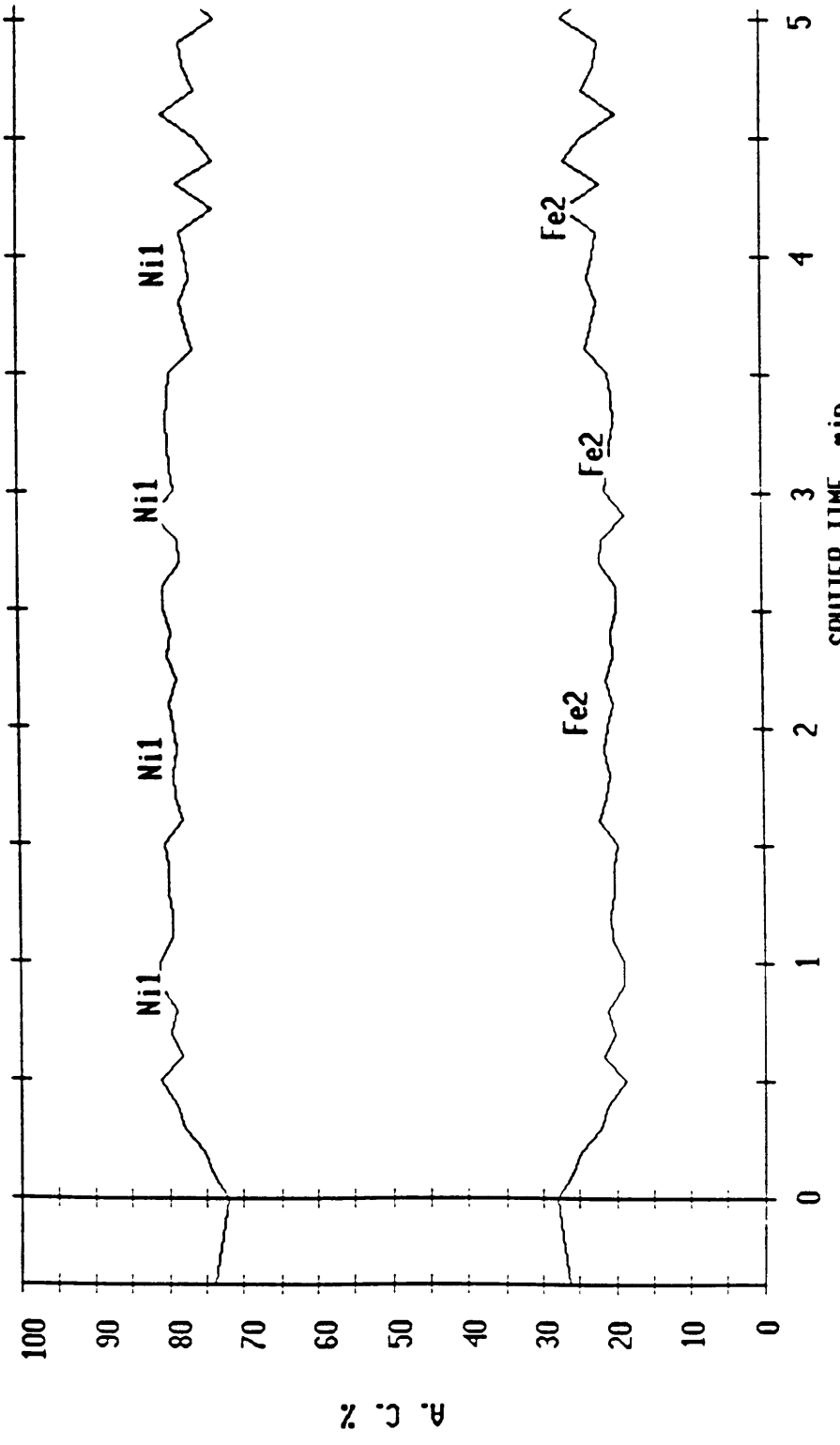

Fig. 4.1.3. Auger depth profiling of the permalloy film on silver vs. sputtering time

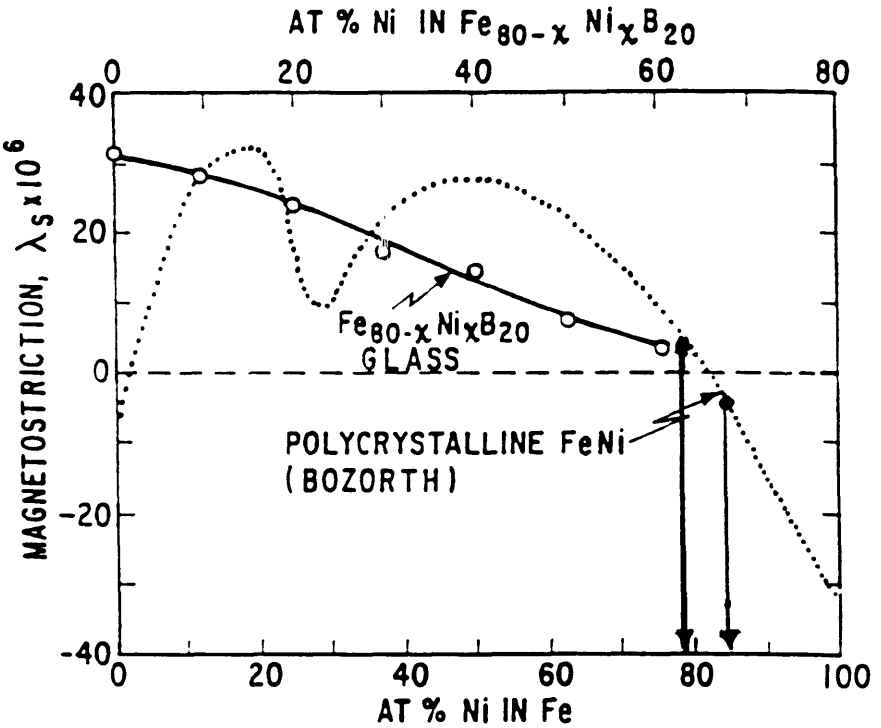

Fig.4.1.4. Magnetostriction of polycrystalline Ni-Fe alloy.(After O'Handley, 1977).

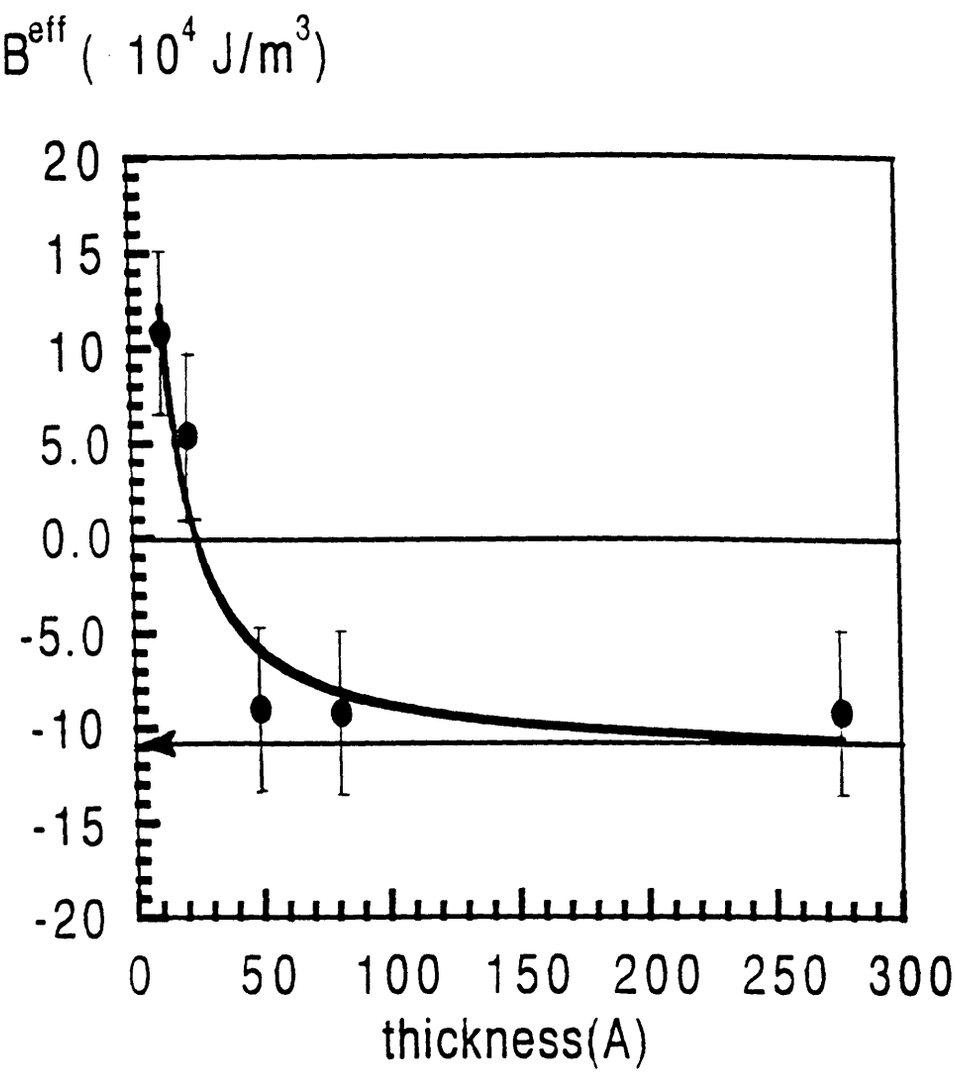

Fig.4.1.5. Plot of $B^{eff}(t)$ vs. t measured *ex-situ* by VSM .

4.2. Permalloy on copper

Similar measurements for $Ni_{79}Fe_{21}$/2000Å Cu/ Si(100) also reveal a divergence toward positive values of B^{eff} at small thickness as shown in Fig.(4.2.1).(a). The result shows almost the same bulk value as in the previous case. We can express the behavior of the effective magnetoelastic coupling coefficient , $B^{eff}(t)$, as,

$$B^{eff}(t) = B^{bulk} + B^{surface}/(t\text{-}13Å) = -0.76 + 35/(t\text{-}13) \quad (x10^5\ J/m^3).$$

All parameters used to fit the data have the same order of magnitude as the previous case. Here 13Å is the magnetically different layer to fit the data.
The above result is expressed more clearly if we plot $B^{eff}\bullet(t\text{-}13)$ vs. film thickness (t-13) as shown in Fig.(4.2.1).(b). The slope is B^{bulk} and the intercept is $B^{surface}$.

We have observed that the surface magnetoelastic coupling term is shifted more on the thickness scale than in the case for permalloy/Ag/Si. We could verify that the shift is due to chemical mixing at the magnetic film/ substrate interface through Auger depth profiling as shown in section 4.5. We observe that permalloy/Cu shows a more diffuse interface than does the permalloy/Ag.

On the other hand, in Fig.(4.2.2), the Auger depth profiling result shows there is no significant compositional variation with respect to depth before the intermixing. The thickness of polycrystalline NiFe/Cu film for the Auger depth profiling is nominally 30Å and sputter rate was 10Å/min. Though we can observe that the interface has more Ni and less Fe at the 3min. of sputtering, a location of the nominal interface, there is no significant composition change for our thinnest films. The peak perturbation around 3 min. of sputter time where close to the norminal interface in Fig.(4.2.2) is mainly due to the software artifact.

In conclusion, the result in Fig.(4.2.1) for NiFe/Cu supports the findings of a surface anomaly of effective magnetoelastic coupling coefficient in NiFe/Ag. However, there appears to be more intermixing for NiFe-Cu than NiFe-Ag interface. This is reasonable if we see the phase diagrams in Ni and Fe with Ag and Cu as shown in Fig.(4.2.3). Fig.(4.2.3) shows that, at room temperature, Cu has a very low solid solubility in Fe but has a very high solubility in Ni. However, Ag has very low solid solubility with either Ni

or Fe at room temperature. So, permalloy/Cu can have more diffuse interface due to greater Cu solubility in Ni or Fe than does the permalloy/Ag.

Therefore we can say that the behavior of B^{eff} for permalloy on copper can be expressed as a Néel model as we expected in section 2.5.

(a)

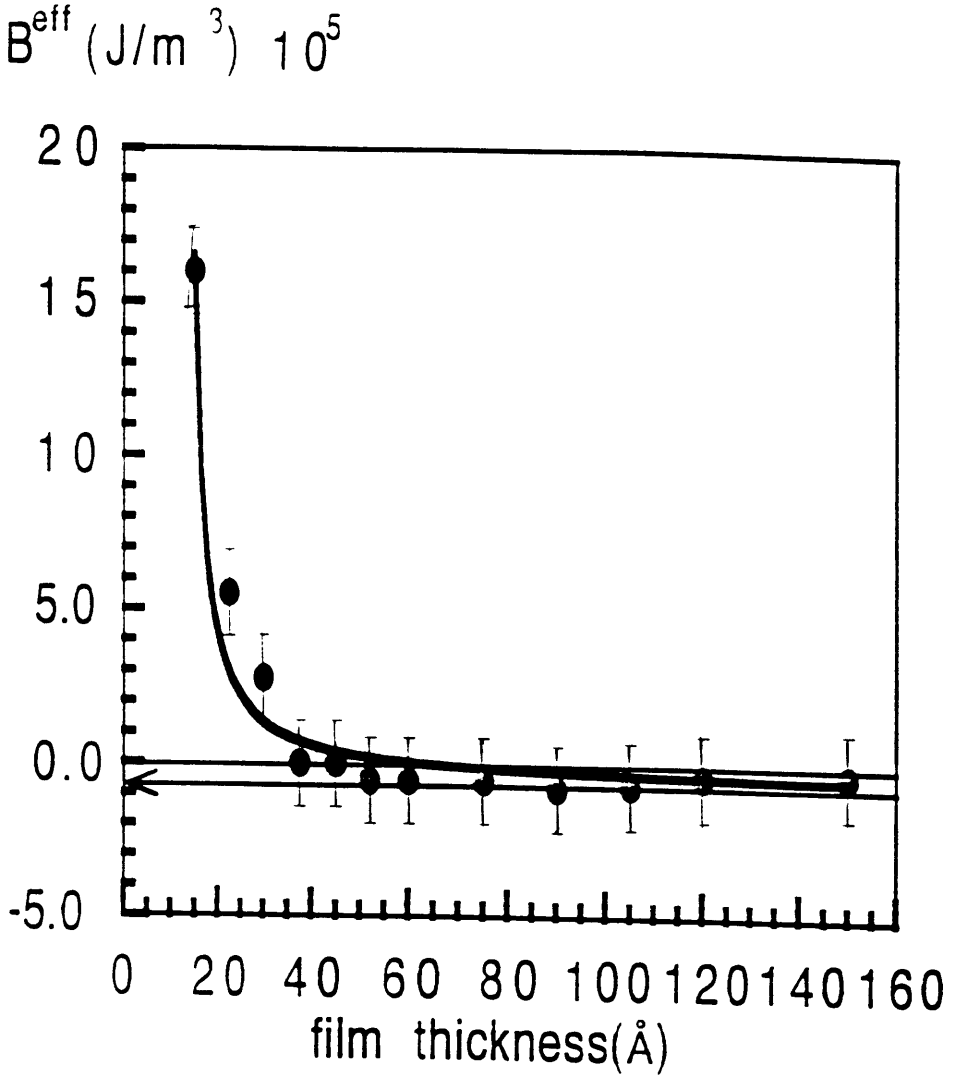

Fig.4.2.1. Magnetoelastic coupling coefficient for polycrystalline permalloy/Cu/Si vs. permalloy thickness. Measurements are done *in-situ* .

(a) Plot of B^{eff} vs. film thickness (t)

(b)

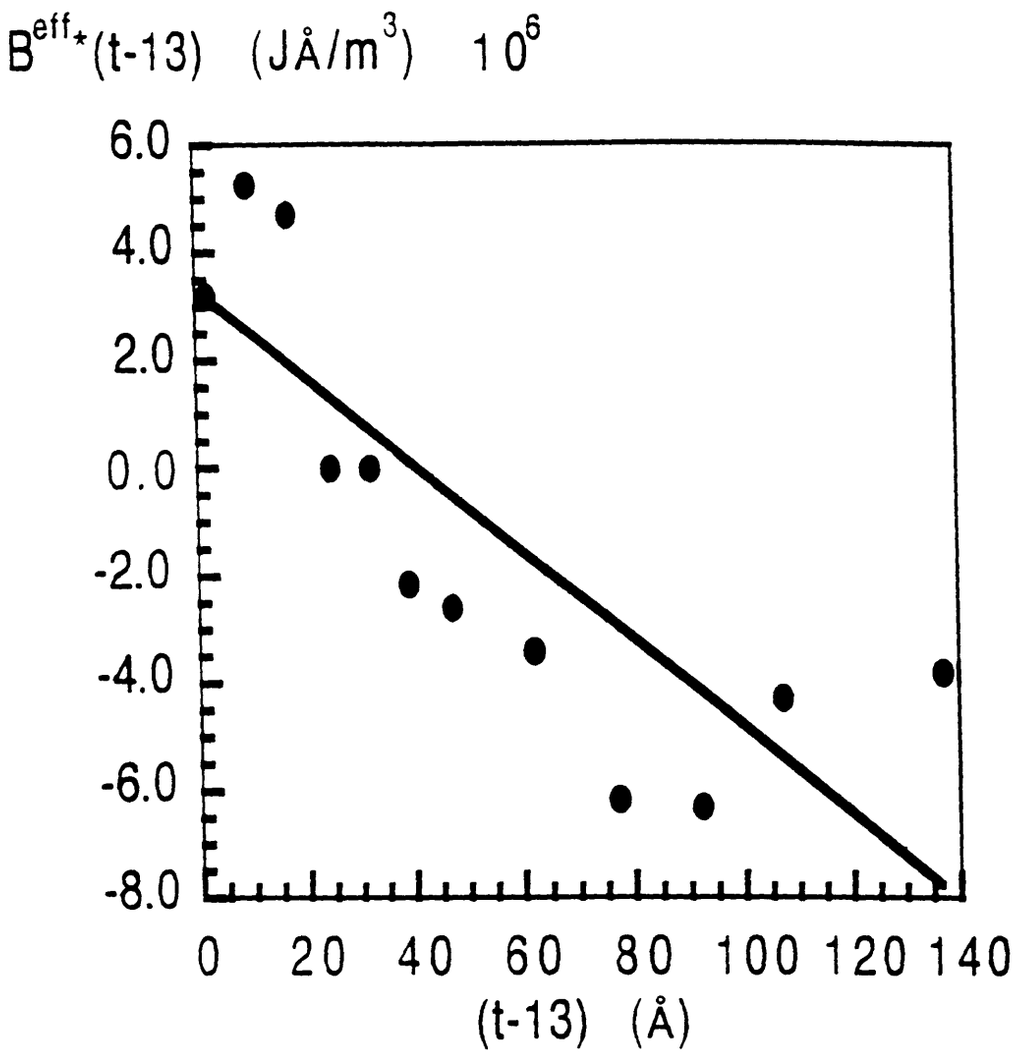

(b) Plot of $B^{eff}\cdot(t-13)$ vs. (t-13)

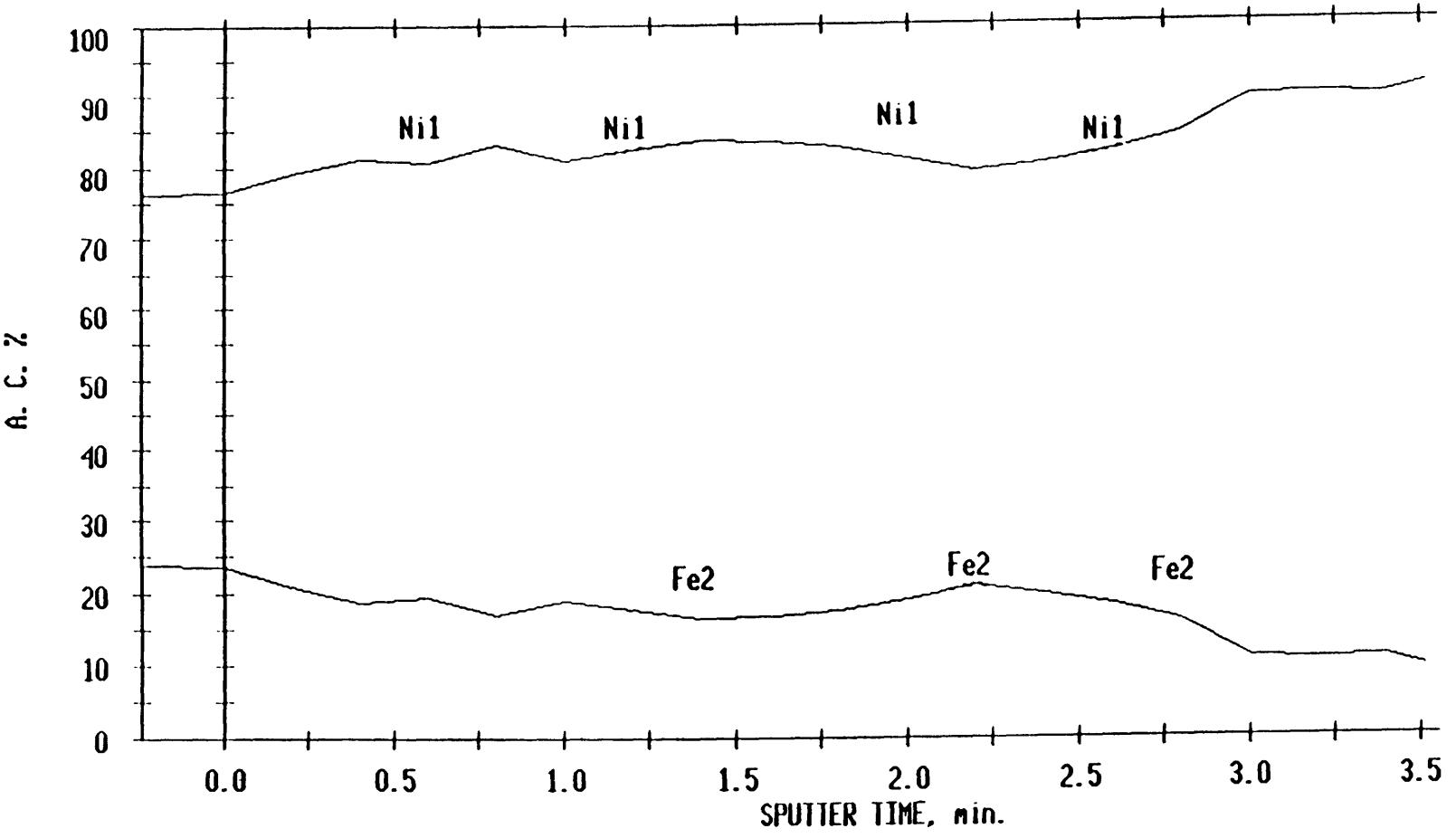

Fig.4.2.2. Plot of atomic content of Ni and Fe elements in NiFe vs. sputtering time (min).

(a)

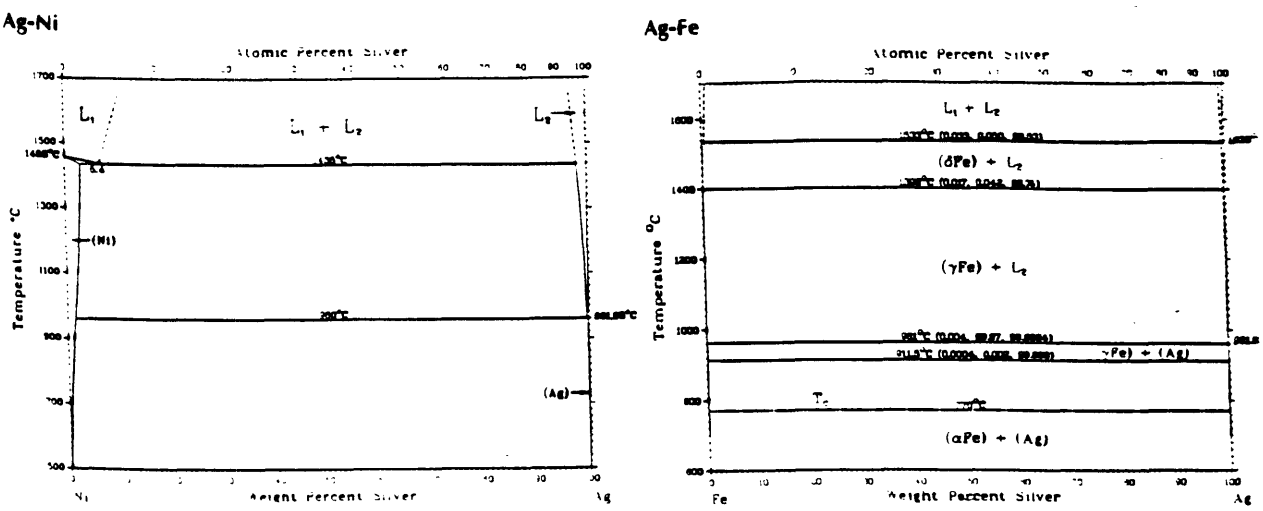

(b)

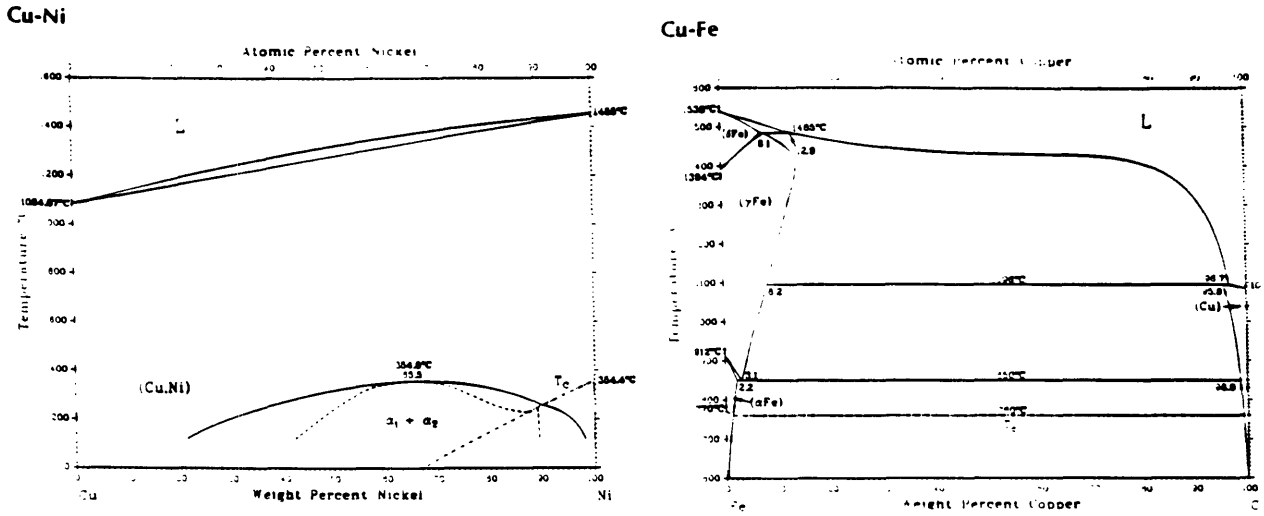

Fig.4.2.3. Binary phase diagrams of (a) Ag-Ni and Ag-Fe, (b) Cu-Ni and Cu-Fe (ASM Handbook , vol 3, Alloy Phase diagrams. ASM international, the Materials Information Society)

4.3. Polycrystalline Ni on Si.

We deposited Ni films on silicon wafers which have a natural oxide layer (5-40Å thick) at the surface. The result of in-situ MOKE measurements of the magnetoelastic coupling coefficient, B, in polycrystalline Ni is shown in Fig.(4.3.1).(a). Note that the vertical scale does not go to zero.

From the result in Fig(4.3.1).(a), we are able to fit the data with the Néel form:

$$B^{eff}(t) = B^{bulk} + B^{surface}/(t-t_o)$$
$$= 5.6 + 186/(t\text{-}55Å) \quad (x10^6\ J/m^3) \qquad (4.3.1).$$

$B^{eff}(t)$ can be very different from the bulk value and diverges at small thickness to values of the same positive sign as B^{bulk}.

Fig.(4.3.1).(b) shows a plot of B^{eff}•(t-55Å) vs. film thickness (t-55Å). The slope is B^{bulk} and the intercept is $B^{surface}$.

$B^{eff}(t)$ changes abruptly around 80Å, and some deviations from the form of Eq.(4.3.1) are observed around 100Å in Fig.(4.3.1).(a). The arrow indicates the reported bulk value, B = 6.2 x 10^6 J/m^3 which corresponds to a magnetostriciton of -34 x 10^{-6}. The vertical dashed line in Fig (4.3.1).(a) shows an offset as before, possibly related to silicide formation, NiSi solid soution or exchange coupling. TEM micrographs in section 4.5 verify the presence of silicides in these films. The error bars in the data correspond to a 5 % uncertainty.

The dip in B^{eff} observed near 100Å in the Ni/SiO_2/Si films may be a real effect. It is known that Si strongly drives the magnetostriction coefficient of Ni more positive (B^{eff} more negative) as shown in Fig.(4.3.2) from measurements by Batova (1976). It implies we may be observing a combination of both the effects of strong positive B due to surface magnetoelastic coupling and negative B due to the increased Si content near the interface. The nickel silicide (Ni_3Si) layer may be causing the departure toward more negative B^{eff} in the bulk region (near 100Å) before the stronger surface effect (B^{eff} more positive) takes over for thinner films.

If the anomaly in $B^{eff}(t)$ near 100Å is related to silicide formation, it has important technical consequences in terms of enhancing or passivating this giant surface magnetostriction effect. The data in Fig.(4.3.2) suggest that we may be able to enhance or

degrade the surface term (B^S) by coating or passivating the surface with appropriate materials.

In conclusion, the results for Ni/Si support the behavior of the magnetoelastic coupling near the surface as we observed in permalloy films and point to a possible new effect on $B^{eff}(t)$ due to alloying or chemical contamination of the film.

(a)

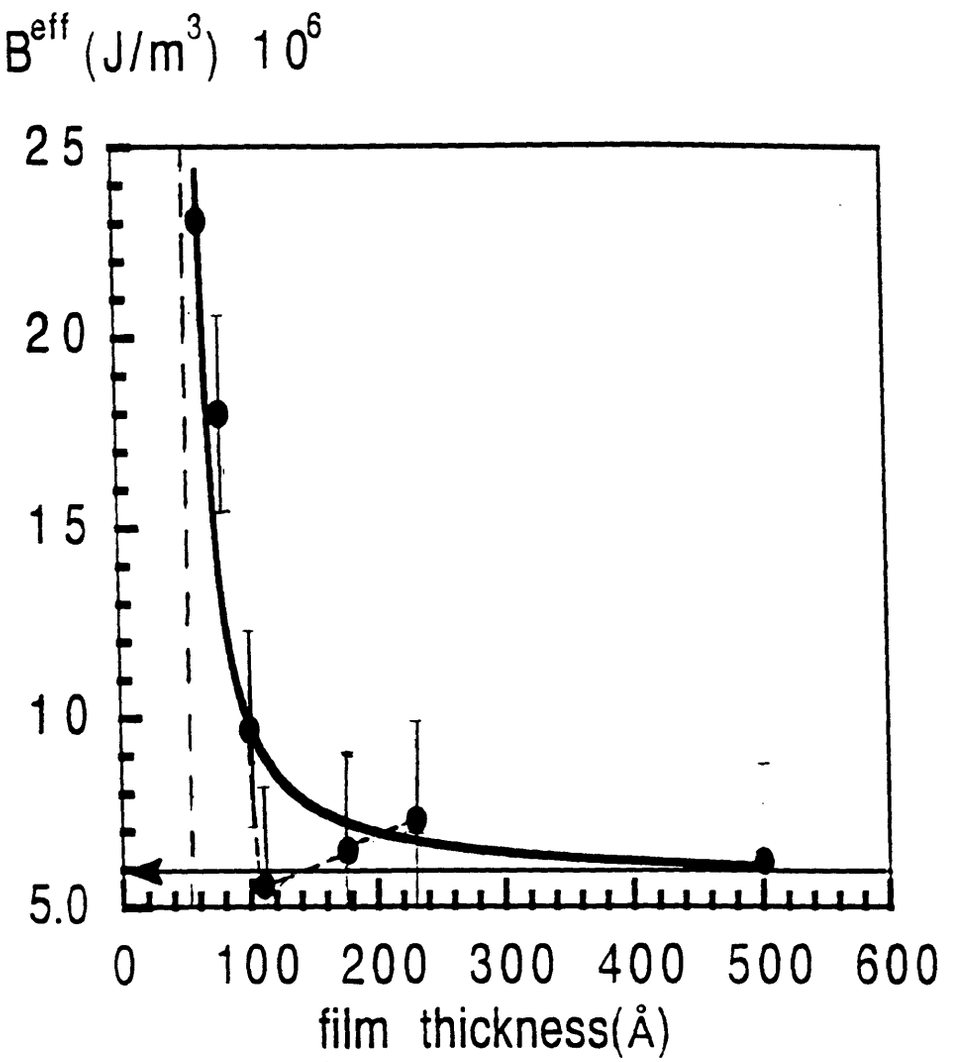

Fig.4.3.1. (a) Plot of $B^{eff}(t)$ for $Ni/SiO_2/Si$ with film thickness.
(b) Plot of $B^{eff} \cdot t$ vs. film thickness (t)

(b)

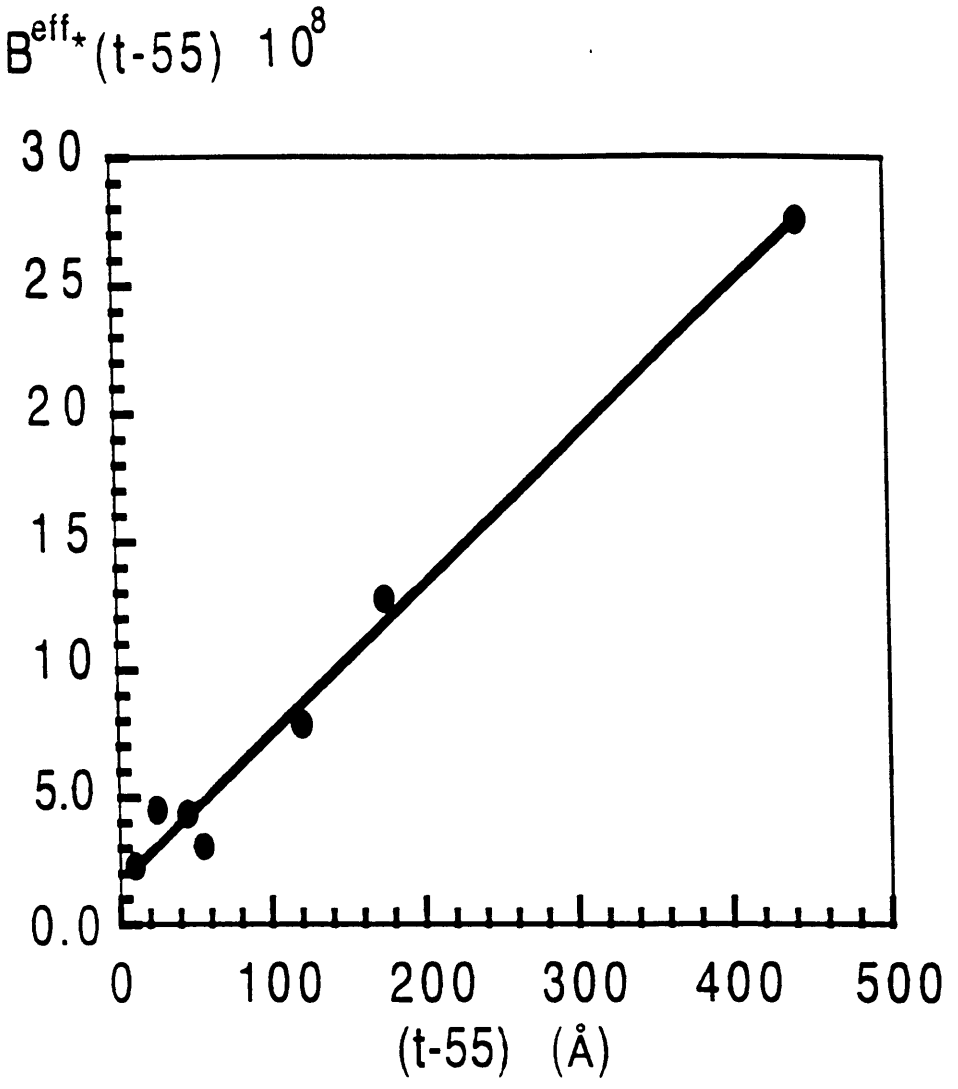

(b) Plot of B^{eff}•t vs. film thickness (t)

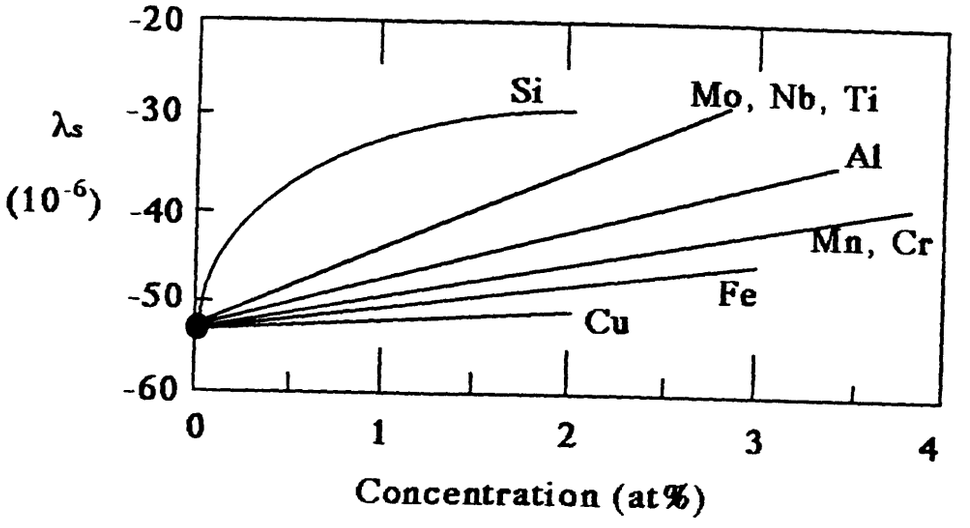

Fig.4.3.2. Variation of magnetostrciton coefficients in polycrystalline Ni with Si and other solvents. (After Batova)

4.4. Epitaxial Ni with Cu capping layer (Cu/Ni/Cu/Si)

So far, we have described our results on polycrystalline permalloy and Ni films. In these cases, we were able to establish the existence of a strong surface magnetoelastic effect by measuring the effects of applied strain on MOKE or VSM M-H loops. We now turn our attention to single crystal, epitaxial Ni films grown on Cu/Si(100) and capped with 40Å of Cu. Because of the larger anisotropy of these films and the small strain we were able to apply, we were unable to use the same method of measurement on these epitaxial films as was used on polycrystalline films. A new method of measuement is described.

We have studied epitaxial Ni films to get B_1^{eff} and B_2^{eff} instead of one B^{eff} as in the isotropic polycrystalline films. Several effects such as magnetoelastic anisotropy coming from misfit and other strain, Néel surface anisotropy and crystal anisotropy contribute strongly to the total magnetic anisotropy. Bochi et al (1993) have demonstrated how complex the problem is even in a relatively simple system such as epitaxial Ni/Cu(100). Fig.(4.4.1) illustrates the complex behavior that can result from the combination of these various energies. The Néel surface anisotropy energy (K_N: 1.0×10^5 J/m^2), magnetoelastic energy (2Be: 1.2×10^5 J/m^3) and shape anisotropy energy ($2\pi M_s^2$: 1.3×10^5 J/m^3) can compete with each other while only the shape anisotropy energy was dominant in the polycrystalline NiFe and Ni film cases. Due to the large anisotropy energies, we cannot determine the magnetoelastic coupling coefficients in a simple way as in the polycrystalline cases. We can apply at best an additional magnetoelastic anisotropy energy amounting to about 5% to a given reference anisotropy energy. This implies that we cannot observe any significant m-H loops change for the range of external strains we are able to apply.

To verify this expectation, we have made Ni films of various thickness on 2000Å thick Cu on Si substrates. The films were then capped with 20Å Cu giving a final structure: Cu/Ni/Cu/Si(100). The copper layer offers a good substrate on which to grow single crystal nickel layers and gives a misfit strain with Ni of 2.6%. The protective copper layer makes it possible to perform *ex-situ* VSM measurements to determine saturation magnetization and magnetoelstic coupling coefficients. A special holder for the VSM, shown in Fig.(3.1.3), gives uniform strain over the sample area during the measurements.

Fig (4.4.2) shows the m-H loops measured by VSM. Clearly, it is difficult to resolve much of a difference in the approach to saturation by this method. The problem is that the

anisotropy of epitaxial Ni is too large for ME anisotropy energy (B·e) with imposed strain to make a difference in the m-H loops.

Thus we make use of a method developed by Bochi (1994) to obtain an indirect but reasonable estimate of $B_1^{surface}$ and $B_2^{surface}$ for the epitaxial magnetic films by measuring the total effective magnetic anisotropy energy density as a function of film thickness. We apply this model to Cu/Ni/Cu(100) and Cu/Ni/Cu(111) sandwiches studied and repored by Jungblut et al (1994). In an epitaxial thin film, the most important contributions to the magnetic anisotropy energy are generally the magnetocrystalline (MC), the magnetostatic (MS), the magnetoelastic (ME) and the surface Néel magnetic anisotropy energies. Here, we neglect the MC anisotropy because this energy is approximately 1% of the others for Ni films thinner than 1000Å. Let θ be the angle that the magnetization vector makes with the film normal.

In the following treatment, we assume the biaxial misfit strain previously described as Eq.(2.5.8) in section 2.5. Substituting the strain tensor Eq.(2.5.8) into the f_{ME} in Eq.(1.1) and keeping only angle dependent terms leads to:

$$f_{ME}^{(100)} = 2B_1 e_0 \sin^2\theta \qquad (4.4.1)$$

For a thin film grown epitaxially with a [111] orientation on a (111) oriented substrate, it has been shown (F. J. A. den Broeder, at al,1991) (Akira Yamaguchi,et al,1993) that

$$f_{ME}^{(111)} = 2B_2 e_0 \sin^2\theta \qquad (4.4.2)$$

Thus the total magnetic anisotropy energy density of a thin ferromagnetic film sandwiched between two identical non-magnetic layers can be given in cgs units as:

$$\begin{aligned} f &= f_{MS} + f_N + f_{ME} \\ &= [\, -2\pi M_S^2 + 2K_N/t + 2\, B\cdot e_0]\, \sin^2\theta \\ &= K^{eff} \sin^2\theta \end{aligned} \qquad (4.4.3)$$

$-2\pi M_S^2$ and $2K_N/t$ represent the magnetostatic and Néel anisotropy energy densities where t is the thickness of the ferromagnetic nickel film. Thus we can express the effective anisotropy of the each surface as Eqs.(4.4.4) and (4.4.5).

$$K^{eff}_{(100)} = 2B_1 e_O - 2\pi M_S^2 + 2K_{N(100)}/t \qquad (4.4.4)$$

$$K^{eff}_{(111)} = 2B_2 e_O - 2\pi M_S^2 + 2K_{N(111)}/t \qquad (4.4.5)$$

The dependence of the effective anisotropy energy density on Ni thickness was measured recently by Jungblut *et al* (1994) and their results are shown in Fig.(4.4.3). Solid dots in Fig.(4.4.3) (a) and (b) show the data of $K^{eff} \cdot t$ vs t for (100) and (111) oriented sandwiches, respectively.

Above the critical thickness t_c, it has been shown (Chappert et al, 1988) that for epitaxial Ni thin films deposited on Cu(100) substrates the average in-plane biaxial strain follows closely the form:

$$e_O = \eta\, t_c / t \qquad (4.4.6)$$

where η =2.6% is the Ni/Cu lattice mismatch and t is the thickness of the Ni film. The data are shown in Fig.(4.4.4). Substituting Eq.(4.4.6) in Eqs.(4.4.4) and (4.4.5), we obtain:

$$K^{eff}_{(100)} \cdot t = -2\pi M_S^2 \cdot t + 2(B_1^{bulk}\, \eta\, t_{c(100)} + K_{N(100)}) \qquad (4.4.7)$$

$$K^{eff}_{(111)} \cdot t = -2\pi M_S^2 \cdot t + 2(B_2^{bulk}\, \eta\, t_{c(111)} + K_{N(111)}) \qquad (4.4.8)$$

Jungblut *et al.* (1994) argue that it is possible to apply the form of the strain in Eq.(4.4.6) for their Cu/Ni/Cu sandwiches with a modified critical thickness, namely t_c = 40Å and t_c = 35Å for (100) and (111) oriented sandwiches, respectively. These values are about twice those calculated from Matthews-Blakeslee theory (1975). Jungblut propose that they can get K_N through the linear fits of t for the Eqs.(4.4.7) and (4.4.8) with constant B's assumed from bulk values as shown a sloid lines in Fig.(4.4.3).

However, based on the Néel model in section 2.5 and as confirmed experimentally in the previous sections 4.1 to 4.3 (O.Song, 1994), we can proceed a step further and expand the first order magnetoelastic coupling coefficients B_1 and B_2 in the Néel form:

$$B_1 = B_1^{bulk} + B_1^{surface}/t \qquad (4.4.9)$$

$$B_2 = B_2^{bulk} + B_2^{surface}/t \qquad (4.4.10)$$

Substitutting Eqs.(4.4.9) and (4.4.10) in Eqs. (4.4.7) and (4.4.8) repectively, we obtain:

$$K^{eff}_{(100)} \cdot t = 2(B_1^{bulk} \eta\, t_{c(100)} + K_{N\,(100)}) - 2\pi M_S^2 \cdot t + 2B_1^{surface} \eta\, t_{c(100)}/t \qquad (4.4.11)$$

$$K^{eff}_{(111)} \cdot t = 2(B_2^{bulk} \eta\, t_{c(111)} + K_{N\,(111)}) - 2\pi M_S^2 \cdot t + 2B_2^{surface} \eta\, t_{c(111)}/t \qquad (4.4.12)$$

Solid curves in Fig.(4.4.3) indicate the curve fit given as a form of Eqs.(4.4.11) and (4.4.12) which are linear combinations of t and 1/t. From such a fit, with known values of B_1^{bulk} and B_2^{bulk}, we can get an indirect measure of the $B_1^{surface}$, $B_2^{surface}$, $K_{N\,(100)}$ and $K_{N\,(111)}$. The values that we obtained for the magnetoelastic coupling coefficients and the Néel magnetic interface anisotropy are sum marized in Table 4.4.1.

Table 4.4.1. Bulk and surface magnetoelastic coupling coefficients and K_N for single crystal Ni. (Determined from Bochi's method applied to Jungblut's data.)

B_1^b (J/m^3)	B_2^b (J/m^3)	B_1^s (J/m^2)	B_2^s (J/m^2)	$K_{N(100)}$ (J/m^2)	$K_{N(111)}$ (J/m^2)
6.2×10^6	8.5×10^6	-1.97×10^{-2}	-0.366×10^{-2}	-1.03×10^{-2}	-0.09×10^{-2}

In Fig.(4.4.5), we plot B_1^{eff} and B_2^{eff} versus film thickness for single crystal Ni using the results in Table 4.4.1. In both cases, the effective magnetoelastic coupling goes from a positive bulk value to a large negative value as the film gets thinner. The cross over in the sign of the coefficients occurs at t = 30Å for B_1^{eff} and t = 8Å for B_2^{eff}. The estimate of $K_{N\,(111)}$ (-0.9 erg/cm^2) is of the same order of magnitude as the value obtained by Gradmann (1986)(-0.22 erg/cm^2). Also, it is of interest to note that the surface magnetoelastic coupling coefficient for polycrystalline Ni deposited on SiO_2/ Si is B_1^s = $+2 \times 10^{-2}$ J/m^2 as showed already in section 4.3, while B_1^s from Jungblut's data fit given as $B_1^s = -1.97 \times 10^{-2}$ J/m^2. The B^s 's in polycrystalline and single crystal Ni films are of the same order of magnitude but of opposite signs.

The signs of B's determined here for Cu/Ni/Cu epitaxial films are consistent with the Néel model calculated with the in-plane biaxial misfit strains as discussed in section 2.5. The discrepancy of the magnitude of B^s 's calculated in the Néel model (B_1^s : -5.25×10^{-4} J/m^2) and that from the Jungblut's data fit (B_1^s : -1.97×10^{-2} J/m^2) can be samller if we consider strain dependence on film thickness and the exchange coupling in the Néel model calculation.

In conclusion, it is possible to determine surface magnetoelastic coupling coefficients in thin epitaxial films whose anisotropy energy is too large to allow measurements by our four-point bending method. By measuring the total effective anisotropy energy density as a funtion of film thickness, we can estimate B^s 's and K_N 's indirectly. The values determined in epitaxial Cu/Ni/Cu(100) from Jungblut's data are reasonable. We expect this fitting method can be improved if we consider more precise form of elastic strain and saturation magnetization behavior with respect to thickness.

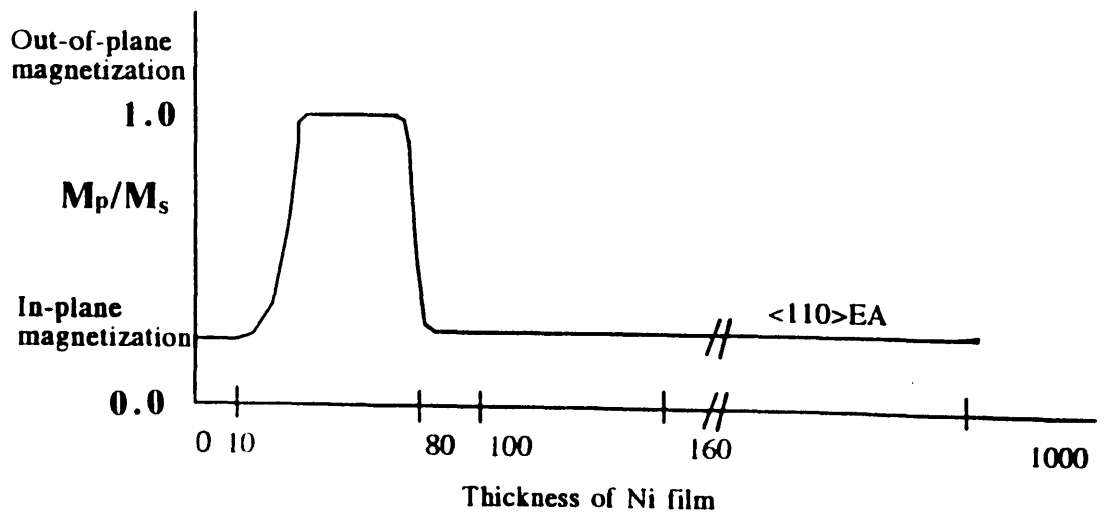

Fig. 4.4.1. The change of magnetization direction of Ni(100)/Cu(100) epitaxial films with respect to Ni thickness.

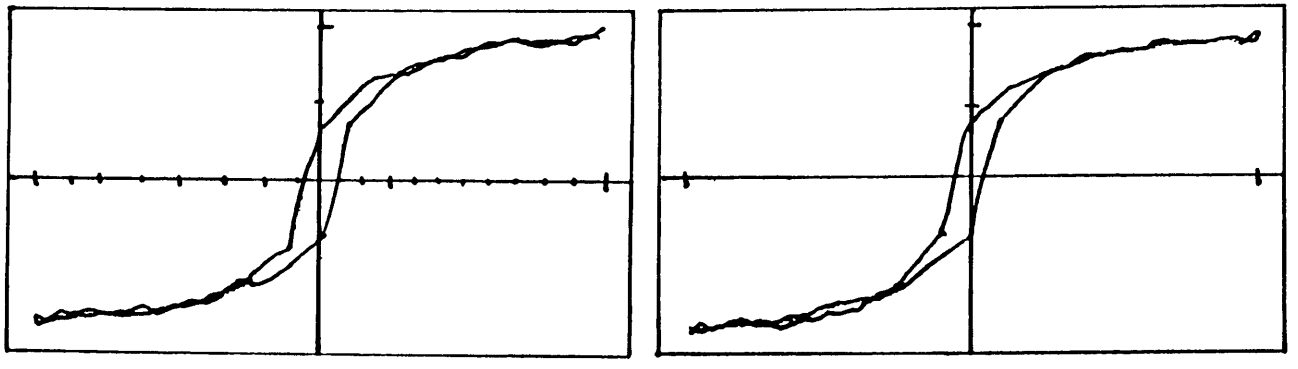

Fig.4.4.2. m-H hysteresis loops of Cu/Ni 500Å /Cu(100) film with strain. Measured *ex-situ* by VSM. Maximum applied magnetic filed was 5000 Oe.
(a) no external strain. (b) with -7×10^{-4} uniaxial imposed strain.

(a)

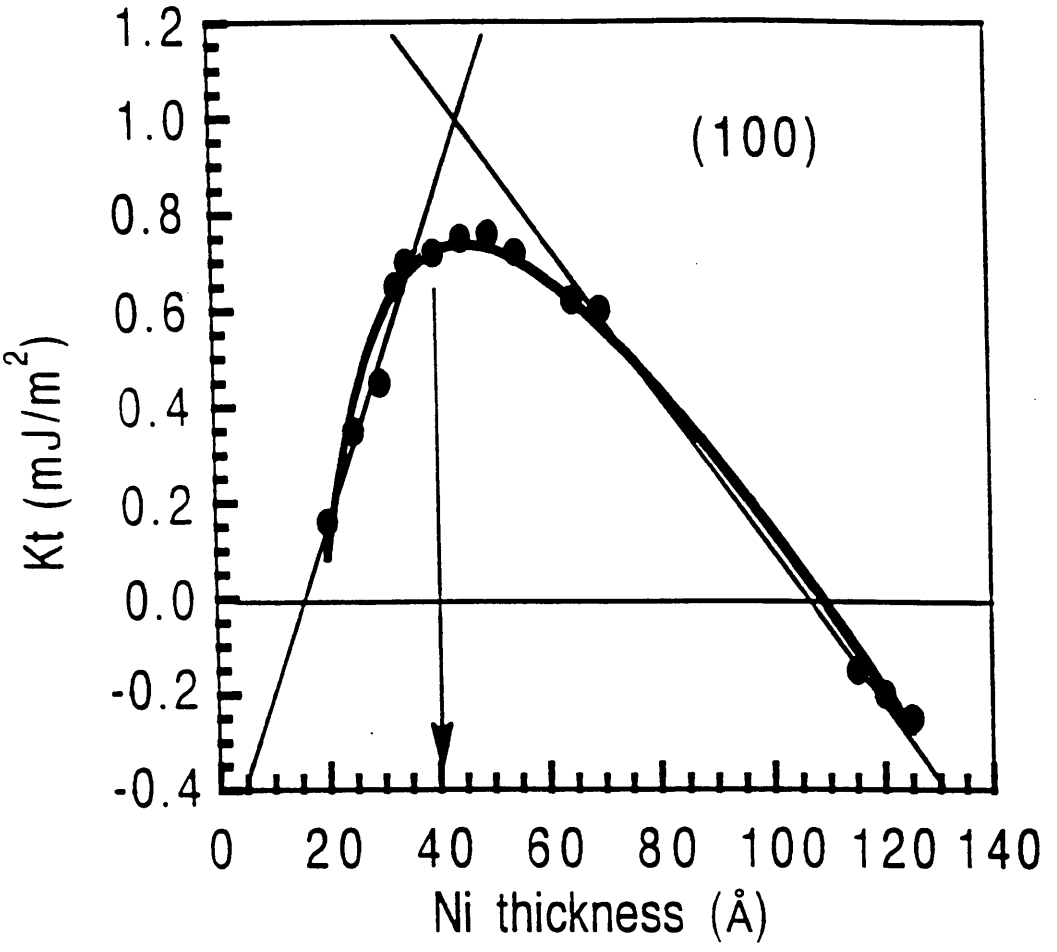

Fig.4.4.3. Plot of $K^{eff}t$ with Ni thickness. Data from Jungblut (1994). Solid curves are data curve fitting.

(a) (100) Ni surface (Cu/Ni(100)/Cu(100))

(b) (111) Ni surface (Cu/Ni(111)/Cu(100)).

(b)

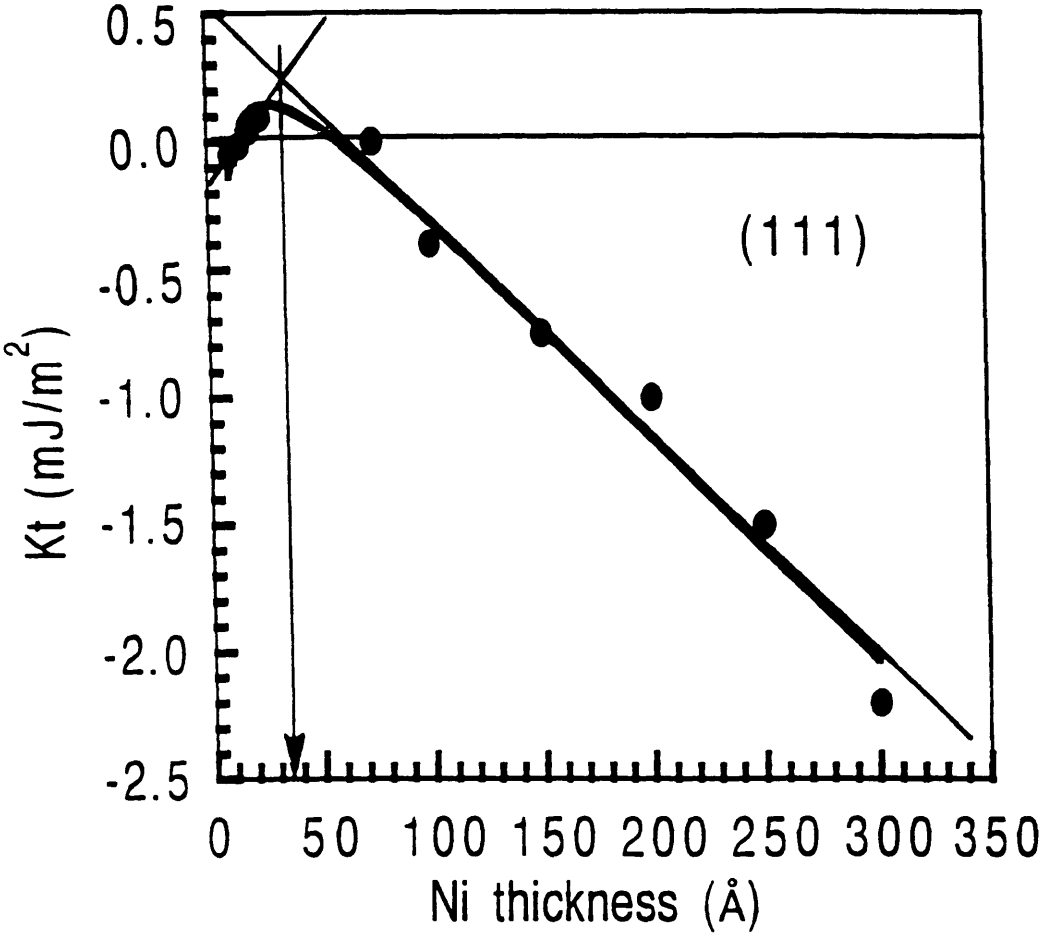

(b) (111) Ni surface (Cu/Ni(111)/Cu(100)).

(a)

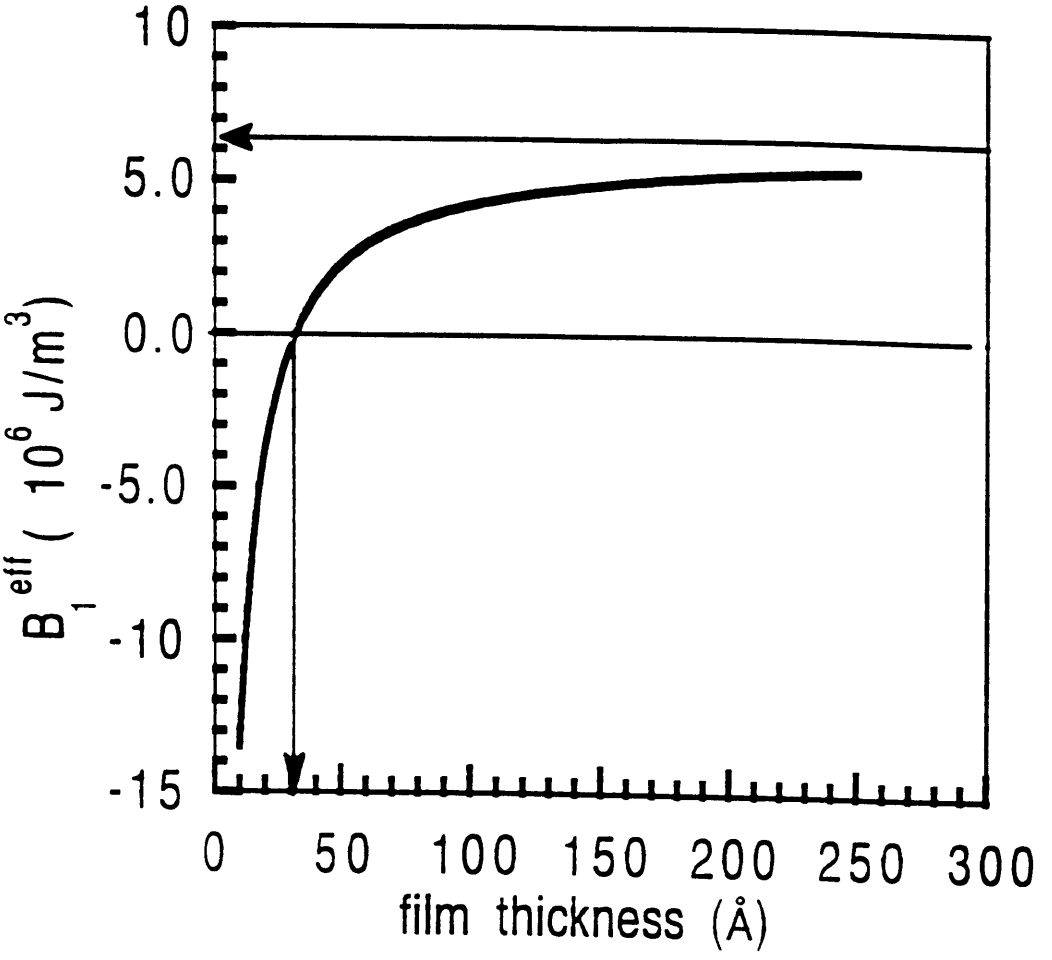

Fig.4.4.5. Plots of extracted magnetoelastic coupling coefficients in Cu/Ni/Cu.
(a) $B_1^{eff} = [6.2 - 192/t(Å)]$ ($x10^6$ J/m^3)
(b) $B_2^{eff} = [8.5 - 37/t(Å)]$ ($x10^6$ J/m^3)

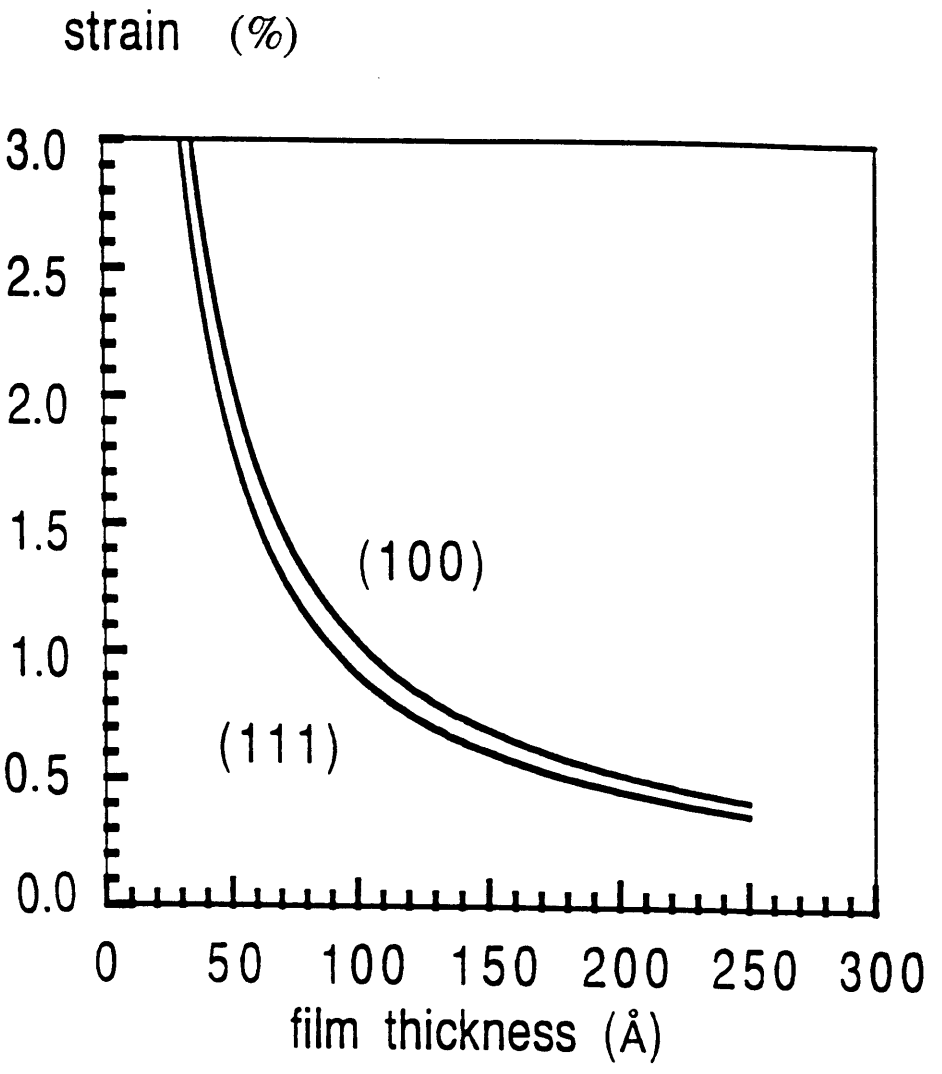

Fig.4.4.4. Illustration of averaged strain with film thickness.

(b)

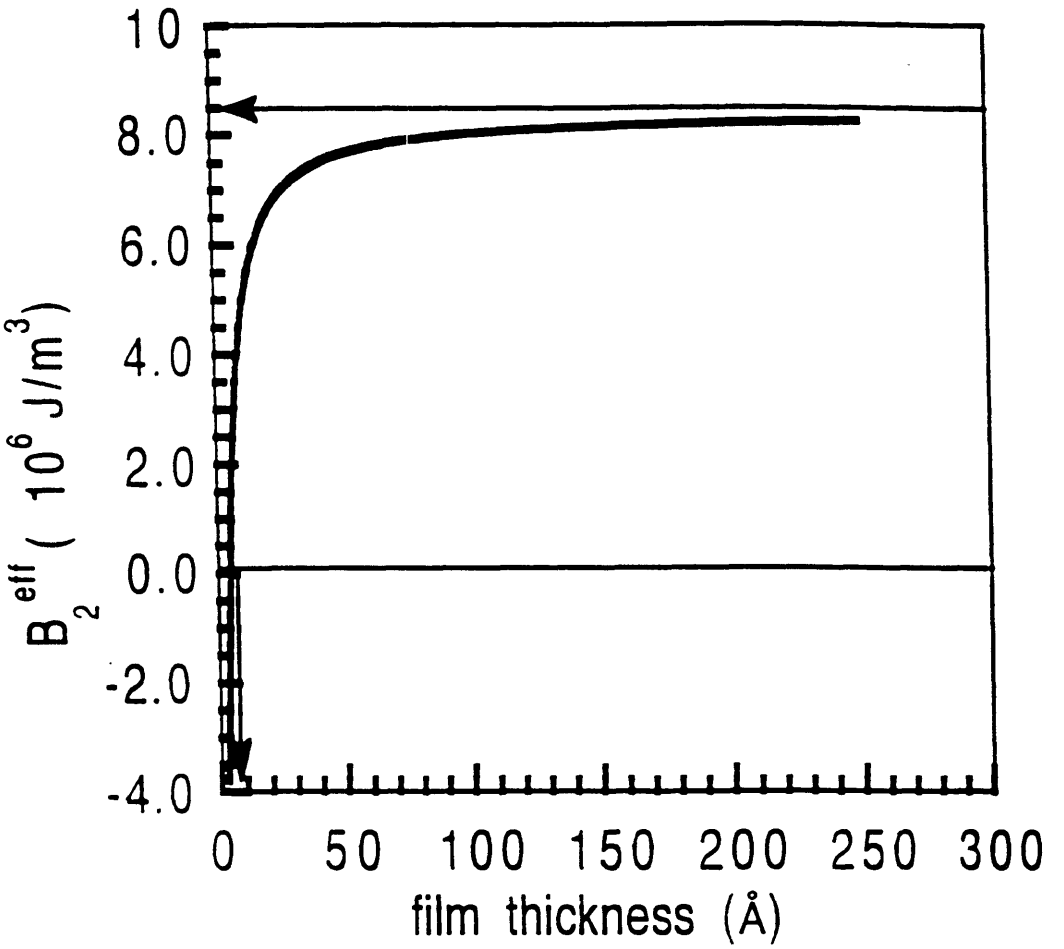

(b) $B_2^{eff} = [8.5 - 37/t(Å)]$ $(x10^6\ J/m^3)$

4.5 Microstructure of the magnetic films

The observation of an effect in the strain-dependent part of the magnetic anisotropy, $B^{eff.}e$, that varies inversely with film thickness parallels the prediction of Néel and numerous observations of similar effects in the strain-independent magnetic anisotropy K^{eff}. The most difficult issue facing both of these observations is establishing the origin of the 1/t dependence. Is it of fundamental origin as predicted by Néel or is it result of strain, microstructural, or other effects which become exaggerated in thin films? The ultimate answer is probably a combination of many effects.

We examined the microstructure of the magnetic films with a transmission electron microscope (TEM) and a Auger depth profiling in order to provide the information about the role of grain growth, texture and interfacial mixing on the surface ME effect. More specially we seek to determine:

(i) Whether the abrupt change of magnetoelastic coupling coefficients near the surface is a result of the specific growth process such as the islands growth mechanism .

(ii) Whether the grains in our polycrystalline magnetic films are randomly oriented or have a prefered orientation.

(iii) Whether the existence of magnetically different layers from the intermixing of elements between magnetic films and substrates or the formation of compounds plays a role in the surface ME effect.

Fig.4.5.1.(a) is a typical micrograph of the intermediate silver layer of permalloy/ 2000Å silver/ Si(100) films. The micrograph reveals that the layer consists of many small grains of diameter in the range 60 - 100 nm and some large recrystallized grains having diameters of order 0.3 μm. Fig.4.5.1.(b) is the selected area diffraction pattern (SADP) micrograph of the fcc silver layer showing a homogeneous ring pattern which indicates no prefered orientation. The small particles around the ring patterns result from usage of a small aperture during the observation. The AFM image in Fig.4.5.2.(a) shows that the grain size of this silver layer is 1000Å in diameter, which is consistent with the small grains seen in TEM, with the surface roughness of ±15Å. The small clusters in Fig.4.5.2.(a) with size of 200Å in diameter may be the initial surface oxide nuclei. Fig.4.5.2.(b) is an AFM image taken after deposition of a 40Å permalloy film on the Ag surface in (a). It shows that the morphology and surface roughness of the permalloy specimen is similar to those of the silver substrate even for a permalloy thickness of 40 Å.

Fig.4.5.3.(a) is a TEM micrograph of permalloy of film thickness 120Å on a silver substrate. The overall morphology of this specimen apparently to be identical to that of the silver substrate in Fig.4.5.1.(a). The small particles seen over the larger grains of the silver substrates indicate the contrast of the permalloy film. Fig.4.5.3.(b) is the SADP showing the random oriented fcc permalloy (γ-phase) diffraction patterns with (111) dot patterns from the large (111) silver grain underneath the permalloy film. Here we can say that our permalloy film is continuous and shows no prefered orientation at the thickness of 120Å on the silver substrate.

To demonstrate the microstructural evolution during magnetic film growth, we prepared permalloy films with thicknesses of 10, 15, 30 and 120Å on formvar substrates. Formvar is an electron transparent substrate that is useful in imaging some deposited materials whose substrates are difficult to thin.

Fig.4.5.4.(a) is the micrograph of the permalloy film with thickness of 10Å grown on a formvar substrate. It shows that permalloy on formvar is continuous. The SADP of this film in Fig.4.5.4.(b) can be compared with that of formvar itself as shown in Fig.4.5.4.(c). The new ring patterns in Fig.4.5.4.(b) in addition to pattterns of formvar in Fig.4.5.4.(c) indicate the existence of the magnetic films that we deposited. However these new rings are not consistent with the diffraction patterns of the thicker permalloy film in Fig.4.5.6.(b). This may be reasonable because the magnetic film can be oxidized easily in this thickness range during *ex-situ* TEM sample preparation. These results suggest that we have continous magnetic permalloy films during *in-situ* magnetoelastic coupling experiments above thicknesses of 10Å.

Fig.4.5.5.(a) is the micrograph of the permalloy film with thickness of 15Å on formvar. This shows that the film is continuous and thicker compared with Fig.4.5.4.(a). The grains show a slightly better definition. The SADP as shown in Fig.4.5.5.(b) indicates the additional ring patterns appear as thickness increased by 5Å.

Fig.4.5.6.(a) is the micrograph of the permalloy film with thickness of 120Å on formvar. Here the grains are well defined and appear to be of order of 10 nm in diameters. Fig.4.5.6.(b) shows clear diffraction patterns of the permalloy. This SADP may compared with that of the Fig.4.5.3.(b). The smaller diffraction patterns in Fig.4.5.3.(b) (20% of reduction in the most intense diffraction pattern) implies the silver with lattice parameter larger than that of fcc nickel can be dissolved from the substrate into permalloy to form a metastable solid solution accoring to Vegard's law. This may be associated with the 7Å of magnetically different layer discussed in section 4.4.1.

Fig.4.5.3 to 4.5.6 verify that our pemalloy films are continuous with random orientations in the thickness range of our magnetoelatic coupling experiment. This implies that large surface magnetoelastic coupling coefficients are not due to discontinuous film morphology at small thickness.

Fig.4.5.7.(a) is the micrograph of polycrystallne Ni of thickness 50Å on Si wafer. The mophology of this sample demostrates that it also is continuous. Fig.4.5.7.(b) shows a selected area diffraction pattern of the nickel. It shows polycrystalline Ni does not have significant prefered orientation. The average grain size is estimated to be approximately 1000 Å. The nickel silicide SAPD in Fig.4.5.7.(c) is determined to be Ni_3Si among 14 possible nickel silicides, according to the JCPDS data file. We also studied a 100Å Ni/Si sample and found the Ni and Ni_3Si SADP's to be essentially the same as those observed here for 50Å Ni/Si.

To verify the continuity of the nickel films and random orientation during film growth, thicknesses of 30Å and 500Å of polycrystalline nickel films are prepared on formvar substrates. Fig.4.5.8.(a) is the micrograph of the 30Å nickel film on formvar. It indicates the existence of a continuous and uniform film layer. The SADP in Fig.4.5.8.(b) shows strong fcc nickel diffraction patterns.

The micrograph shown in Fig.4.5.9.(a) is the image of the polycrystalline Ni film with thickness of 500Å. The SADP of this nickel film is identical to the standard diffraction patterns. (Fig.4.5.9.(b)). If we compare this SADP with that of Fig.4.5.7.(b), we observe significant (16%) shrinkage of the patterns in Ni on Si compared to Ni/formvar. Solid solution formation between Ni and Si penetrating the thin natural silicon dioxide (SiO_2) layer and formation of Ni_3Si silicide can explain this. Moreover the formation of silicide and solid solution between Ni and Si is a possible explanation of 55Å of magnetically different layer needed to fit in our data to the Néel model as in section 4.4.3.

Also, Auger depth profiling was performed in order to study the intermixing layers. Comparing the behavior of permalloy/Ag and permalloy/Cu films, both nominally 30Å thick, as shown in Fig.(4.5.10).(a) and (b) respectively, we observed permalloy/Cu shows a more diffuse interface than does NiFe/Ag. Sputtering was performed with a gun voltage of 2 kV, sputter rate of 12Å/min, scale factor of 826.97 k c/s for (a) and 346.64 k c/s for (b). If we set the nominal interface as 150 sec of sputtering time, then we get

around 5Å of permalloy/Ag solid solution layer in Fig.(4.5.10).(a) and 15Å of permalloy/Cu mixing layer in Fig.(4.5.10).(b). These mixing layers can be a explanation for the magnetic different layers which we assumed in sections 4.1 and 4.2 to fit the data to the Néel model more appropriately. However, since Auger depth profiling can have sputter induced intermixing, determination of precise intermixing layer thickness and nominal interface location is not fully reliable.

In summary, TEM micrographs verify that magnetic films are continuous and uniform and display no prefered orientation. The result of the SADP's show that the formation of NiFe-Ag and Ni-Si solid solution and Ni_3Si silicide at the interface may provide strong evidence for the magnetically different layers. Moreover, Auger depth profiling on NiFe-Ag and NiFe-Cu reveals that some chemical interactions occur at the interfaces.

The existence of intermixing layer or compound layer can affect the form of the result as $B^{eff} = B^b + B^s/(t-t_o)$ but these chemical interactions are not responsible for the B^s/t behavior.

Still, we can not exclude completely the microstructural effect on our results as shown in sections 4.1 to 4.4, because of the limitation and practical problems of our probe facility. However, we can confirm that our experimental results are not from the discontinuity or prefered orientation of the thinnest magnetic film.

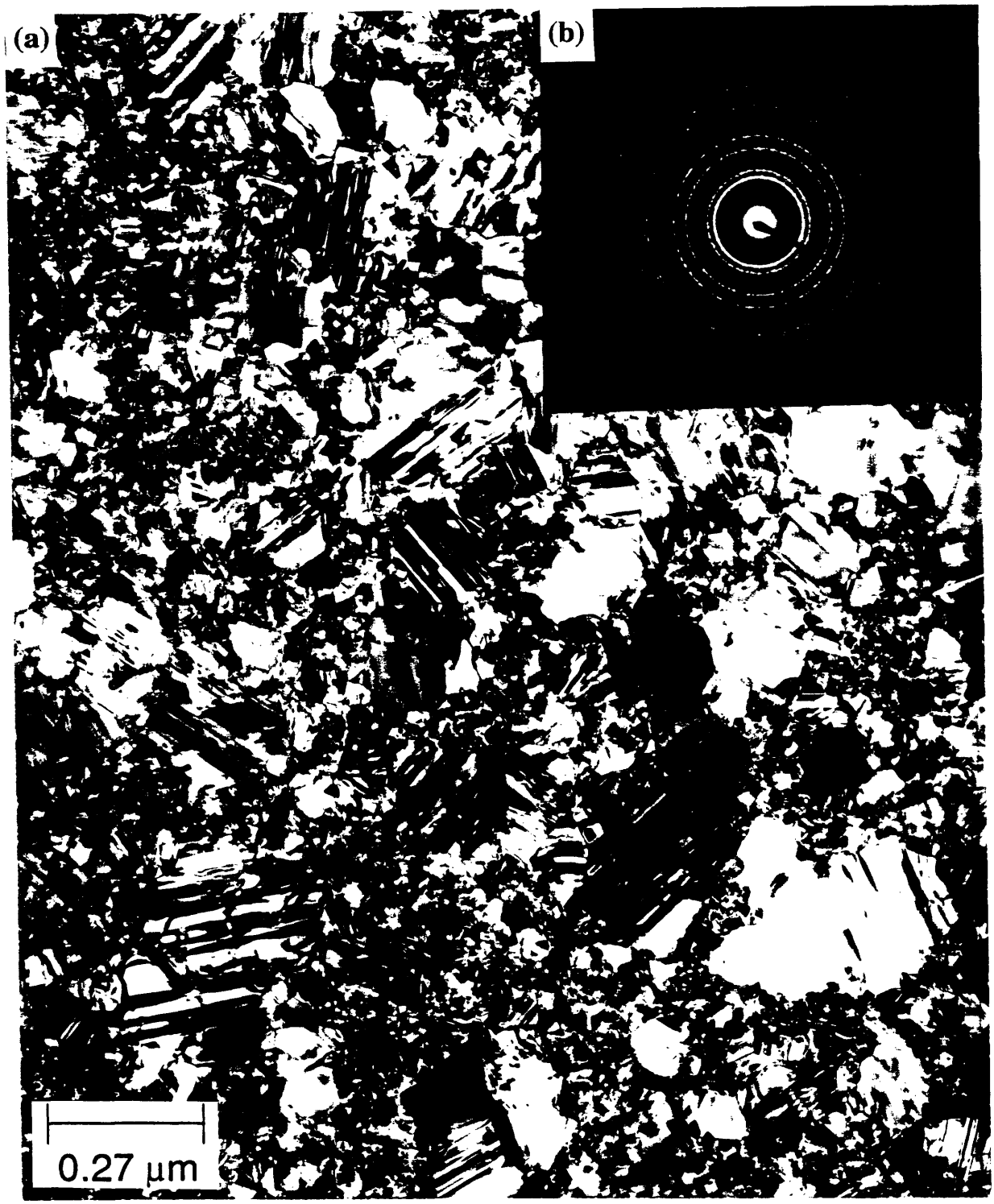

Fig.4.5.1. TEM micrographs of 2000Å silver layer.
(a) Bright field image (b) Selected area diffraction pattern (SADP)

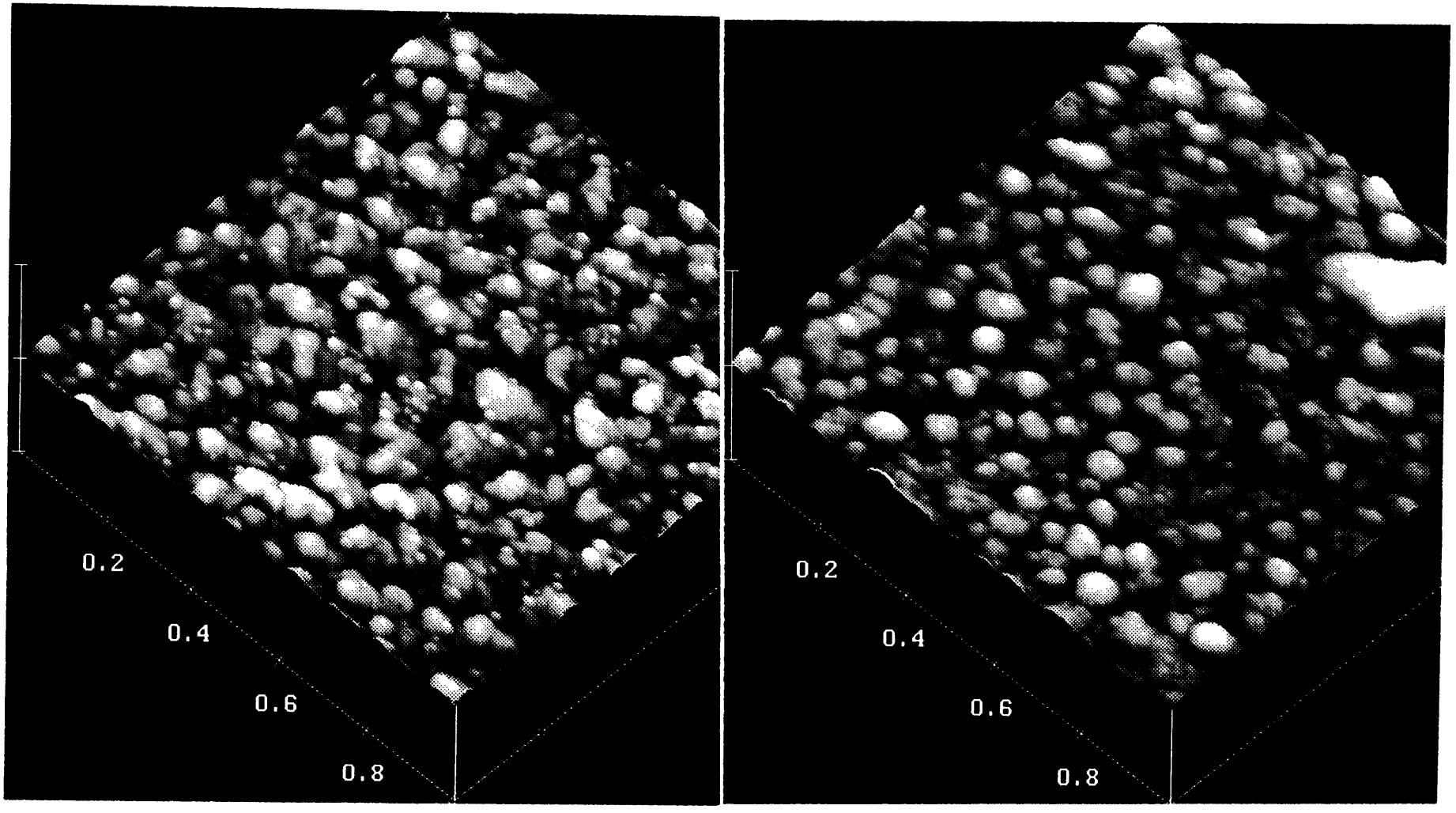

Fig.4.5.2. AFM micrographs
(a) 2000Å Ag/ Si(100)
(b) 40Å permalloy/ 2000Å Ag/ Si(100)

Fig.4.5.3. TEM micrographs of 120Å permalloy film/ 2000Å Ag layer.
(a) Bright field image (b) SADP

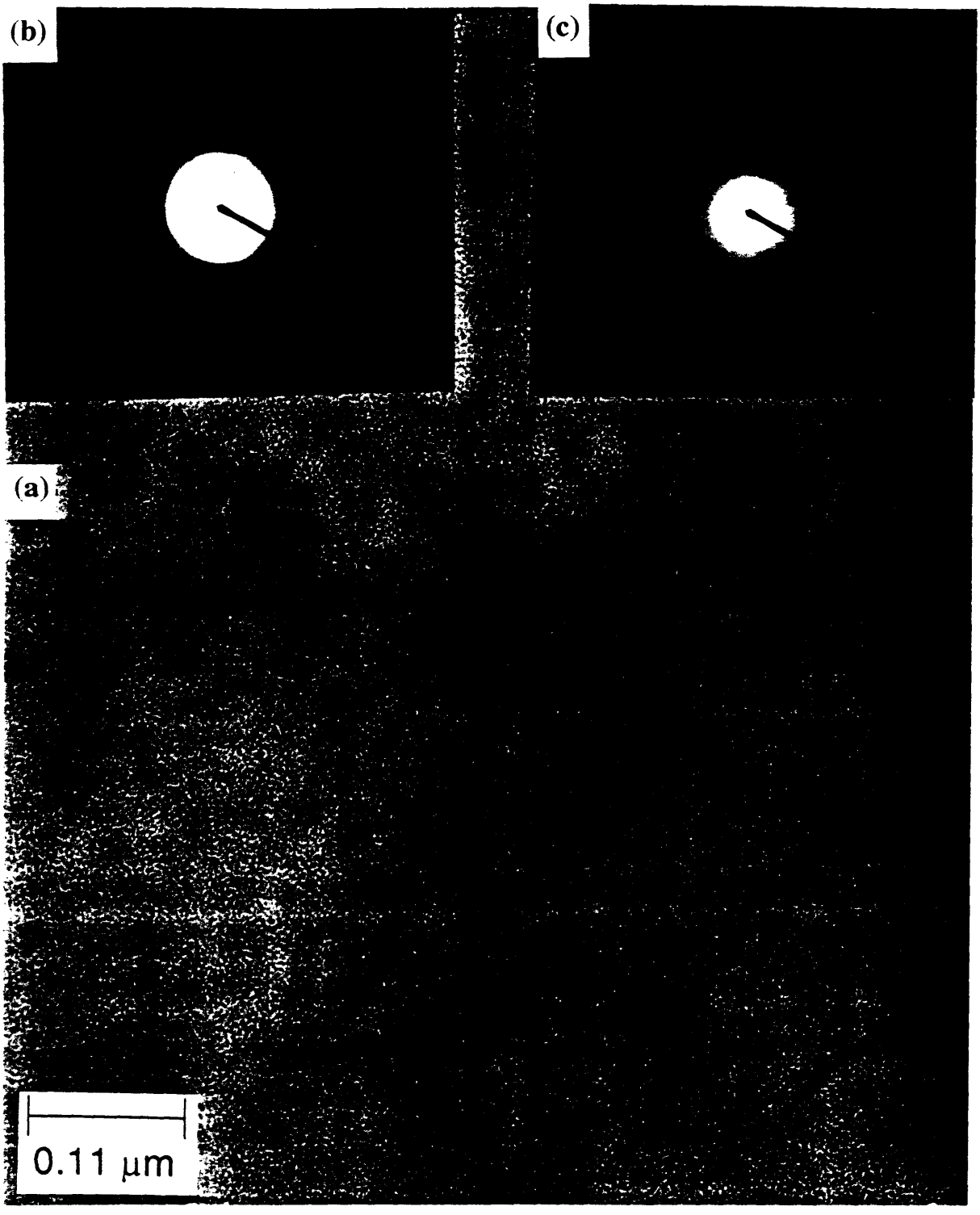

Fig.4.5.4. TEM micrographs of 10Å permalloy film/ formvar.

(a) Bright field image

(b) SADP of 10Å permalloy

(c) SADP of formvar

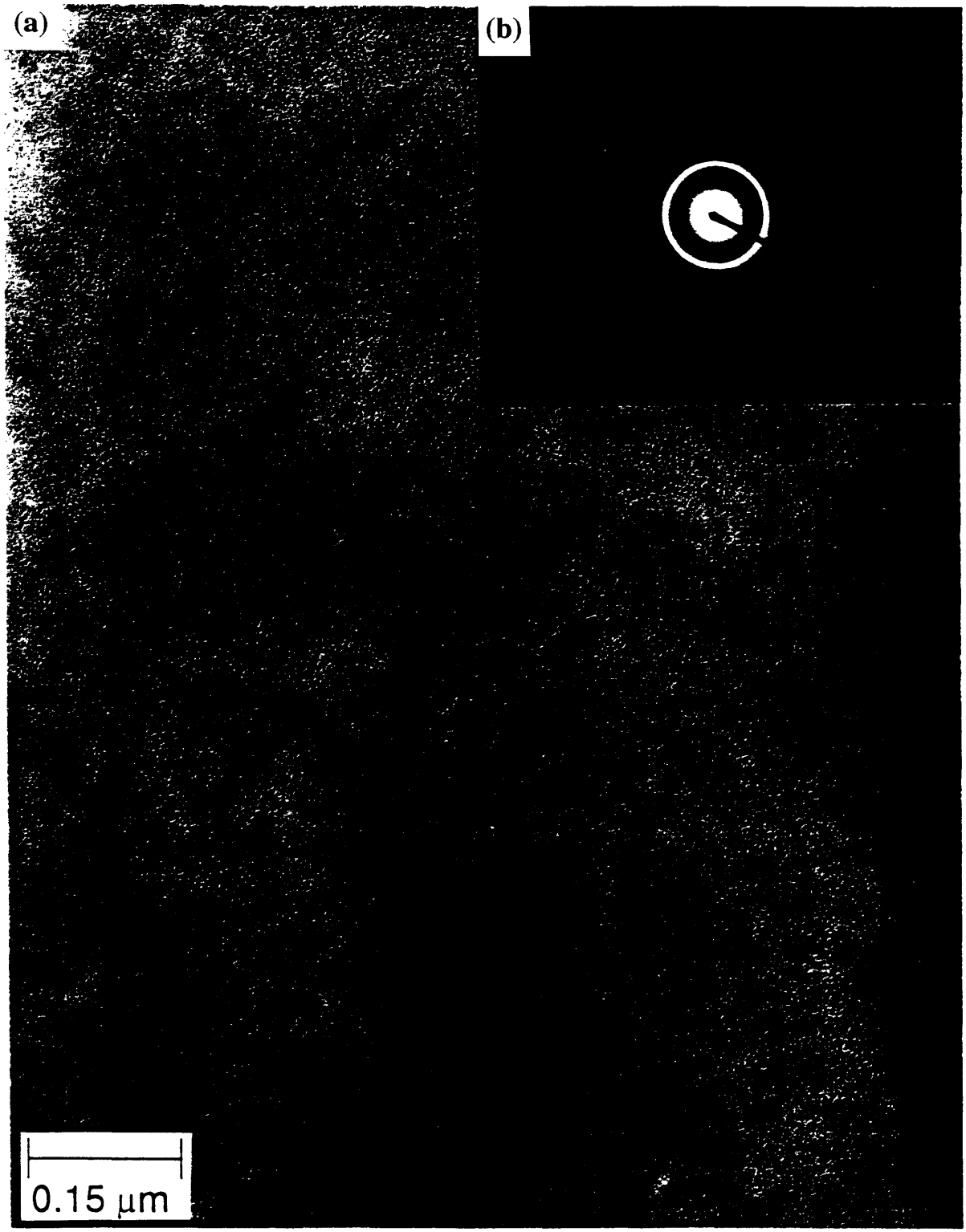

Fig.4.5.5. TEM micrographs of 15Å permalloy film/ formvar.
(a) Bright field image
(b) SADP of 15Å permalloy

Fig.4.5.6. TEM micrographs of 120Å permalloy film/ formvar.

(a) Bright field image

(b) SADP of 120Å permalloy

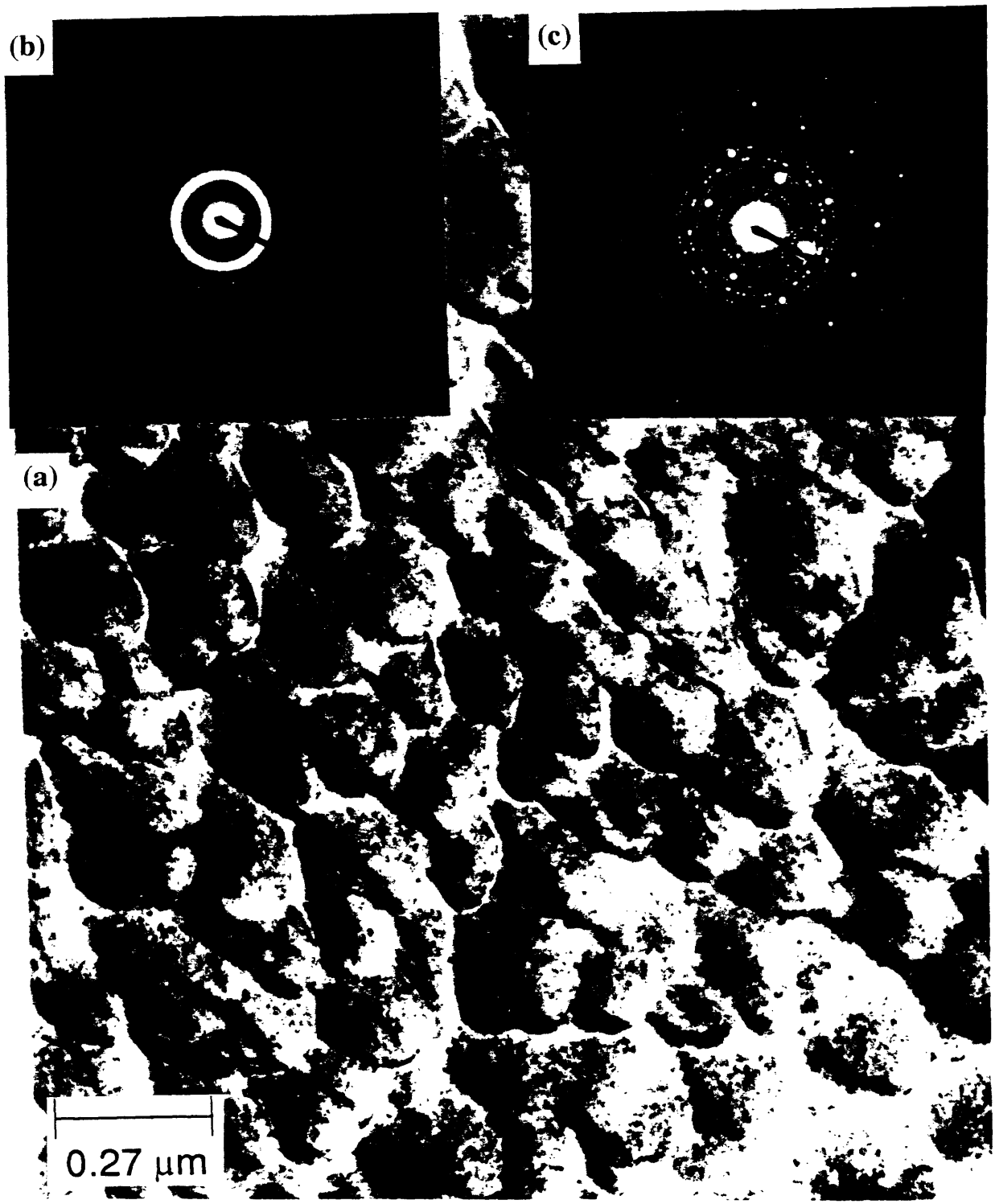

Fig.4.5.7. TEM micrographs of 50Å Ni/ SiO_2/Si.

(a) Bright field image

(b) SADP of Ni

(c) SADP of nickel silicide

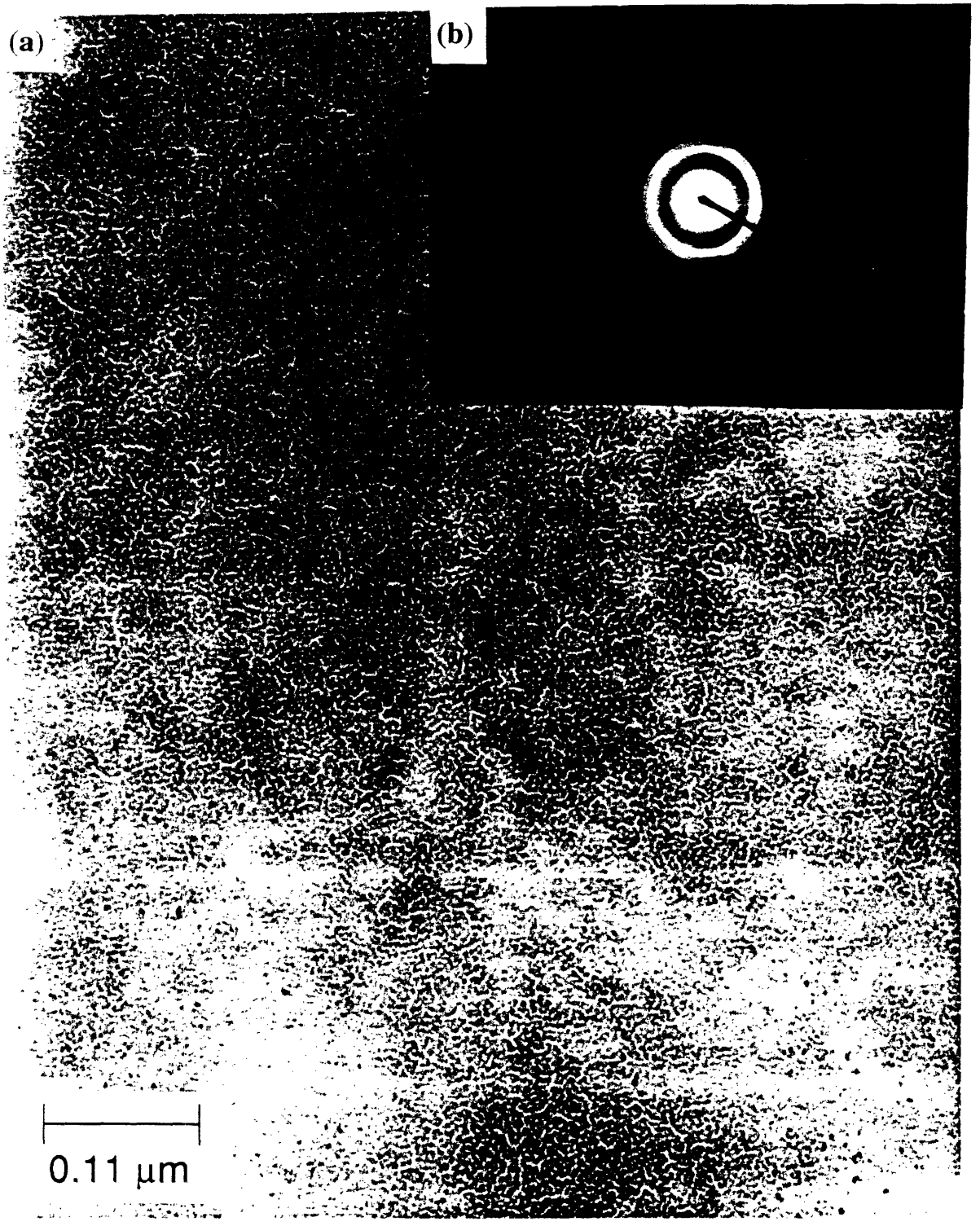

Fig.4.5.8. TEM micrographs of 30Å Ni/ formvar.

(a) Bright field image

(b) SADP of Ni

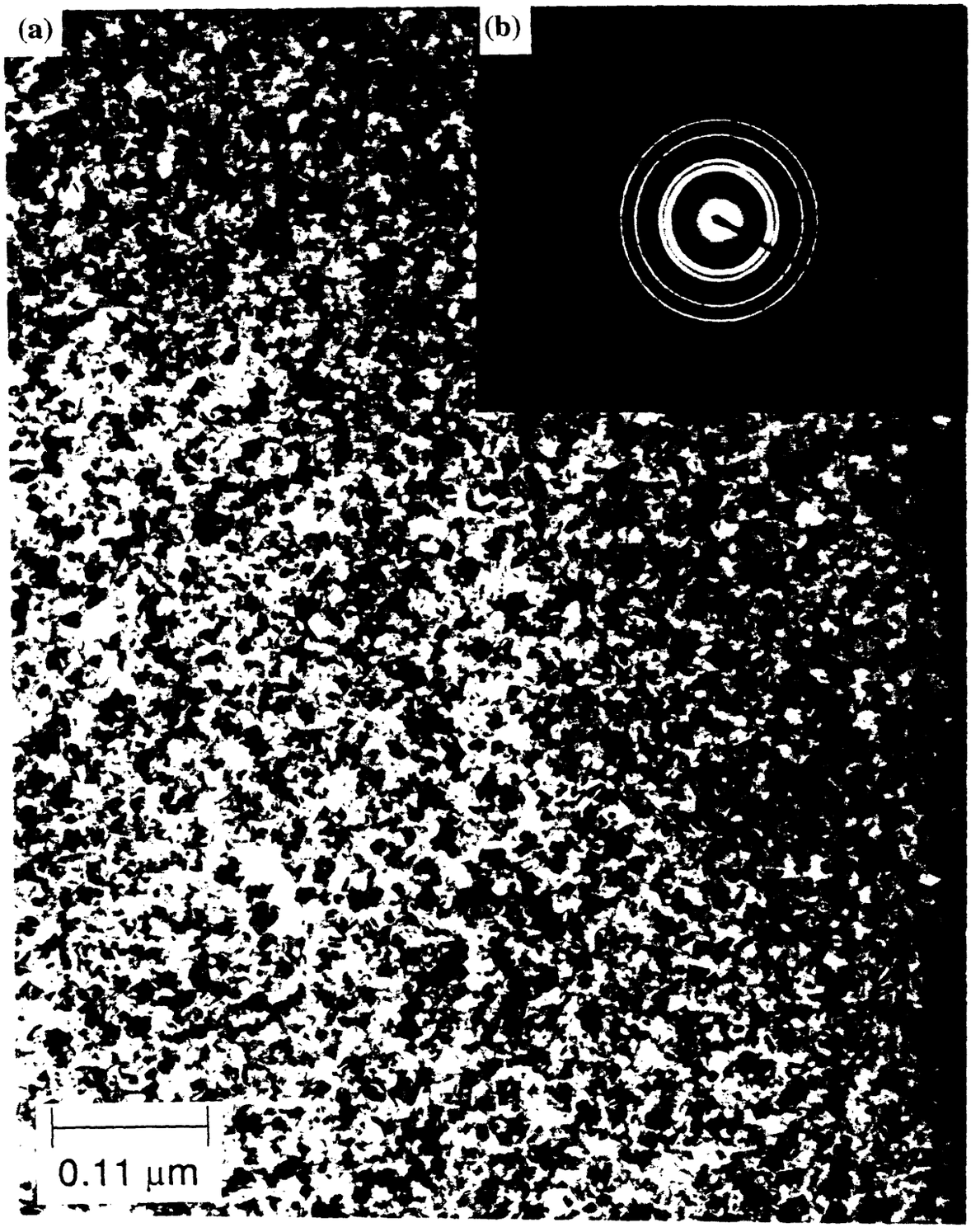

Fig.4.5.9. TEM micrographs of 500Å Ni/ formvar.
(a) Bright field image
(b) SADP of Ni

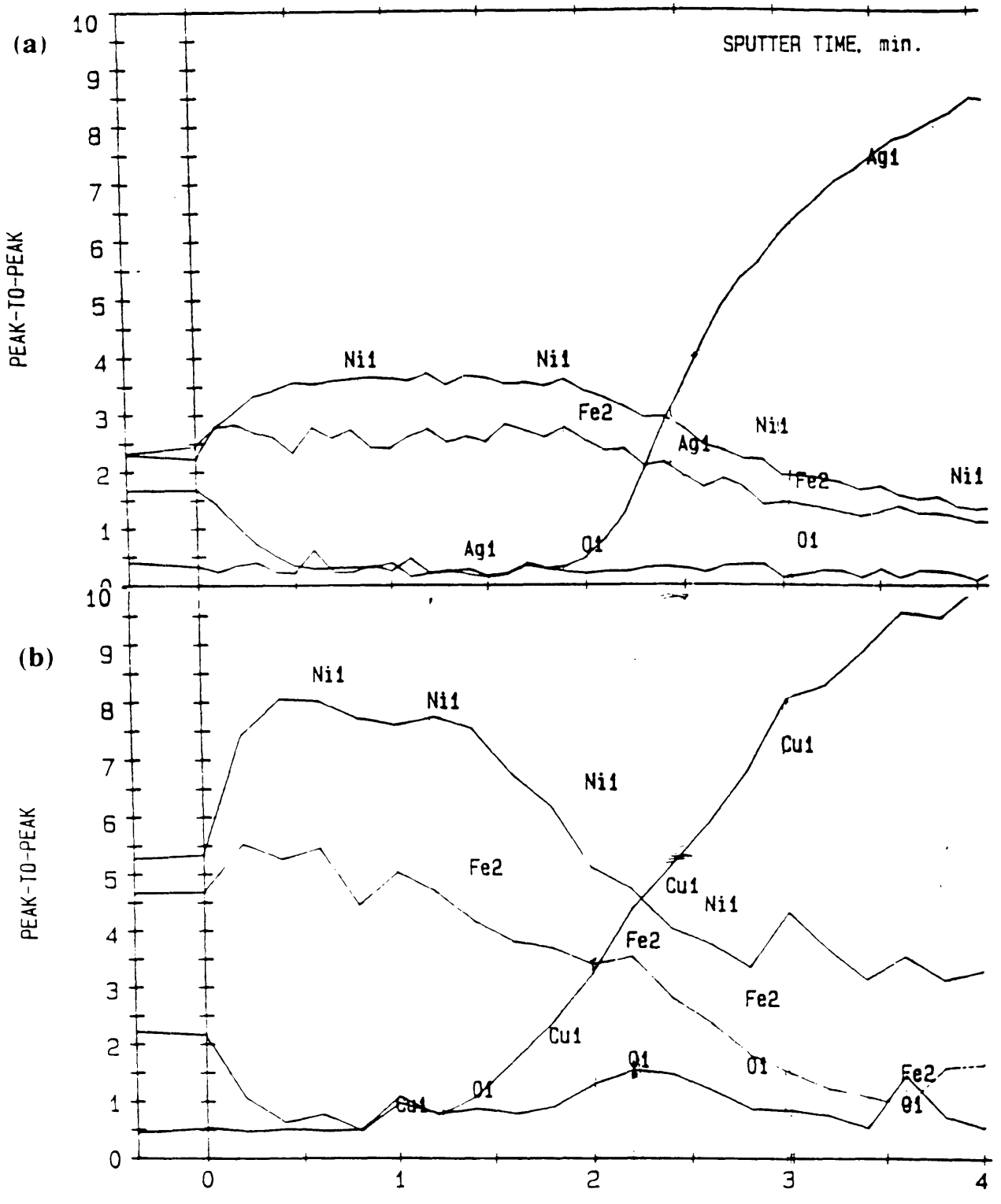

Fig.4.5.10 Auger depth profiling. Peak-to-peak profile with sputtering time (min).

(a) 30Å NiFe / Ag

(b) 30Å NiFe / Cu

5. Discussion

Table 5.1 below summarizes the parameters used to fit the data in sections 4.1, 4.2, 4.3 and 4.4. and the accepted bulk values for the magnetoelastic coupling coefficients. It also shows the magnetostatic energy, $\mu_o M_s^2/2$, which tends to maintain in-plane magnetization. Finally, it shows the critical thickness t_c, below which the measured surface anisotropy $B^s \cdot e/t$ overcomes the magnetostatic energy for an assumed misfit strain of 1.5%. Then, we obtain $t_c - t_o$:

$$t_c - t_o = B^s \cdot e / (\mu_o M_s^2/2 - B^b \cdot e) \qquad (5.1).$$

These numbers will be discussed later.

Table.5.1. Summary of the experimental results

	B^{bulk} (J/m^3)	$B^{surface}$ (J/m^2)	t_o(Å)	accepted B^{bulk}	$\mu_o M_s^2/2$(J/m^3)	$t_c - t_o$(Å)
NiFe/Ag	-0.78×10^5	1.4×10^{-4}	7	$<\lvert 1.0\times10^5\rvert$	2×10^5	0.10
NiFe/Cu	-0.76×10^5	3.45×10^{-4}	13	$<\lvert 1.0\times10^5\rvert$	2×10^5	0.26
Ni/SiO_2	5.6×10^6	1.86×10^{-2}	55	6.0×10^6	1.5×10^5	47
Cu/Ni(100)/Cu	6.2×10^6	-1.97×10^{-2}	-	6.2×10^6	1.5×10^5	-

Two aspects of our findings are worth more detailed discussion: 1) the appearance of a term in the effective magnetoelastic coupling having inverse thickness dependence, and 2) the need for the parameter t_o.

We discuss first some of the factors, other than an intrinsic surface effect, that could contribute to the observed surface anisotropy. We then discuss possible sources of the t_o term. This chapter ends with some suggestions for future work.

We have shown that B^{eff} can take on anomalously large values or even different signs in thin films relative to its value in thick films. A large surface value of any parameter by itself could result from an exaggeration or enhancement of the bulk value at the surface. However, a change of sign in a parameter at the surface suggests a different mechanism may be operating there. Nevertheless the possibility remains that surface anisotropy and

surface magnetoelastic coupling reflect a microstructure or chemical anomaly at the surface of a material rather than purely intrinsic effects. We consider several possibilities in order.

1. The assumption that elastic constants (c_{ij}) maintain their bulk values near the surface of a magnetic film may not be valid. What we measure is $B = -\lambda c_{ij}$, which contains the elastic constants so our measured values of B do not require an assumed value for c_{ij}. The anomalously large values near the surface may be related to an enhancement of elastic constant with decreasing film thickness. Supermodulus effects have been reported in thin films (Cammarata, 1989). These effects amount to approximately 50% increases in c_{ij}. We observe increases in B of as much as one order of magnitude. Further, we also observed a change of the sign of B from negative to positive in polycrystalline permalloy films with decreasing film thickness. The elastic constants should be always positive. Thus, while the elastic constants may be a function of the film thickness, they cannot be responsible for the full surface effect we observed in B^{eff} and they will not cause a change in the sign of B as film thickness decreases. The change of sign would rather be due to the change of sign for the effects on the magnetic spin direction by an the imposed strain in the thinnest film because of lowered symmetry at the surface.

2. As film thickness decreases, surface anisotropy becomes dominant as shown in Eq.(1.3). Thus, the reference anisotropy in polycrystalline permalloy and nickel films without imposed strain, may increase due to surface anisotropy. It has been speculated that this change in the unstressed anisotropy could alter our measured B^{eff}. Any change of the reference anisotropy with thickness would produce no first order effect on our measured B values which come from the area difference between the reference and strained m-H loops at a given film thickness.

3. It may be asked whethter the misfit strains between the individual grains and the substrate leave the film in a non-linear strain regime. If this were the case, the additional bending strain we impose to measure B^{eff} would not be reversible, i.e. after bending, the film would not return to its original state of anisotropy. No such hysteresis was observed within our ability to resolve it.

4. In this study, we assumed that the effects of misfit and differential thermal contraction produce a uniform strain across the whole magnetic film. As we observed in our microstructural study in section 4.5, our magnetic films were not formed by perfect layer-

by-layer growth nor by discontinuous island growth. Rather, they exhibit the features of Stranski-Krastanov (SK) growth, the combination of layer-by-layer and island modes, with a surface roughness of ± 15Å in films of thickness 40Å. The surface roughness was shown due to the microstructure of the substrates and films. The irregular surface and interface morphology in the thinnest film as shown in Fig.(4.5.2) makes the imposed strain non-uniform accordingly. The crests and troughs in the surface are subject to different strains. We need to consider whether this inhomogeneous strain may cause the anomaly of B in the thinnest films.

To appreciate such microstructural or surface roughness effects on our data, we may modify our general eqauation as :

$$B^{eff} = B^{b} + B^{s}/ (t-t_{o})^{n+1} \qquad (5.2)$$

Here we define n as a microstructural factor which might explain the deviation from the Néel form, $B^{s}/(t-t_{o})$. We can determine n mathematically from the slope on a plot of $\log(B^{eff} - B^{b})$ vs. $\log(t-t_{o})$. Through such a fit, we obtain n's of 0.01, 0.18 and 0.51 for permalloy on Ag and Cu, and nickel on silicon, respectively. The smallest value of n for permalloy on silver suggests that this system is the least affected by microstructural induced roughness effects. Another interpretation is that the intrinsic effect is so small not to contribute in this thickness range and the 1/t dependence is due to the thickness dependence of the surface roughness on microstructure. While we cannot completely rule out this possibility, it is unlikely because the microstructure appears to be independent of thickness in the range of interest.

Therefore, the values of B^{s} measured in our study are very likely dominated by the intrinsic surface effect and reflect extrinsic microstructural surface roughness effects to different degrees in different systems. The former stems from the lowered symmetry at surfaces and interfaces, while the latter results from the SK growth mode of our films. Our analysis based on the values of n suggests that to lessen the possible microstructural effects, immiscible and chemically stable substrates which prevent the formation of chemical compounds, are highly recommended.

We now discuss the magnetically different layer (of thickness t_{o}) which we need to fit our results. It is not a common part of the Néel model. We suggest two possible

origins of this parameter which suggests the existence of a surface layer that is magnetoelastically dead.

First, we discuss the exchange couping between surface and interior of the film. The strong anisotropy at the surface is coupled with the film interior by exchange interactions. If the magnetoelastic energy at the surface (B^Se/t) is much greater than the bulk anisotropy (K_u), then surface spins are strongly pinned and they will tend to pull the interior spins in their direction. The greater stength of the surface anisotropy may render it insensitive to the weak applied strain we use for our measurement.

If the surface and bulk anisotropy easy axis are both in-plane but at 90° to each other, then the magnetization will relax from the surface to bulk orientation over a distance of half about a Bloch wall width, $\pi(A/K)^{1/2}/2$. This effect would give t_o of order several hundred to 1000Å. If the the interior of the film has the magnetic easy axis parallel to the film and the surface anisotropy is out-of-plane, then the problem is slightly more difficult. The problem of determining the form and length scale of this interaction has been solved (O'Handley and Woods,1990) and it was shown that the surface orientation of $\mathbf{M_S}$ decays toward its interior orientation with a characteristic length, $\xi=(A/2\pi M_S^2)^{1/2}$. In Ni, ξ is of the order of 60Å. Here A is the exchange stiffness constant. Thus this exchange coupling can drag the surface effect deeper into the interior of the material than the effective anisotropy itself. If the surface anisotropy is strong enough, a surface layer may exist that is unresponsive to a weak bending strain. Consequently, we may express Eq.(4.3.1) as:

$$B^{eff}(t) = B^{bulk} + B^{surface}/(t - t_O) \qquad (5.3)$$

where t_O is associate with the magnetoelastically dead layer possibly caused by strong surface anisotropy and exchange coupling. Thus, exchange coupling between surface and bulk magnetization may drag the surface anisotropy into the interior of the film and may be responsible for the magnetically different layer which we observe.

The other possible origin of the magnetically different layer of thickness t_O is the formation of a solid solution or silicide between the film and the substrate as we have shown in section 4.5. The SADP's and Auger depth profiling of the magnetic films indicate the existence of a magnetically different layer. This is a likely explanation for the t_O offset in the inverse thickness. However, neither the exchange nor the chemical explanation can determine the precise thickness of the magnetically different layer at present.

We now compare the relative significance of interfacial intermixing and exchange coupling to surface anisotropy. Since B^s is positive in the NiFe/Ag and the NiFe/Cu data, the surface magnetoelastic anisotropy can be expected to be perpendicular to the film. However, the B^s values in NiFe are smaller by two orders of magnitude than those of Ni films. Therefore the surface anisotropy is so weak that it only overcomes the magnetoelastic energy in the first monolayer beyond t_o as shown in the last column of Table 5.1. Thus the origin of the magnetically different layer in NiFe films is most likely due to the formation of the solid solution with Ag and Cu substrates as observed in Auger depth profiling.

In Ni/SiO_2 films, the large positive B^s observed implies a strong surface magnetoelastic anisotropy, $B^s \cdot e/t$, with a critical thickness t_c, of order 100Å as shown in Table 5.1. Within this surface layer the spins would be strongly pinned by the surface magnetoelastic energy if a 1.5% strain were present. Pinned surface spins can exchange couple to the in-plane interior spins with 40 to 60 Å of characteristic length. Separately, the formation of the Ni silicide (Ni_3Si), as shown in our TEM work (see section 4.5), can also cause the magnetically different layer. Thus, the 55 Å thick magnetically different layer in Ni films may be due to the combined effects of the exchange coupling and the the chemical compound formation at the interface.

In MBE grown, epitaxial Cu/Ni/Cu films, the magnetically different layers apparently do not exist because the B^s values are determined indirectly by fitting Jungblut's data with an assumed form of $B^{eff} = B^b + B^s/t$. Jungblut's effective anisotropy data include the effects of the exchange coupling between in-plane pinned suface spins and flexible interior spins and formation of the metastable solid solution beween Ni and Cu. Therefore, we should consider the magnetically different layer to interpret the B^s values from the curve fittings and those from the Néel model calculation. Although the Néel model can explain the sign of B^{eff} near the surface, the data show that there are significant differences between the Néel model expectation and the results from the effective anisotropy energy fitting method shown in section 4.4. Incorporating the magnetically different layers with thickness t_o to the Néel model changes Eq.(2.5.9) to $B^{eff} = B^b + B^s/(t-t_o)$. This change effectively shifts the curves in Fig.(2.5.3) (a) and (b) by 30 and 10 Å, respectively, in the positive direction. Then the values in Eq.(2.5.9) become comparable to those in Table 4.4.1.

The Néel model allows us to predict that the effective B is a sum of the bulk B value and the surface B which is inversely proportional to the thickness. Moreover, it predicts

the sign and magnitude of bulk B and surface B values in a single crystal. Our results above support this hypothesis. To improve the accuracy of the prediction, we should relax some assumptions to incorporate the effects of the exchange coupling between surface and interior, the chemical interactions at the interface and the surface relaxation.

Even though the origin of our surface anomaly in B^{eff} remains somewhat clouded, it is clear that our measurements have important technical implications. Since the B^s can be the dominant B in very thin films, the ME anisotropy in thin films should be different from that in bulk-like thick films. Accounting for such differences should lead to improvements in design and manufacture of magnetic devices such as magnetostrictive transducers and MR reading heads. One example for the application of these results may be the magnetic recording head material. So far, people have used binary and ternary alloys base on NiFe to make inductive magnetic read and write heads. These heads require large magnetization and low magnetostriction. Large saturation magnetization enhances the recording signal and low magnetostriction reduces stress induced anisotropy and noise. Typically, Fe and Co are used for the large saturation magnetization (M_S), and Ni is added for low magnetostriction requirements. Fig.(5.1).(a) is a ternary alloy phase diagram of Fe-Co-Ni. The solid curves in Fig.(5.1).(a) indicate the compositions with zero magnetostriction. In some supplementary experiments, we studied ternary alloys with Fe/Co ratio fixed at 1 for various Ni percentages of 65, 70, 75 and 80 %. These compositions are expressed as a solid line in Fig (5.1).(a). Films were grown by S.W. Sun at Boston University using dc-sputtering. The thickness of films was 400Å. Magnetostriction coefficients were measured *ex-situ* by MOKE and the 4-point bending system described earlier. Fig.(5.1).(b) and (c) plot, respectively, the saturation magnetization (M_S) vs. (100-Ni) % and the magnetostriction coefficient (λ) of the films vs. (100-Ni) %. The zero magnetostriction coefficient requirement fixes % of (100-Ni) at 27% with, in turn, limits the M_S to 800 G.

For the very thin films, we can express the magnetostriction coefficient as:

$$\lambda^{eff} = \lambda^b + \lambda^s/t \qquad (5.4)$$

Therefore, if λ^b is positive for a given ternary bulk alloy, then an appropriate thickness (t) which yields $\lambda^{eff} = 0$ can be found provided $\lambda^s < 0$ (ie, $B^s > 0$, as we observed). This result is significant because we can now set the saturation magnetization at any desired level. Then we can compensate the thickness which will make the λ^{eff} equal to zero. In

Second, it would be of interest to study the temperature dependence of the surface and bulk ME coupling coefficients in a cubic system. The theory of magnetic anisotropy shows that anisotropy and ME coupling coefficients should vary with temperature as $m^{l(l+1)/2}$ where m is the reduced magnetization and defined as $m(T) = M_S(T)/M_S(0)$. l is a spherical harmonic index.(l = 4 for cubic, l = 2 for uniaxial). Thus the bulk ME coefficients for a thin film of a cubic material such as Ni should vary sharply with temperature, going as m^{10} while the surface ME coefficient would be of uniaxial symmetry and would decrease with increasing temperature as m^3 (Callen, 1968). This sharp difference in temperature dependence could be resolved if measurements are taken over a modest temperature range.

Third, it is important to determine the effects of the chemical nature of the interface on B^{eff}. A systematic study of buffer or capping layers such as Si, Cu, Ag, SiO_2 etc. will be required to know the effects of these species on B^{eff}. Such studies would serve to clarify the role of surface bonding and alloying in surface anomalies. They would also be of great technical importance by guiding the selection of capping and layering materials in magnetic thin film devices.

In conclusion, we have discovered that magnetoelastic coupling coefficients (or magnetostriction coefficients) of polycrystalline and single crystalline nickel and polycrystalline permalloy ($Ni_{79}Fe_{21}$) thin films can take on anomalously large values in films of thickness less than 40 to 100 Å. The behavior of these coefficients as a function of thickness in films resembles the behavior that is observed for the surface magnetic anisotropy. The behavior is consistent with the Néel model, that is, $B^{eff} = B^{bulk} + B^{surface}/t$. Microstructure induced surface roughness may contribute weakly to this 1/t dependence. Further, we find our data to be shifted on a thickness scale by an amount t_o : $B^{eff} = B^{bulk} + B^{surface}/(t - t_o)$. The origin of this shift appears to be interfacial alloying, and, in Ni films, surface pinning and exchange between the surface and interior of the films. Our new results on NiFe/Ag/Si , NiFe/Cu/Si and Ni/SiO_2/Si have very important implications for thin film devices. These observations suggest that the surface conditions of thin film magnetic devices are of great importance in controlling anisotropy.

effect, we can move into the region with (100-Ni) % greater than 27% in Fig(5.2)(b) and (c). (eg.curve A to B).

To confirm the apparent change in magnetoelastic coupling coefficients in thin films, the following experiments had been suggested but could not be performed because of practical problems. First, we could use different probing depth equipment. If we use blue lasers instead of red lasers, then we can have different magnetic property information because of different skin depth. As skin depth (δ) is propotional to $(\omega)^{-1/2}$, where ω is the frequency of the probe source, we could measure B(t) by using the different wavelengths of the probe source. However it is difficult to change the optical source every time. Furthermore, the square root dependence on wave length (λ) makes it difficult to control probing depth because of the unavailability of lasers of sufficiently different wave lengths.

A second experiment was suggested, in which one could grow films to the maximum thickness to be examined. The magnetic thickness of the films is expected to decrease as annealing time elapses due to interdiffusion. Such an experiment may replicate our data for the magnetic properties of films with different thicknesses. However, controlling the active film thickness by annealing is not trivial because uneven diffusion through grain boundaries might result in irregular interfaces. Further, surface oxidization may also degrade the quality of the magnetic films.

Third, it would be possible to sputter etch the films *in-situ* as in Auger depth profiling. However sputtering may degrade the surface quality because of the sputter induced mixing and it is difficult to control the depth of the film due to lack of the precise knowledge of the sputtering rate.

To extend the present work, the following suggestions are appropriate.

First, our results on polycrystalline NiFe film should be extended to single crystal NiFe films in order to extract two or more ME coupling coefficients. We found difficulty in detecting the magnetoelastic change in the M-H loop for epitaxial Ni/Cu(100) because of the small strain we could apply: $B_1 \cdot e << K_1$. Higher strain could be applied if the films were deposited on a different substrate. Also the method of analysis developed with Bochi (1994) has proven suitable for analysis of such cases. BCC Fe will be of interest because of its two cubic ME coefficients have opposite sign and the Néel model predicts a change in sign for B_1^{eff} as film becomes thinner.

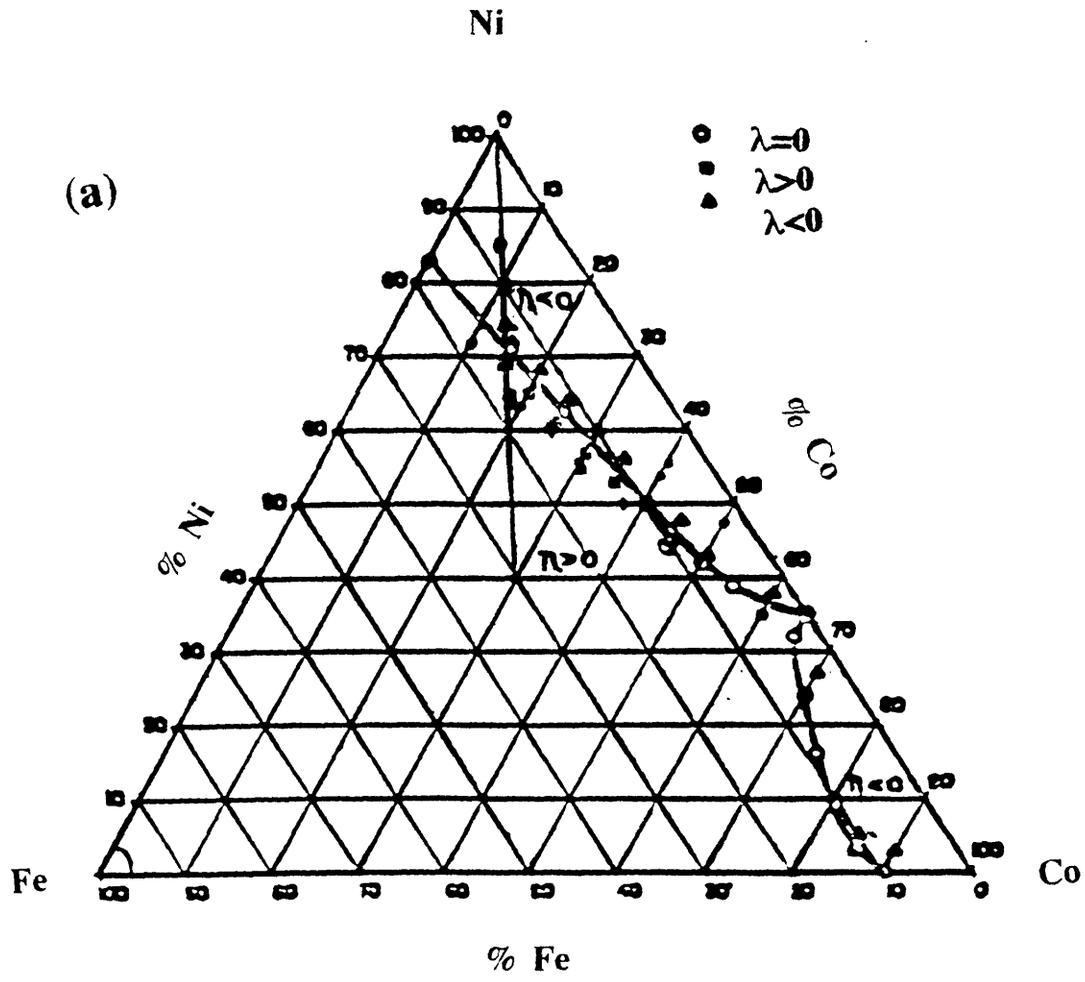

Fig.5.1. (a) Ternary alloy phase diagram of Fe-Co-Ni (after Lampert)
(b) Saturation magnetization with respect to content in $Ni_x(Fe_{0.5}Co_{0.5})_{1-x}$.
(c) Magnetostriction coefficients with respect to content in $Ni_x(Fe_{0.5}Co_{0.5})_{1-x}$.

(b)

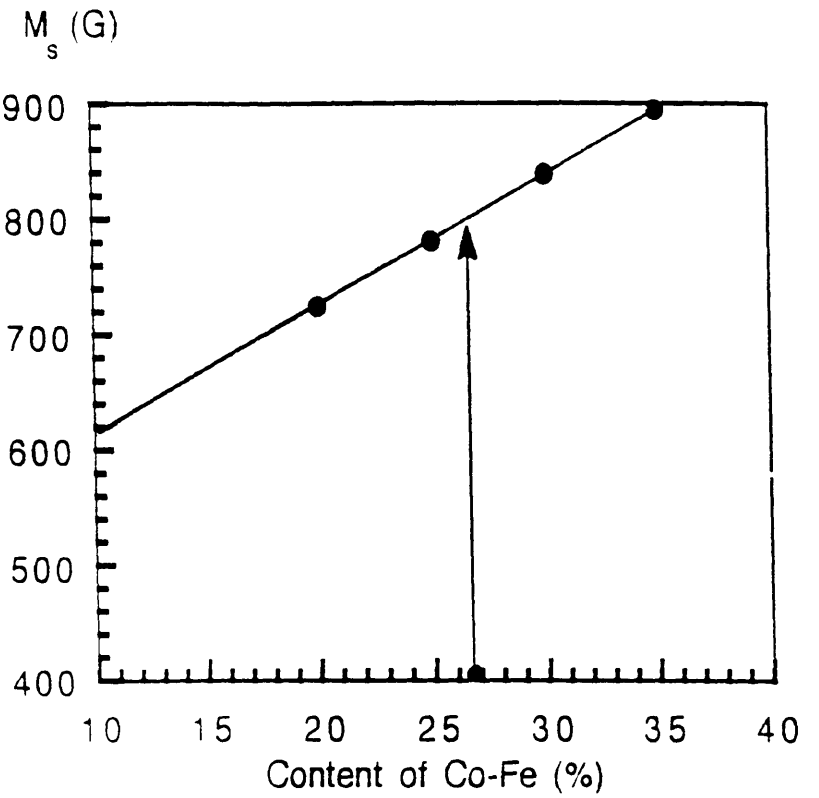
M s (G)
900
800
700
600
500
400
10
15
20
25
30
35
40
Content of Co-Fe (%)

(c)

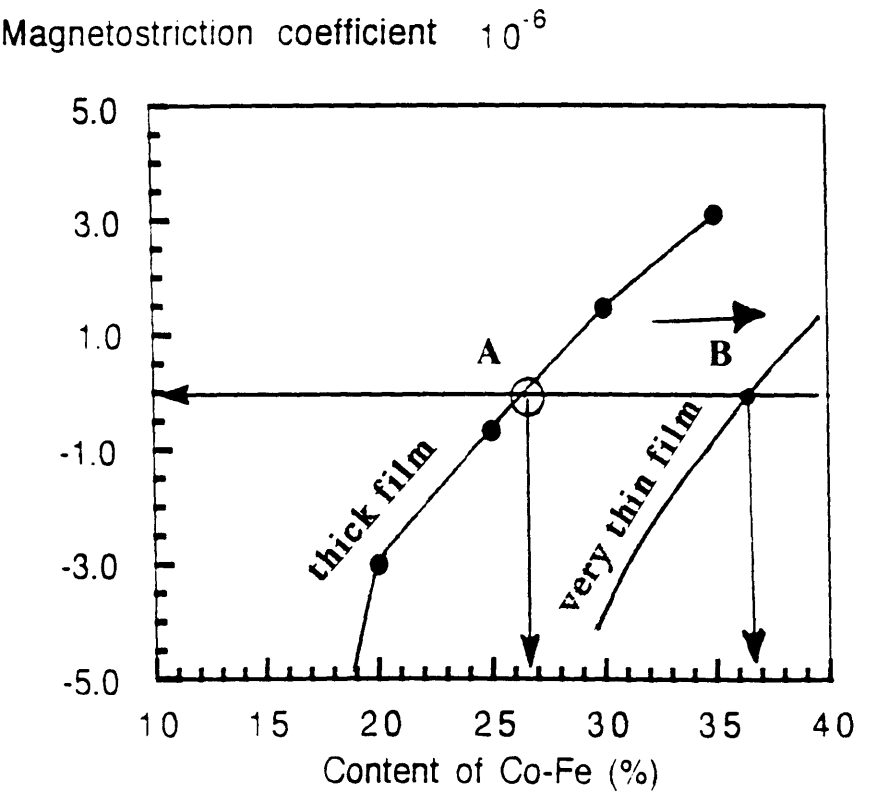
Magnetostriction coefficient 10-6
5.0
3.0
1.0
-1.0
-3.0
-5.0
A
B
thick film
very thin film
10
15
20
25
30
35
40
Content of Co-Fe (%)

References

S. D. Bader, E.R.Moog, J. Appl. Phys., 61, 3729-3733 (1987).

S. D. Bader, J. Mag. Mag. Mater. , 440-454 (1991).

C. A. Ballentine, Ph.D.thesis, The Univ. of Texas at Austin (1989).

M. G. Barthes, A. Rolland, Thin Solid Films 76, 45-52 (1981).

M.I. Batova, I.V. Meshchaninov, S.G. Khayutin, and S.L. Shapiro, Fiz. Met. Met.42, 1324 (1976).

E. G. Bauer, et al., J. Material Research Society, 5, 852 (1990).

A.Berger, U. Lauks, R.L. Stamps, B. Hillerands, G. Guntherodt and H.P. Open, Jounal of Magnetism and Magnetic Materials , 121,483 (1993)

G. H. Bellesis, I. P. S. Harllee, I. A. Renema, D. N. Lambeth, IEEE Trans. Mag., 29, (1993).

G. N. Benninger, A.S.Pavlovic, J. Appl. Phys., 38, 1325 (1967).

G. Bochi, C.A. Ballentine, H.E. Inglefield, S.S. Bogomolov, C.V.Thompson and R.C. O'Handley, Mat. Res.Soc. Symo. Proc. 313,309 (1993).

G. Bochi, O.Song, and R.C. O'Handley, Physical Review B, to be published (1994).

R. M. Bozorth, R. W. Hamming, Physical Review 89, 865 (1953).

R. M. Bozorth,, Physical Review 96, 311-316 (1954).

F. J. A. den Broeder, W. Hoving, and P.J.H. Bleomen, J. Mag. Mat., 93-562 (1991).

W. F. Brown.Jr, J. Appl. Phys., 36, 994 (1965).

L.A. Bruce, H.Jaeger, Philosopical Magazine 36, 6,1331-1354 (1977)

E. R. Callen, Physical Review ,129, 578 (1963).

E. Callen, J. Appl. Phys., 39, 519 (1968).

R. C. Cammarata, K. Sieradzki, Physical Review Letters, 62,17, 2005-8 (1989).

S. A. Chambers, T. R. Greenlee, C. P. Smith, J. H. Weaver, Physical Review B, 32, 4245 (1985).

S. A. Chambers, F. Xu, H. W. Chen, I. M. V. B. Anderson, J. H. Weaver, Physical Review B, 34, 6605-6611 (1986).

C. Chang, Applied Physics Lett. 55, 2754-2755 (1989).

C. Chang, J. Appl. Phys., 71, 825-828 (1992).

C. Charppert and P. Bruno, J. Appl. Phys., 64, 5736 (1988).

S. Chikazumi, *Physics of Magnetism* ,Wiley, (1964).

D. S. Chuang, R,C, O'Handley, Physical Review B, in press (1994).

A. E. Clark, M. Wun-Fogel, IEEE Trans. Mag., 25, 3611-3613 (1989).

T. M. Coughlin, J.H. Jidy. E.R. Wuri, IEEE Trans. Mag., 17, 6, 3169 (1981).

B. D. Cullity, *Introduction to Magnetic Materials* (1972).

H.L.Davis, J.B.Hannon, K.B. Ray, E.W. Plummer, Physical Review Lett. 68, 17,2632-2635 (1992).

L. E. Davis, N. C. MacDonald, P. W. Palmberg, G. E. Riach, and R.E. Weber. *Hand book of Auger electron spectroscopy.*,Physical Electronics Indusries, (1978).

B. N. Engel, C. D. England, R. A. V. Leewen, M. H. Wiedmann, C. M. Falco, Physical Review Letters-in press 67, (1991).

L.C. Fieldman, J.W. Mayer, *Fundamentals of surface andthin film analysis*,257-258,NorthHalland (1986).

J. J. M. Franse, M.STOLP, Physics Letters 32 A, 316 (1970).

H. Fujiwara, T. Tokunaga, H. Tange, M. Goto, Journal of the Physical Society of JAPAN 43, 1554 (1977).

J. E. Goldman, R.Smoluchowski, Physics review 75, 140 (1949).

U. Gonser, M.Ackermann, H.G.Wagner, J. Mag. Mag. Mater., 31-34, 1605-1607 (1983).

U. Gradmann, Applied Physics , 161-178 (1974).

U. Gradmann, J. Mag. Mag. Mater., 173-182 (1977).

U. Gradmann, J. Mag. Mag. Mater.,54-733 (1986).

U. Gradmann, Physics review B 27, 3, 1935 (1983).

U. Gradmann, Bergholtz and Bergter, IEEE Trans. Mag.-MAG.20,1840 (1984)

P. S. Harllee, G. Bellesis, N. Lambeth, 38th annual conference on MMM , (1993).

B. Heinrich, J.F. Cochran, M. Kowalewski, Kirschner, Z. Celinsk, A.S. Arott, K. Mytle, Physical Review B 44, 17, 9348 (1991).

P. Hirsh et al., *Electron Microscope of thin crystals*, Robert E. Krieger Publishing Company,(1977)

H. Hoffman, ang. Phy. 26, 2,(1969).

L. Holland, *Vacuum Deposition of Thin Films*, Wiley, NewYork (1961)

S. Iwasaki, K. Ouchi, IEEE Trans. Mag.,14, 5, 849 (1978)

B. T. Jonker, J. J. Krebs, G. A. Prinz, J. Appl. Phys., 64, 5340-5342 (1988).

R. Jungblut, M.T. Johnson, J. aan de Stegge, A. Reinders and F. J. A. den Broeder, 38th MMM, to be published in J. Appl. Phys. (1994).

T. Katayama, Y. Nishihara, Y. Suzuki, N. Koshizuka, Physical Review Letters 60, 1426-1429 (1988).

E. Klokholm, IEEE Trans. Mag. Mag-12, 819 (1976).

E. Klokholm, S. Krongelb, Proceedings-The electrochemical society 90, 125-136 (1988).

N. C. Koon, B. T. Jonker, F.A. Volkening, J. J. Krebs and G.A. Prinzz, Physical Review Letters 59, 21,2463-66 (1987).

T. Kwaaitaal, B. J. Luymes, W. M. M. M. v. d. Eijnden, J. Mag. Mag.Mater., 26, 187-190 (1982).

H. K. Lachowicz, H. Szymczak,J. Mag. Mag.Mater., 41, 327-334 (1984).

M.G. Lagally, D.E. Savage, MRS Bulletine (1993).

R. E. Lampert, J.M. Gorres and M.H. Hanson, IEEE Trans. Mag. 4, 525 (1968).

E. W. Lee, Reports of Progress in Physics 18, 185 (1955).

E. W. Lee, M. A. ASGAR, Proc.R.Soc.Lond. A, 73 (1971).

K. Mahoney, MIT undergraduate thesis , (1988).

W. P. Mason, IEEE Trans. Mag., 96, 302-310 (1954).

J. W. Matthews and A. E. Blakeslee, J. Cryst. Growth, 12, 126-133 (1975).

D. Mauri, D. Scholl, H. C. Siegmann, E. Kay, J. Appl. Phys., A49, 439-447 (1989).

D. Mauri, V. S. Sperisu, T.Yogi, G.Castillo, D. T. Peterson, IEEE Trans. Mag., 26, 1584-1586 (1990).

R. D. McMichael, MMM93 AR-03 , (1993).

L. Néel, J. de Phys. et Rad. 15, 225 (1954).

S. Nemeth, C. kopasz, J. Mag. Mag. Mater., 112, 139-142 (1992).

R.C. O'Handley, Sol. St. Comm.22,458 (1977).

R. C. O'Handley, Material Science and Engineering , 365-369 (1989).

R. C. O'Handley, O. Song, IUMRS, (1993).

R. C. O'Handley, J. P. Woods, Physical Review B 42, 6568-6573 (1990).

R. C. O'Handley, S.Sun, MRS Anaheim , (1991).

H. Ohmori, K. Katori, M. Hayakawa, IEEE Trans. Mag., 27, 5319-5321 (1991).

D. Pescia, M. Stepanoni, G.L.Bona, A. Vaterlaus, R.F. Williams, F.Meier, Physical Review Lett. 58, 20, 2126 (1987).

Ludwig Reimer, *Transmission electron microscopy*, Springer-Verlag (1984).

G. J. Russell, prog. crystal growth and charact. 5, (1982).

M. J. Sablik, D. C. Jiles, IEEE Trans. Mag., 29, 2113-2123 (1993).

C. M. Scneider, P. Breosler, P. Schster, J. Kirscner, J.J. de Miguel, R. Miranda,S. Ferrer, Vacuum 41, 1-3, 503-505 (1990).

C. Y. Shih, C. L. Bauer, J. Appl. Phys., 64, 5428-5430 (1988).

A. Sloane, *Mechanics of Materials* , Macmillan, New York, (1952).

R. Smouchowski, Physical Review 60, 249 (1941).

O. Song, C. Ballentine, R.C. O'Handley, to be published Applied Physics Lett. (1994).

D. A. Steigerwald, I. Jacob, J. W. F. Egelhoff, Surface Science 202, 472-492 (1988).

M. Sullivan, Rev. Sci. Instrum. 51, 382 (1980).

S. W. Sun, R.C.O'Handley, Physical Review Letters 66, 2798-2801 (1991).

S. Sun, Ph.D.thesis, MIT (1991).

S. W. Sun, R. C. O'Handley, Physical Review Letters 66, 2798 (1991).

J. Tersoff, L. M. falicov, Physical ReviewB 26, 6186-6200 (1982).

E. Tremolet, P. Morin, J. Rouchy, Ann. Phys. 3, 479-501 (1978).

G. Trippel, *Dynamical Magnetostriction Tester* , IBM technical report, (1977).

R. H. Victora, J.M. MacLaren, Physical Review B 47, 11583 (1993).

Robert Walat, MIT BS thesis, (1993).

Akira Yamaguchi, Shinzo Ogu, We-Hyo Soe, and Roichi Yamamoto, Appl. Phys. Lett. 62,1020 (1993).

Xueyuen. Zhu, H. Huang, J. Hermanson, Physical ReviewB 29, 3009-3013 (1984).

R. Zuberek, Thin Solid Films 118, 1-5 (1990).

R. Zuberek, H. Szymczak, R.Kirshnan, M. Tessier, J. de Phys. C8, 49, 1761 (1988).

APPENDIX A: Four-point bending

Fig.(A.1) shows the schematic diagram of the four-point bending mechanism.

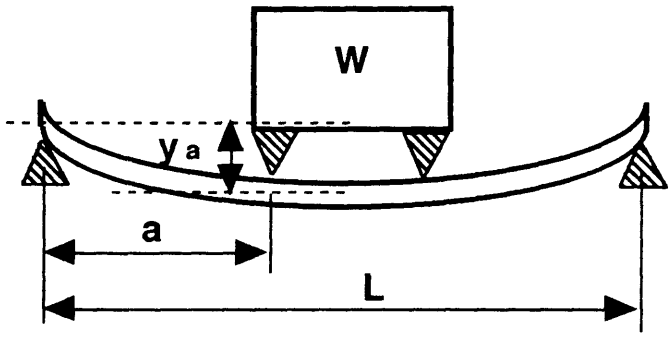

Fig.A.1. Schematic diagram of four-point bending.

In a symmetric four point bending apparatus the bending moment is constant in the central region and is given by

$$M = \frac{W}{2}x - \frac{W}{2}(x - a) = \frac{W}{2}a \qquad \text{(A.1)}$$

where W is the weight on the top ot the sample, x is the distance along the sample, and a is the distance between an outer rod and an inner rod.
the normal bending stress is defined as

$$\sigma = \frac{M}{I}y \qquad \text{(A.2)}$$

where M is the bending moment, y is the distance from the point of interest to the neutral layer, and I is the moment of inertia,which for a rectangular cross section is equal to $bt^3/12$, where b is the width of a sample, and t is the thickness of the wafer.
To determine the stress at the surface of the sample(wafer slice), since the neutral layer is the center of the sample, y should be t/2.

Thus, the bending stress in the top of the surface of the sample is given by

$$\sigma = \frac{3Wa}{bt^2} \qquad \text{(A.3)}$$

The top surface of the wafer will exhibit the same strain as the the magnetic film layer, whose bottom surface shares an interface with the top of the wafer.
The inflation at position 'a' is given by

$$y_a = \frac{Wa^2}{2EI}\left(\frac{4}{3}a - L\right) \qquad \text{(A.4)}$$

where E is Young's modulus of <011> direction on the (100) plane of silicon wafer , 1.68×10^{12} dyn/cm^2.
Then from above two Eqs.(A.3) and (A.4), we get:

$$y_a = \frac{2kae}{t}\left(L - \frac{4}{3}a\right) \qquad \text{(A.5)}$$

where k is a bending shape factor, e is stain at the surface.
We calibrate the strain of the surface of the Si substrate with strain gauge as shown Fig.(A.2) before the bending experiments. We found k=3.65 for 2" wafer with thickness of 10 mil inch and 2.0 for 3" wafer with thickness of 20 mil inch by using strain gauge before the bending experiments. We used BLH SR-4 strain gauges of which resistanc is 350 Ω and G factor=2±2%. Strain gauges are attacehed on the surface of the Si wafer (size: 0.2x1.5") then calibrated with Y_a.
We could get a surface strain (e) through equation given by: (Sullivan, 1980)(Mahoney, 1988)

$$e = 1/G\ (\Delta R/R) = 4/G\ (\Delta V/V) \qquad \text{(A.6)}$$

and we show the calibration result in Fig.A.3.

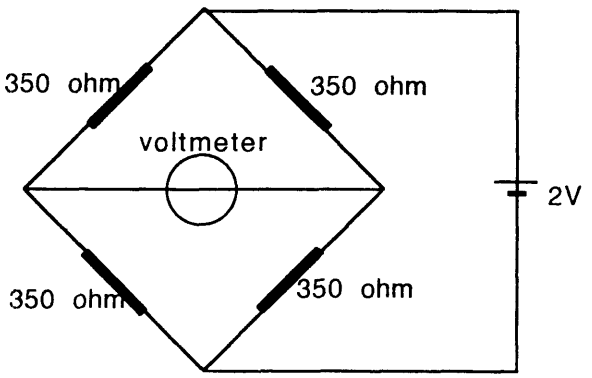

Fig.A.2. Strain gauge setup

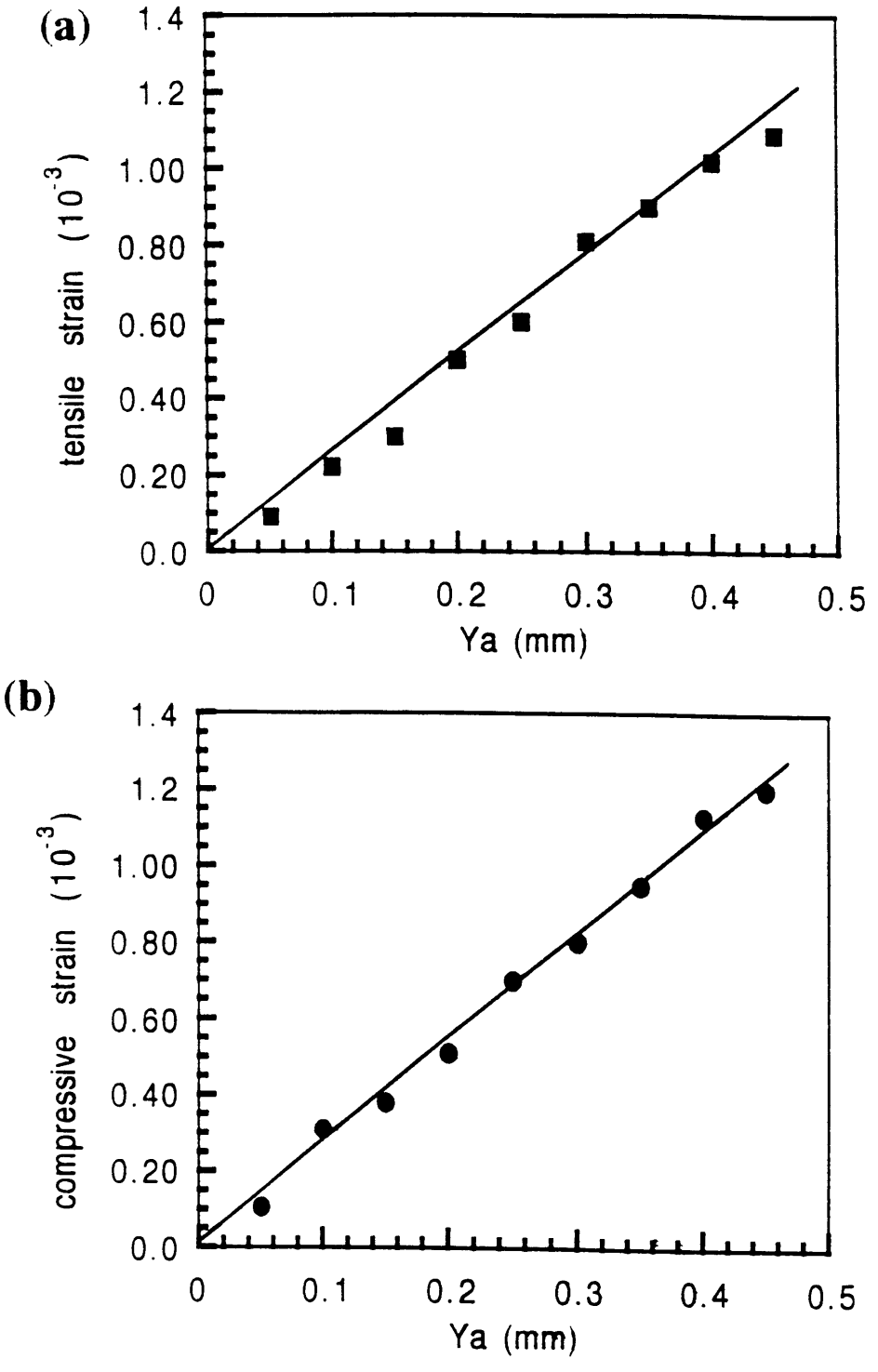

Fig.A.3. Strain according to Y_a in 2" Si wafer.
(a) tensile strain (b) compressive strain

APPENDIX B: Tetragonal symmetry

If the cubic crystalline symmetry becomes tetragonal because of surface relaxation as shown in Fig.(B.1), then we should treat the problem of surface anisotropy in tetragonal symmetry.

Mason (1954) and Callen(1968) give the magnetostriction coefficients but not the form of the energy for tetragonal systems. E. du Tremolet deLacheisserie (1978) lists the tetragonal ME coefficients in their most general form. We list below the anisotropy terms up to order α^6 for the crystal anisotropy energy $f_K{}^i$ and up to order α^2 for f_{ME}. The tetragonal form we chose is more easily related to the familiar cubic forms. The subscripts on the coefficients K_{ij} and B_{ij} are chosen for convenience in relating the tetragonal coefficients to the cubic ones. They are neither tensor nor matrix subscripts.

$$f_K{}^t = K_s\alpha_3{}^2 + K_{11}\alpha_1{}^2\alpha_2{}^2 + K_{12}\alpha_3{}^4 + K_{21}\alpha_1{}^2\alpha_2{}^2\alpha_3{}^2 + K_{22}(\alpha_1{}^4+\alpha_2{}^4)\alpha_3{}^2 + \ldots . \qquad (B.1)$$

$$f_{ME}{}^t = B_{11}(e_{11}\alpha_1{}^2 + e_{22}\alpha_2{}^2) + B_{12}(e_{11}\alpha_2{}^2 + e_{22}\alpha_1{}^2) + B_{13}\, e_{33}\, \alpha_3{}^2 + B_{21}e_{12}\alpha_1\alpha_2 + B_{22}(e_{23}\alpha_2\alpha_3 + e_{13}\alpha_1\alpha_3) + .. \qquad (B.2)$$

Other terms are either absent by symmetry or can be transformed trigonometrically to be of the same form as these (plus constants). Some of the tetragonal terms can be seen to evolve directly from partitioning of the cubic expressions to their tetragonal components (e.g. K_{11} and K_{12} from K_1 or B_{11} and B_{13} from B_1). Others are entirely new (e.g. K_s or B_{12}). The surface anisotropy term, $K_s\alpha_3{}^2$, was first identified by Néel and often is given his name.

From Eqs.(B.1) and (B.2), it is clear that a static strain e_o at a surface could lead to ME anisotropy contributions of the same symmetry as surface anisotropy terms (e.g. a uniaxial strain $e_{33} = e_o$ in $B_{13}e_{33}\alpha_3{}^2$ contributes to the Néel term $K_s\alpha_3{}^2$). Also, a static shear strain could lead to new ME anisotropy terms of symmetry lower than tetragonal (e.g. $e_{ij} = e_{ij}$ in $B_{21}e_{12}\alpha_1\alpha_2$ or $B_{22}(e_{23}\alpha_2\alpha_3+e_{13}\alpha_1\alpha_3)$ produce uniaxial anisotropies 45° off the principal axes).

If we consider thin films as purely tetragonal, and use the direction cosines in the coordinates of Fig.(B.1), we have Eq. (B.3):

$$\begin{aligned} f_{ME} = {} & B_{11}\,(e_{11}\cos^2\phi + e_{22}\sin^2\phi)\sin^2\theta \\ & + B_{12}\,(e_{22}\cos^2\phi + e_{11}\sin^2\phi)\sin^2\theta + B_{13}\,e_{33}\cos^2\theta \\ & + B_{21}\,e_{12}\sin^2\theta\,\sin\phi\cos\phi \\ & + B_{22}\,(e_{23}\sin\phi + e_{13}\cos\phi)\sin\theta\cos\theta \end{aligned} \qquad (B.3)$$

Because we have 5 unknown B's , we need at least 5 equations to find all B's in tetragonal symmetry. It is acceptable to ignore B_{13} and B_{22} in thin films that do not show perpendicular anisotropy ($\theta = 90°$). When $\theta < 90°$ is possible, it may still acceptible to ignore B_{22} because e_{23} and e_{13} should be negligible. It is possible obtain these B's using different combination of applied srain and field as done in cubic symmetry to evaluate B_1 and B_2.

For the case of four-point bending about the y axis that subject the film to tensile strain in the x direction [100] , we have for the strain between the middle two bending points and the coordinate system as shown in Fig. 2.4.1.

$$e = e_0 \begin{vmatrix} 1 & 0 & 0 \\ 0 & -\nu & 0 \\ 0 & 0 & -\nu \end{vmatrix} \approx e_0 \begin{vmatrix} 1 & 0 & 0 \\ 0 & -1/3 & 0 \\ 0 & 0 & -1/3 \end{vmatrix} \qquad (B.4)$$

We then have from Eq.(B.3)

$$\begin{aligned} f_{ME} = {} & \{B_{11}(4\cos^2\phi - 1) + B_{12}(4\sin^2\phi - 1)\}(e_O/3)\sin^2\theta \\ & - B_{13}\,(e_O/3)\cos^2\theta \end{aligned} \qquad (B.5)$$

If the tetragonal ME anisotropy is small then one will observe $B_{12} \approx 0$ and $B_{11} \approx B_{13}$ for the film and B_{11} is about equal to B_1 for the cubic material.

In general the total free energy of the tetragonal surface subject to four-point bending strain is given by the Zeeman energy, magnetostatic energy, low-order crystalline anisotropy terms (Eq.(B.1)) and ME energy (Eq. (B.5)) in cgs units:

$$\begin{aligned} f = {} & -\mathbf{M_s}\cdot\mathbf{H} + 2\pi M_s^2\cos^2\theta \\ & + K_s\cos^2\theta + K_{11}\sin^4\theta\,\sin^2\phi\cos^2\phi + K_{12}\cos^4\theta + \ldots \end{aligned}$$

$$+ \{B_{11}(4\cos^2\phi - 1) + B_{12}(4\sin^2\phi - 1)\} (e_O/3) \sin^2\theta - B_{13} (e_O/3)\cos^2\theta \quad (B.6)$$

If the easy in-plane direction is [110], as for thin epitaxial Ni/Cu(001) (Ballentine, 1990) and fcc Co/Cu(001) (Berger et al, 1992), application of an in-plane field along [100] direction is appropriate as shown in Fig. (2.4.3.1). From Eq.(B.6), the free energy is:

$$f = -M_s H\cos\phi + K_{11}\sin^2\phi\cos^2\phi + [B_{11}(4\cos^2\phi - 1) + B_{12}(4\sin^2\phi - 1)] (e_O/3) \sin^2\theta \quad (B.7)$$

For in-plane magnetization ($\theta = 90^o$), the equation of motion, obtained as before, is:

$$m[(1-2m^2)2K_{11} + 8(B_{11} - B_{12}) e_O/3] = HM_s \quad (B.8)$$

Here we defined $m = \cos\phi$.

Similary, by imposing a different sign of strain and different field direction, we may obtain more relationships to find all B's and K's. First, we can apply compressive and tensile strain e_0 along the [100] direction as shown in Fig.(2.4.3.1) in section 2.4.3. Then Eq.(2.4.4.8) gives,

$$e_O(B_{11}-B_{12}) = a\, K_{11}\Delta A \quad (B.9)$$

for compressive strain and,

$$e_O(-B_{11}+B_{12}) = a'\, K_{11}\Delta A \quad (B.10)$$

for tensile strain. Here a and a' are proportional constants.

Secondly, we can give shear strain as shown in Fig.(2.4.3.3) (B_2 measurements in section 2.4.3.). B_{21} is important for bending along [110] direction. Similarly we get,

$$B_{21} = 2\Delta A\mu_O M_s/(1+\nu)e_O \quad (B.11)$$

and for the m-H loop with e = 0, at the saturation magnetic field (H_S), we get:

$$H_S = -2K_{11}/\mu_O M_s \quad (B.12)$$

Thus from a series of m-H loops under different strains and films surfaces, we can get both ME coupling coefficients and crystal anisotropy constants.
Thirdly, we can apply an out-of-plane external magnetic field, then

$$\mu_O M_s^2/2+(B_{11}+B_{12}+B_{13})e_O=\Delta A \qquad (B.13)$$

From the 5 equations, Eqs.(B.9) to (B.13), we can get B_{11},B_{12},B_{13} B_{21}, and K_{11}.

We have considered low surface relaxation induces a transformation of symmetry from cubic to tetragonal symmetry at surfaces in very thin films. In the case of tetragonal symmetry 5 B's are necessry to describe fully the magnetoelastic coupling of the system. In principle, it is possible to obtain these 5 B's using different combinations of applied strain and field. These surface parameters should indicate the extent to which surface ME coefficients can differ from the corresponding bulk, cubic values, and the extent to which surface ME effects play a role in surface anisotropy.

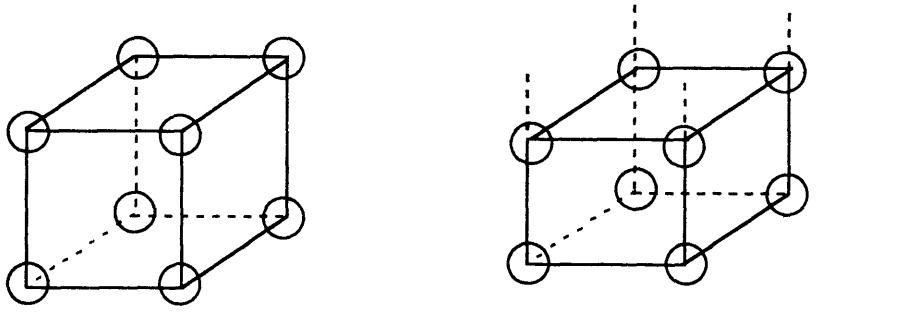

(a) cubic symmetry (b) tetragonal symmetry

Fig.B.1. Illustration of the cubic and tetragonal symmetry. Surface relaxation induce the transformtion of the symmetry from cubic to tetragonal in very thin films.